Studies of Singly and Multiply Charged Secondary Ion Emission And The Effects Of Oxygen On Ionization And Sputter Erosion

by

Richard Carlisle Sobers Jr.

A Dissertation Presented in Partial Fulfillment
of the Requirements for the Degree
Doctor of Philosophy

Approved July 2012 by the
Graduate Supervisory Committee:

Peter Williams, Chair
Mark Hayes
William Petuskey

ARIZONA STATE UNIVERSITY

August 2012

ABSTRACT

Mass spectrometric analysis requires that atoms from the sample be ionized in the gas phase. Secondary ion mass spectrometry achieves this by sputtering samples with an energetic primary ion beam. Several investigations of the sputtering and ionization process have been conducted.

Oxygen is commonly used in secondary ion mass spectrometry (SIMS) to increase ion yields, but also can complicate the interpretation of SIMS analyses. An ^{18}O implant in silicon has been used to quantify the oxygen concentration at the surface of sputtered silicon in order to study the dependence on oxygen of several sputtering and depth profile phenomena.

The ion yield dependence of trace elements in silicon on the surface oxygen concentration is a function of the ionization potential of the element. The ion yield is high and unaffected by oxygen for elements with low ionization potential and ranges over several orders of magnitude for elements with high ionization potential.

Depth resolution in sputter profiles has been shown to be degraded by the presence of oxygen, the mechanism of this effect has been investigated using an ^{18}O implant to quantify oxygen levels and it is shown that the process does not appear to be a consequence of surface oxide formation.

Molecular ions are a source of mass interference in SIMS analysis, and multiply charged atomic ion signals might be interference-free due to the possible instability of multiply-charged molecular ions. Sputtered SiH^{2+}, AlH^{2+}, BeH^{2+}, Mo_2^{2+} and Mg_2^{2+} ions have been observed and appear surprisingly stable. The formation mechanism of some of these species has been explored.

This dissertation is dedicated to wife Dee, my Mom, my Dad, my sister Geri and the rest of my family who supported and believed in me. In memory of my grandparents: Nan, Poppy, Grandma and Grandpa.

ACKNOWLEDGEMENTS

I would like to thank several people who have been of assistance to me while pursuing my PhD. I must first thank my advisor, Peter Williams, for providing me with a great research opportunity and guidance. Pete's perspective on scientific problems has been an education for me. I have also enjoyed working with Pete teaching general chemistry and I have incorporated several of Pete's methods into my own lectures.

I would also like to thank Raul, Gideon, Miranda, Teresa, Adam, Jitao, Jan, Sergei, Klaus and Maitrayee. These past and present members of the Williams group have provided valuable discussion over the years and also many fond memories. The same sentiment applies to my SIMS colleagues Rick Hervig and Linda Williams. I especially want to thank Klaus and Maitrayee. Klaus provided many useful scientific discussions and also trained me to run the Cameca IMS-3f. I have only known Maitrayee a short while but her help during that time has been invaluable. As a recent graduate herself she provided critical perspective and support as I reached the final stages of writing and prepared for my defense.

This PhD took longer than I expected due to unforeseen circumstances. I effectively took an unofficial leave of absence from the program for a period of time. My wife Dee, my advisor Pete, and my committee members Mark Hayes and Bill Petuskey were supportive and I would like to thank them for their patience.

I would also like to thank my good friends Melissa, Josie and Erin. We shared in the experience of graduate school and I am thankful that our friendship continues. I would also like to thank my good friend, Michael Andrews, for helping with some last minute editing.

TABLE OF CONTENTS

Page

LIST OF TABLES ix

LIST OF FIGURES x

CHAPTER

1 INTRODUCTION 1

1.1 Secondary Ion Mass Spectrometry 1

1.2 The Cameca IMS-3f Mass Spectrometer 3

1.3 Acquisition of Mass Spectra 7

1.4 Sputter Depth Profiling 9

1.5 Energy Profiling 11

1.6 References 15

2 INVESTIGATION OF DIATOMIC DICATIONS 17

2.1 Molecular ion interference in Mass Spectrometry 17

2.2 Observations of the SiH^{2+} and AlH^{2+} ions 19

2.3 Mechanism of formation for SiH^{2+} 29

2.4 Other Doubly Charged Diatomic Cations 32

2.5 Mechanism of formation of Mo_2^{2+} 37

2.6 Mechanism of formation of BeH^{2+} 45

2.7 Summary 48

2.8 References 49

3 INTRODUCTION 51

3.1 The Use of Oxygen in SIMS 51

CHAPTER Page

3.2 The ^{18}O Implant in Silicon Method For Measurement of Oxygen Concentration at the Sputtered Silicon Surface..............53

3.3 Characterization of the ^{18}O Implant in Silicon Sample 56

3.4 Measured Surface Oxygen Concentration and Silicon Sputter Yields For Primary Oxygen Ion Beams 61

3.5 The Energy Dependence of the Sputter Yield...................71

3.6 The Angular Dependence of the Sputter Yield..................75

3.7 Normalization of Silicon Sputter Yields 77

3.8 Theoretically Oxygen Free or Clean Silicon Sputter Yields 83

3.9 Clean Sputter Yields Applied to a Similar Study 89

3.10 Normalized Silicon Sputter Yields and the Silicon Atom Fraction 92

3.11 Normalized and Clean Silicon Sputter Yields for Argon Sputtered Silicon with Oxygen Flood Gas 96

3.12 Useful Ion Yields 102

3.13 Summary...118

3.14 References..120

4 ELONGATION OF ION BEAM MIXING TAILS BY STEEP OXYGEN GRADIENT 123

4.1 Ion Beam Mixing and Elongation of Mixing Tails 123

CHAPTER Page

4.2 Measurement of Decay Lengths of Gold, Silver and Copper in Silicon 125

4.3 Measurement of Decay Lengths of Calcium and Magnesium in Silicon 140

4.4 Summary 147

4.5 References 149

5 COMPREHENSIVE REFERENCE LIST 151

LIST OF TABLES

Table Page

2.1 Theoretical and observed abundances of Mo_2^{2+} isotopomers 36

3.1 Peak depth and atom density of implanted elements in silicon sample 60

3.2 Average silicon sputter yields and O/Si ratios of silicon sputtered with oxygen ion beams 62

3.3 Slopes of semi-log plots of useful ion yields vs. ionization potential for several oxygen and argon ion beams 117

LIST OF FIGURES

Figure Page

1.1 Propagation of ions in the Cameca IMS-3f 4

1.2 Extraction field and the field aperture 10

1.3 Two energy profiles 14

2.1 Depth Profile of phosphorous in silicon 20

2.2 Depth Profile of phosphorous in silicon with water vapor flood 22

2.3 Mass spectrum of amorphous silicon hydride on aluminum 23

2.4 High-resolution mass spectrum of amorphous silicon hydride on aluminum at m/z = 15 25

2.5 High-resolution mass spectrum of amorphous silicon hydride on aluminum at m/z = 14.5 26

2.6 High-resolution mass spectrum of amorphous silicon hydride on aluminum at m/z = 14 28

2.7 Energy profiles of Si^{+}, Si^{2+} and SiH^{2+} sputtered from amorphous silicon hydride on aluminum 31

2.8 Mass spectra of beryllium metal showing the BeH^{2+} ion 33

2.9 Mass spectrum of molybdenum metal showing Mo_2^{2+} ions 35

2.10 Mass spectrum of magnesium metal showing Mg_2^{2+} ions 38

2.11 Mass spectra of molybdenum metal at different sample potentials 40

2.12 Pseudo energy profiles of Mo_2^{2+} ions 41

2.13 Mass spectra of molybdenum using two different ion beams 44

Figure Page

2.14 Energy profiles of Be^{2+}, BiH^{2+} and Ar_2^+ and sputtered from beryllium metal 46

3.1 Sputter depth profile of ^{18}O in silicon implant....................54

3.2 Sputter depth profile of silicon containing multiple implants 57

3.3 Sputter depth profiles of ^{18}O in silicon implant with two different oxygen ion beams 65

3.4 Measured silicon sputter yields vs. ion beam impact angle....................69

3.5 Theoretical energy dependence of silicon sputter yields for argon, neon and oxygen ion beams....................74

3.6 Theoretical angular dependence of silicon sputter yields for argon, neon and oxygen ion beams....................76

3.7 Experimental sputter yields normalized to 10keV impact vs. ion beam impact angle 78

3.8 Measured silicon sputter yields vs. ion beam impact energy....................80

3.9 Experimental sputter yields normalized to normal incident impact vs. ion beam impact energy 82

3.10 Theoretical clean silicon sputter yields vs. primary ion beam impact angle for oxygen ion beams....................86

3.11 Theoretical clean silicon sputter yields vs. primary ion beam impact energy for oxygen ion beams 87

3.12 Theoretical clean silicon sputter yields from another study 91

Figure Page

3.13 Silicon sputter yields normalized to normal incidence and 10keV impact energy vs. silicon atom fraction for oxygen ion beams 94

3.14 Silicon sputter yields normalized to normal incidence and 10keV impact energy vs. silicon atom fraction for argon ion beams..................95

3.15 Theoretical clean silicon sputter yields vs. primary ion beam impact angle for argon ion beams 97

3.16 Theoretical clean silicon sputter yields vs. primary ion beam impact energy for argon ion beams..98

3.17 Theoretical clean silicon sputter yields vs. primary ion beam impact angle for oxygen ion beams with oxygen flood......................................99

3.18 Theoretical clean silicon sputter yields vs. primary ion beam impact energy for oxygen ion beams with oxygen flood..................................100

3.19 Useful ion yields of elements sputtered from silicon with oxygen ion beams part 1..105

3.20 Useful ion yields of elements sputtered from silicon with oxygen ion beams part 2..106

3.21 Useful ion yield of silicon sputtered from silicon with oxygen and argon ion beams 107

3.22 Useful ion yield of boron sputtered from silicon with oxygen and argon ion beams 108

3.23 Useful ion yield of aluminum sputtered from silicon with oxygen and argon ion beams 109

Figure Page

3.24 Useful ion yield of oxygen sputtered from silicon with oxygen and argon ion beams 110

3.25 Useful ion yield vs. ionization potential for a 3keV O^+ ion beam ... 114

3.26 Useful ion yield vs. ionization potential for a 14.5keV O^- ion beam 115

3.27 Useful ion yield vs. ionization potential for an 8keV Ar^+ ion beam 116

4.1 Depth profile of a gold surface layer on silicon 127

4.2 Depth profile of a gold surface layer on silicon with oxygen flood . 128

4.3 Gold decay lengths with argon ion beam and oxygen flood 130

4.4 Depth profiles of a silver monolayer in silicon 132

4.5 Depth profiles of a copper monolayer in silicon 133

4.6 Silver decay lengths with argon ion beam and oxygen flood 135

4.7 Copper decay lengths with argon ion beam and oxygen flood 136

4.8 Gold decay lengths with oxygen ion beams 138

4.9 Gold decay lengths with oxygen ion beam and oxygen flood 139

4.10 Depth profiles of a magnesium monolayer in silicon 142

4.11 Depth profiles of a calcium monolayer in silicon 143

4.12 Magnesium decay lengths with argon ion beam and oxygen flood 145

4.13 Calcium decay lengths with argon ion beam and oxygen flood 146

CHAPTER 1

INTRODUCTION

1.1 Secondary Ion Mass Spectrometry

Elemental analysis of a sample by mass spectrometry is achieved by measuring intensities of ions that originated from the sample. Atoms originating from the sample must be ionized and in the gas phase in order to accelerate them through the spectrometer. Mass spectrometry developed from experiments with cathode ray tubes and early experiments investigated the elements and the atomic nature of matter using low-pressure gases. The first observation of isotopes of an element was made in a cathode ray tube experiment when Thomson (1913a, 1913b, Watson 1914) observed the ^{20}Ne and ^{22}Ne isotopes in 1912. These measurements were made using positively charged ions produced between the electrodes by collision with electrons. These canal rays, or kanalstrahlen, were first observed in 1886 (Goldstein 1898) to pass through a hole (canal) in the cathode of a gas discharge tube in a direction of travel counter to the cathode ray. The canal rays were later found to be particles of positive charge (Wien 1898, Ewers 1899).

For samples not already in the gas phase, the sample must be both vaporized and ionized for mass spectrometric analysis. The secondary ion mass spectrometry technique (SIMS) utilizes an ion beam to accomplish both. Secondary ions sputtered from the sample by the primary ion beam are accelerated by the high sample potential into the

mass spectrometer. Sputtering was first observed in the initial studies of gas discharge tubes (Grove 1852, Plücker 1858). To observe ions of alkali metals not easily produced in a cathode ray tube, Gehrcke (1906, 1907a,b,c) placed alkali metal salts mixed with graphite on the anode. These positive anode rays were likely sputtered by electrons and the earliest mass spectrometric measurement of sputtered ions. Early observations of charged particles sputtered by an ion beam are electrons (Austin 1906) and positive ions (Thomson 1910). Both were sputtered from the cathode by canal rays. The first ion source created for the purpose of producing sputtered ions for mass spectrometric measurements was made by Herzog (1949). This ion source produced canal rays that were directed towards a sample. The electric field of the ion source was isolated from that at the sample that accelerated the secondary ions. A decade later, the SIMS technique was being defined and investigated (Honig 1958) for its potential as an analytical tool.

1.2 The Cameca IMS-3f Mass Spectrometer

SIMS experiments discussed here were made on the Cameca IMS-3f mass spectrometer at Arizona State University in the laboratory of Dr. Peter Williams. A general schematic of this instrument is provided in figure 1.1. Primary ion beams produced by the ion source are focused onto the sample surface using ion lenses. The primary ion beam may be operated with a square raster with dimensions up to 500μm. The sample potential is usually operated at ±4.5keV with an optional offset of ±125eV. Different sample potentials are possible using external power supplies. The impact energy of the primary ion beam may range from 3keV up to 22keV and depends on the potential of the primary ion source, V_p, and the potential of sample, V_s. The angle of impact, θ, is also defined by these potentials. The primary ion beam column is at a 30° angle, θ', to the sample surface but the primary ion beam is accelerated by the sample potential.

The impact angle may be calculated from basic electrostatic equations and a general formula has been provided in the literature (Moens 1987):

$$\sin\theta = \frac{\sin\theta'}{\left(1 - V_s / V_p\right)^{1/2}}$$

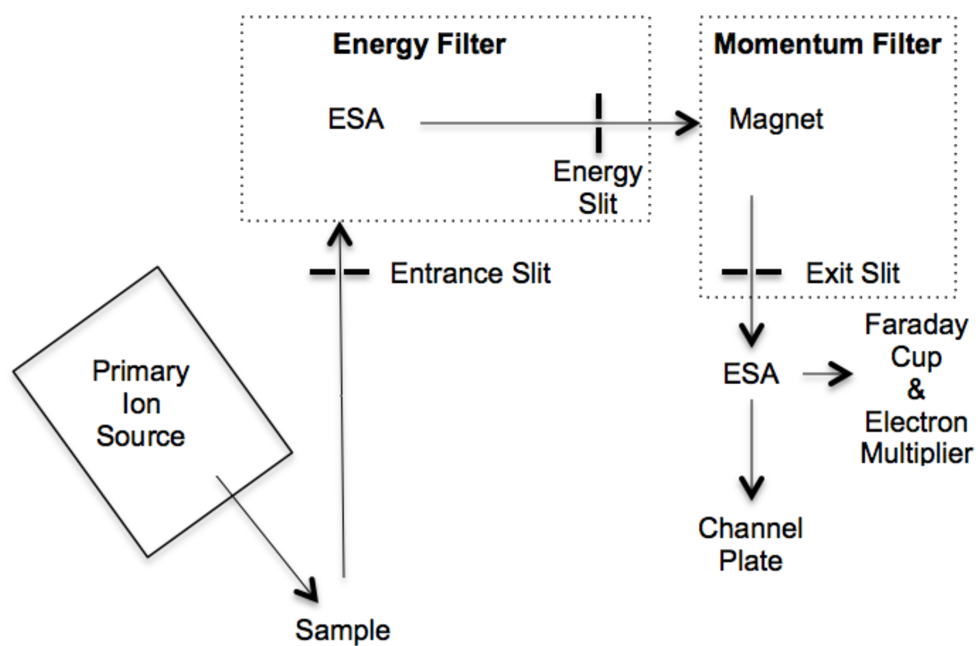

Figure 1.1. Propagation of ions through the Cameca IMS-3f mass spectrometer.

Secondary ions are accelerated through the 1V/μm extraction field towards the ground plate 4.5mm away. The ground plate is also part of an ion optical lens. This lens and any others prior to the entrance slit of the mass spectrometer are used to focus the secondary ions at the point at which they enter the mass spectrometer. The mass spectrometer is a double focusing design of the type first designed by Aston (1919, 1920) that places electric field and magnetic field sectors in series with adjustable slits at the focal points. The energy filter consists of an electrostatic analyzer, ESA, and an adjustable slit. The electrostatic analyzer, ESA, is a curved electric field that bends the ion trajectories and focuses isoenergetic ions into focal points on an arc passing through the energy slit. The energy filter is usually tuned to allow ions with 4.5keV (*z) to pass. The width of the energy slit defines the range of energies with the fully open slit allowing a window of ±60eV (*z). A more selective range is possible by narrowing the slit. The ESA voltage is not changed during an experiment.

After passing through the energy slit, the secondary ions enter the magnetic field. The magnetic field and exit slit together serve as a momentum filter. Isoenegetic ions are focused onto an arc of radius r in order of increasing mass to charge ratio, m/z, after passing through the magnet. The exit slit is located on this arc and ions selected for detection by the magnetic field are focused at the exit slit.

$$\frac{m}{z} = \frac{B^2 r^2}{2V}$$

The increased velocity of a multiply charged ion is matched by the increased charge state and so multiply charged ions are focused on the same arc of radius r.

$$r = \frac{mv}{zB}$$

After leaving the mass spectrometer exit slit, the secondary ions may be detected several ways. The ion trajectories broaden from the focal point at the exit slit and may be imaged at the channel plate. The secondary ions may also be detected using electron multiplier or Faraday cup detectors. An ESA located after the exit slit is activated to bend the trajectories of the ions away from the channel plate and focus them at the location of the electron multiplier detector. A mechanism may be activated to move the Faraday cup detector in front of the electron multiplier to intercept the ions.

1.3 Acquisition of Mass Spectra

A secondary mass spectrum is acquired by changing the strength of the magnetic field to sweep a range of m/z. Secondary ions are selected for detection of a particular mass-to-charge ratio (m/z) in the momentum filter by directing them towards the exit slit with the magnetic field. The selected mass range is sampled by increasing the magnet strength during the experiment. Each data point in a mass spectrum is the time-averaged intensity in counts per second for that particular m/z. A fixed number of points are sampled during a mass spectrum. The range of masses measured simultaneously at a particular magnet setting depends on the width of the exit slit. The mass resolution is defined by the width of a peak, Δm, at a particular mass:

$$R = \frac{\Delta m}{m}$$

Mass resolution is lost due to ions traveling through the spectrometer off of the ion optical axis. Off-axis ions do not pass through the focal points of the spectrometer and may overlap with the focal point of another ion of similar mass at the exit slit. Higher mass resolution is not achieved by simply narrowing the exit slit as off-axis ions of a slightly different mass may still pass through. Narrowing the slit simply allows a smaller range of on-axis ion masses through the exit slit at any particular magnet setting. To achieve higher mass resolution, the entrance slit must be narrowed. Off-axis ions are removed in proportion to the amount of

narrowing of the entrance slit where on-axis ions are focused. Higher resolution is achieved at the expense of decreased intensity. Two peaks resolved by narrowing the entrance slit are still detected simultaneously unless the exit slit is narrowed too.

The energy filter is sometimes narrowed as well to achieve better mass resolution. The magnet is a momentum filter, and with isoenergetic ions, the ions are selected by mass only. Secondary ions are accelerated by a potential, V, in the extraction field to a final velocity. Secondary ions leaving the extraction field may have a distribution of energies due to the initial kinetic energies of the sputtered ions or having been ionized away from the sample surface. At the magnet, higher energy ions are equivalent to having been accelerated by a slightly greater potential, thus reducing the range of velocities by narrowing the energy slit improves the mass resolution.

In practice, the peaks are imaged on the channel plate while narrowing the entrance slit until peaks are resolved. The energy filter is narrowed if necessary to resolve the peaks. The exit slit is then narrowed until the resolved peaks are observed individually. Flat top peaks are observed when the exit slit is wide enough so that when the ions of a particular mass are in the center of the exit slit, all are within it.

1.4 Sputter Depth Profiling

Dynamic SIMS is a SIMS technique with a large enough current density to sputter a significant depth during the experiment. A crater depth of hundreds of nanometers is not uncommon. A sputter depth profile is the secondary ion intensity of an element measured in short time intervals during the entire time the crater is being sputtered. The depth scale is determined by either a measurement of the sputtered crater depth or using previously determined depth markers in the sample such as a monolayer or an implanted isotope. Several isotopes may be measured in the same depth profile by peak switching. The intensity of one secondary ion is measured over a time interval and then the magnet is tuned to the next ion to be measured. Each secondary ion in the duty cycle may be measured at a different sample potential and the same ion may be measured at different sample potentials.

To obtain reliable depth resolution, a field aperture in the mass spectrometer restricts transmission of secondary ions to those originating from the center of the primary ion beam raster. The field aperture diameter is smaller than raster so that secondary ions originating from the sloped crater edges are removed. Figure 1.2 shows a sputtered crater with the sampled area that is defined by a field aperture.

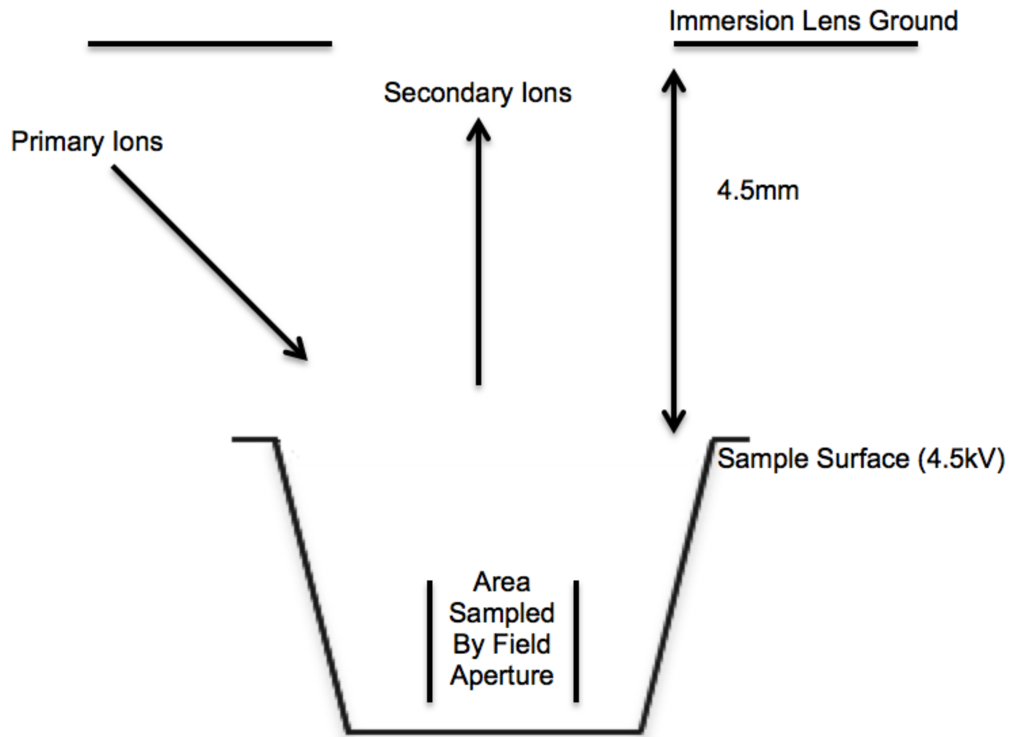

Figure 1.2. The secondary ion extraction field and area sampled by the field aperture. The size of the sputtered crater is greatly exaggerated.

1.5 Energy Profiling

A secondary ion's velocity through the mass spectrometer is due to acceleration in the extraction field. The ion may also possess some initial kinetic energy from the sputtering process prior to electrostatic acceleration. An energy profile measures the initial kinetic energy of secondary ions when formed. The energy filter is set so that secondary ions with energies of 4500eV (*Z) pass through the center of the energy slit. The width of the energy slit is usually open to allow ions with ±60eV energy to pass.

An energy profile measures the changing secondary ion intensity of a particular ion with sample potential. This is done with high "energy resolution" by closing the energy slit to allow transmission of ions within only ±10eV (*z) of 4.5keV(*z). The ESA voltage remains unchanged during SIMS experiments. To observe ions of different energy the sample potential is adjusted.

Ions formed at the sample surface with some additional kinetic energy will have more than 4500eV of energy and do not pass through the energy slit unless the slit width is wide enough. Higher energy secondary ions will pass the energy slit when the sample potential is decreased. The initial kinetic energy of a secondary ion formed at the sample surface is the difference between 4500V and the sample potential, V_s:

$$\text{Initial KE of Ion} = 4500 - V_s$$

This applies to multiply charged cations also as the initial kinetic energy is present prior to acceleration of the newly formed ion in the extraction field.

Some ions are formed away from the sample surface in the extraction field. These are sometimes referred to as sputtered or secondary neutrals to distinguish them from secondary ions that are sputtered in ionic form. Another term commonly used is “gas phase” ions in reference to their ionization away from the sample surface. Gas phase ions are observed in energy profiles with sample potentials greater than 4500V. The initial kinetic energy of these ions would appear to be negative as they are only accelerated over a fraction of the extraction field distance.

The energy profile provides the initial kinetic energy of sputtered ions. For gas phase ions, the energy profile provides a measure of the distance from the sample surface at which the ion was formed. A singly charged cation formed 100μm from the sample surface would only be accelerated over 4400μm of the 1V/μm extraction field. Such an ion would be observed in the energy profile at a sample potential of 4600V and appear to have a 100eV energy deficit. The distance from the surface is not as straightforward for multiply charged ions as these may first be accelerated some distance with a +1 charge prior to losing more electrons.

Energy profiles in this dissertation are presented with a sample potential scale rather than an energy scale. This is not uncommon and is done for several reasons. For gas phase ions, the significance of the

sample offset being a measure of the distance from the sample surface is sometimes lost when plotted against “initial kinetic energy”. A distance scale would be more appropriate for gas phase ions. Also when comparing singly and multiply charged ions formed away from the surface, separate depth scales are required.

An energy scale in an energy profile is also confusing in that the distinction between sputtered ions and gas phase ions is sometimes lost. In the literature and in presentations, the “low-energy” ions of an energy profile may be discussed. Low-energy ions are specifically sputtered ions appearing at 4500V or slightly less in the energy profile, having low initial kinetic energy. In this connotation “ion” or “secondary ion” distinguishes the ion as having not been formed in the gas phase. In other connotations “secondary ion” applies to both. Higher energy ions would be observed at even lower sample potentials. The negative energy of a gas phase ion in an energy profile may be confused as being a low-energy ion.

Two energy profiles are shown for comparison in figure 1.3. The distribution of ion intensity with sample potential of the silicon ion indicates that it is formed at the surface as a sputtered ion. The intensity drops off at 4500V with no gas phase ions formed. The distribution of ion intensity for sample offsets less than 4500V reflects the distribution of initial kinetic energies. The Ar^{2+} ion by comparison is formed as a gas phase ion. The energy distribution of these ions is all above 4500V sample potential. Ions are formed in significant amounts at over 100µm from the sample surface.

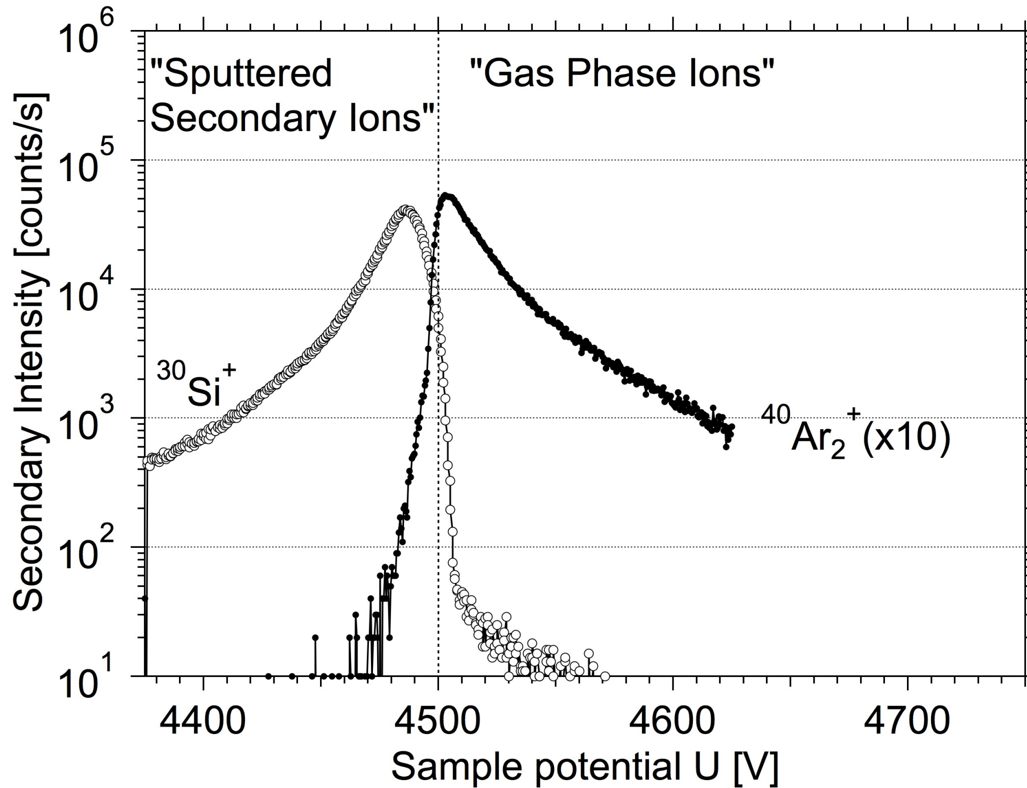

Figure 1.3. Examples of energy profiles of two ions. The $^{30}Si^{+}$ ion was produced by sputtering silicon with an argon ion beam. The energy filter is centered to allow transmission of ions having 4.5keV ±10eV energy. The silicon ions are produced at the sample surface with a distribution of energies and accelerated over the entire distance of the extraction field. Silicon ions having no initial kinetic energy pass through the energy filter when the sample potential is 4500V. Ions with additional kinetic energy are observed with a sample potential less than 4500V. The $^{40}Ar_2^{+}$ ion energy profile was made by sputtering beryllium metal with an argon ion beam. The argon dimer ion is formed in the gas phase away from the sample surface. The argon ions are not accelerated over the entire extraction field and are observed at sample potentials greater than 4500V. The sample potential at which the gas phase ion is observed is a measure of the distance from the sample surface at which it is formed.

1.6 References

Aston, F. W. (1919). A positive ray spectrograph. *Philosophical Magazine, 38*, 707 - 714.

Aston, F. W. (1920). The mass-spectra of chemical elements. *Philosophical Magazine, 39*, 611 - 625.

Austin, L. W. (1906). On an emission of negatively charged particles produced by canal rays. *Physical Review, 21*, 312 - 319.

Ewers, P. (1899). Zur Mechanik der canal- and kathoden-strahlen. *Annalen Der Physik Und Chemie, 69*, 167 – 199.

Gehrcke, E., Reichenheim, O. (1906). Anodenstrahlen. *Berichte der Deutschen Physikalischen Gessellschaft, 8*, 559 - 566.

Gehrcke, E., Reichenheim, O. (1907a). Anodenstrahlen. *Berichte der Deutschen Physikalischen Gessellschaft, 9*, 76 - 83.

Gehrcke, E., Reichenheim, O. (1907b). Anodenstrahlen. *Berichte der Deutschen Physikalischen Gessellschaft, 9*, 374 - 379.

Gehrcke, E., Reichenheim, O. (1907c). Anodenstrahlen. *Berichte der Deutschen Physikalischen Gessellschaft, 9*, 200 - 204.

Goldstein, E. (1898). Ueber eine noch nicht untersuchte strahlungsform an der cathode inducirter entladungen. *Annalen Der Physik Und Chemie, 64*, 38 - 48.

Grove, W. R. (1852). On the electro-chemical polarity of gases. *Philosophical Transactions Of The Royal Society Of London, 142*, 87 - 101.

Herzog, R. F. K., Viehböck, F. P. (1949). Ion source for mass spectrography. *Physical Review, 46*, 855 - 856.

Herzog, R. F. K., Poschenrieder, W. P., Satkiewicz, F. G. (1973). Observations of clusters in a sputtering ion source. *Radiation Effects, 18*, 199 - 205.

Honig, R. E. (1958). Sputtering of Surfaces by Positive Ion Beams of Low Energy. *Journal, 29*, 549 - 555.

Moens, M., Adams, F. C., Simons, D. S. (1987). Dependence of interface widths on ion-bombardment conditions in secondary ion mass-spectrometric analysis of a nickel chromium multilayer structure. *Analytical Chemistry, 59*, 1518 - 1529.

Plücker, J. (1858). Ueber die einwirkung des magneten auf die elektrischen entladungen in verdünnten gasen. *Annalen Der Physik Und Chemie, Vol*, 88 - 106.

Thomson, J. J. (1910). Rays of positive electricity. *Philosophical Magazine, 20*, 752 - 767.

Thomson, J. J. (1913a). On the appearance of helium and neon in vacuum tubes. *Nature, 90*, 645 - 647.

Thomson, J. J. (1913b). On the appearance of helium and neon in vacuum tubes. *Science, 37*, 360 - 364.

Watson, H. E. (1914). Some experiments on the electrical discharge in helium and neon. *Proceedings of the Cambridge philosophical society. Mathematical and physical sciences, 17*, 90 - 107.

Wien, W. (1898). Untersuchungen über die electrische entlandung in verdünnten gasen. *Annalen Der Physik Und Chemie, 65*, 440 - 452.

CHAPTER 2

INVESTIGATION OF DOUBLY CHARGED DIATOMIC CATIONS

2.1 Molecular ion interference in Mass Spectrometry

Molecular ions are a common source of background interference in mass spectrometry. The choice of a proper mass spectrometric technique may be made with knowledge of the molecular ions that are expected from different samples. A small molecular ion observed in SIMS analysis of silicon samples, SiH^+, interferes in measurements of phosphorous in silicon. A method for avoiding this mass interference is extreme energy filtering (Schauer 1990). Another option for avoiding mass interference is to use a higher mass resolution by closing entrance and exit slits on the spectrometer. These methods are not always practical due to decreased secondary ion intensity.

One method that is quite successful at removing cluster ion interference is accelerator mass spectrometry. Negative ions are accelerated towards a positive terminal with millions of volts of potential. At the location of the high-potential terminal is also a charge stripper. A charge stripper removes electrons by collision with a gas or thin foil:

$$AB^{n} + M \rightarrow AB^{n-m} + M + me^{-}$$

The positive ion is further accelerated away from the high positive potential at the terminal. One of the several factors contributing to the reduced molecular interference observed in accelerator mass spectrometry is that positive ions with multiple charges are usually

unstable and fragment in a process described as a Coulomb explosion. Small, multiply charged, molecular ions are especially expected to be unstable due to the high charge density. High-energy mass spectrometers are larger and more expensive due to the high voltage requirement. These tandem accelerators may be part of a secondary ion beam column of a SIMS instrument (accelerator SIMS).

Weathers (1991) noted that while a +2 or +3 charge was generally accepted to be a high enough charge to avoid molecular interference in accelerator mass spectrometry, some small, multiply charged molecules are known to exist and so began a search for them. In the process, the B_2^{3+} ion was observed using accelerator SIMS. The metastable nature of these small, multiply charged ions are indicative of the relative strengths of the covalent bonding and the coulomb repulsion within the molecule. A +3 or +4 charge is usually used in accelerator SIMS measurements now to avoid background from ions of this sort. These small dications are also important to chemical bonding theoreticians. The He_2^{2+} ion was predicted to be stable by Pauling (1933) but not observed until decades later in a charge stripping reaction of He_2^{+} (Guilhaus 1984).

Small dications may be observed and studied in low-energy SIMS experiments. It is a more cost effective method than accelerator mass spectrometry but also provides an alternative formation process for study. In the present study, several diatomic dications have been observed either

for the first time or for the first time created as secondary ions sputtered from a sample.

2.2 Observations of the SiH^{2+} and AlH^{2+} ions

The stability of the SiH^{2+} ion was investigated as the possible background interference at m/z = 15.5 from sputtered silicon. If the dication is unstable then analysis of phosphorous in silicon would be possible by measurement of the P^{2+} ion free of any SiH^{2+} background. A Coulomb explosion of sputtered SiH^{2+} has been noted as a probable source of low energy secondary hydrogen ions sputtered from amorphous silicon hydride using a noble gas primary ion beam (Wittmaack 1979) but SiH^{2+} has not been previously identified in secondary ion mass spectra. Figure 2.1 shows a depth profile of a phosphorous in silicon implant using a 10.5keV Ar^{+} primary ion beam. The peak to background ratio improves from 25 for P^{+} to 170 for P^{2+}. The peak to background ratio is better for the P^{3+} ion but at the expense of decreased peak intensity.

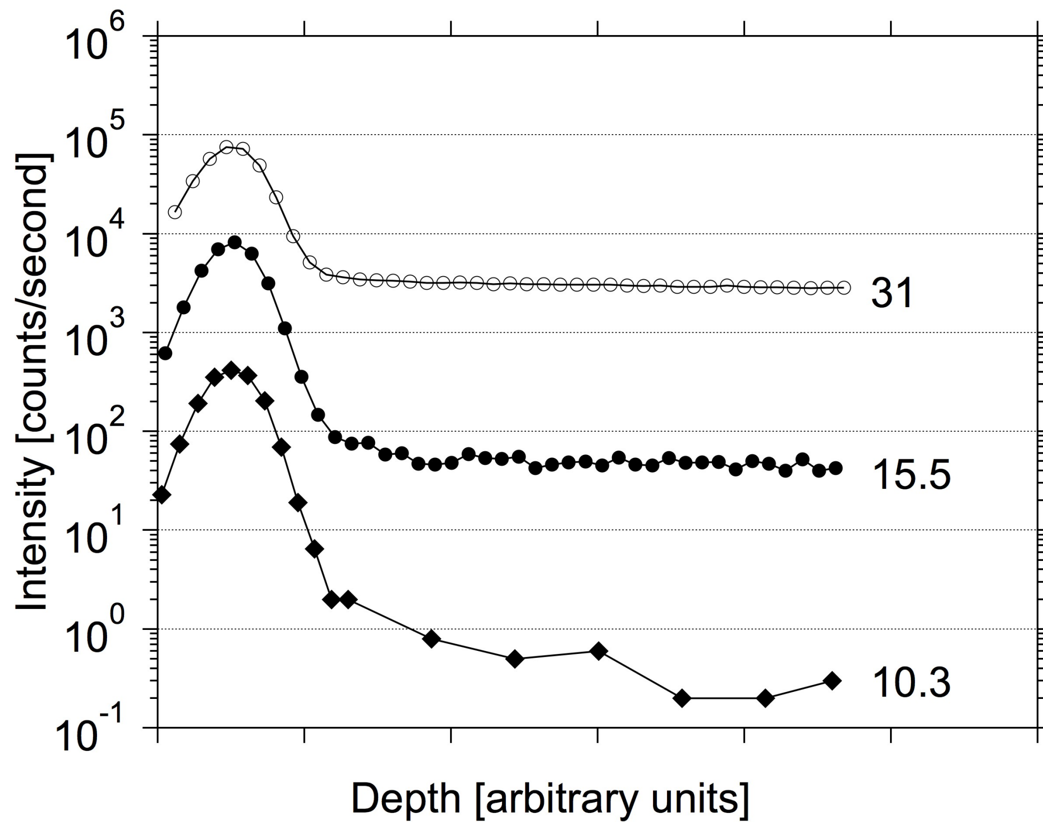

Figure 2.1. A positive secondary ion mass spectrum produced by sputtering ^{31}P implanted silicon with 10.5 keV Ar^{+}. The monitored $^{30}Si^{+}$ ion intensity (not shown) was constant during the course of the depth profile. Each data point is the average counts per second measured over a 2 second count time. Data points for m/z = 10.3 have been binned into average intensity over a 10 second count time at depth beyond the phosphorus implant. The primary ion beam was operated with a current of 810nA and a 250μm square raster. The ^{31}P implant was previously prepared with impact energy of 80 keV and a dose of $1x10^{16}$ atoms/cm^2.

A second depth profile in figure 2.2 was made under the same operating conditions with the addition of water vapor to the sample chamber. The background intensity of the P^+ ion increases when the sample surface is exposed to a source of hydrogen atoms. The background signal at m/z = 31 is due to the $^{30}SiH^+$ ion. Somewhat surprisingly an increased background was also observed at m/z = 15.5 indicating that the SiH^{2+} ion is formed and survives transmission through the spectrometer. The undetectable change in peak to background ratio of P^{3+} indicated that the SiH^{3+} ion does not form or does not have a long enough lifetime to reach the detector.

An amorphous silicon hydride sample served as another means to observe the SiH^{2+} ion without the addition of a flood gas. The $^{30}SiH^{2+}$ is seen at m/z = 15.5 in the mass spectrum of figure 2.3 made by sputtering silicon hydride with an 8keV argon ion beam. The thin silicon hydride layer is on an aluminum substrate. Sputtered Al^{2+} ions at m/z = 13.5 originate from the sample substrate.

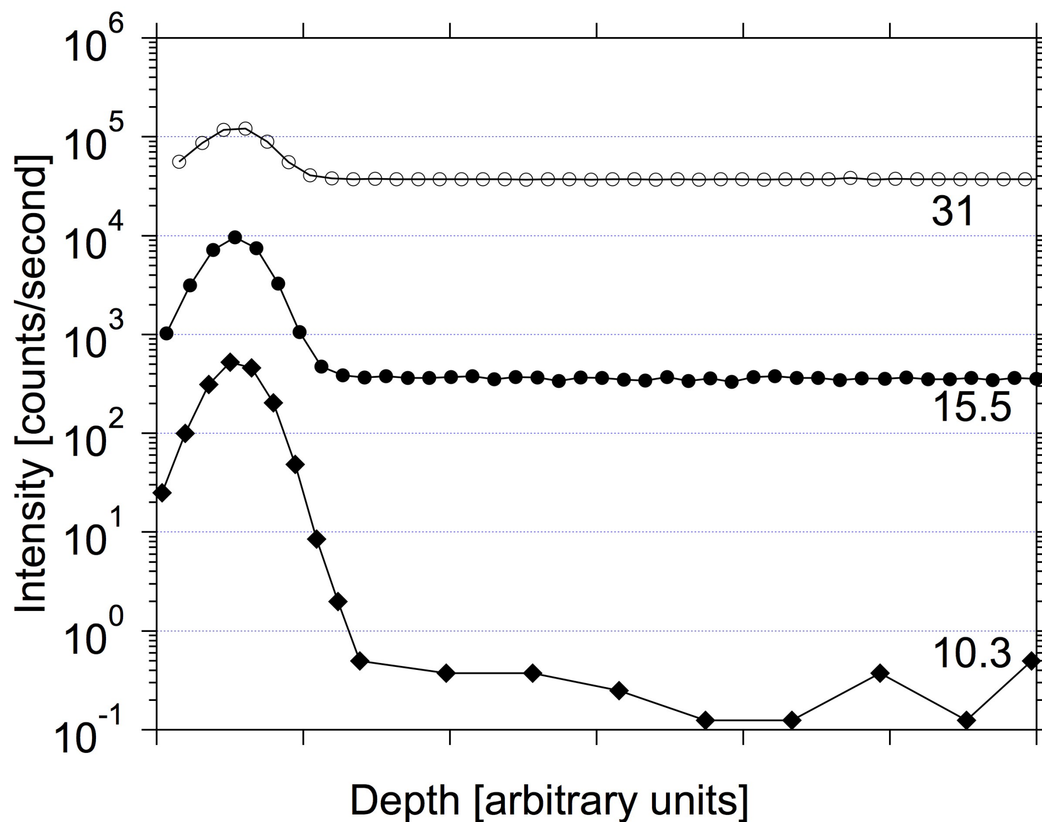

Figure 2.2. A positive secondary ion mass spectrum produced by sputtering ^{31}P implanted silicon with 10.5 keV Ar^+ primary with addition of water vapor to the sample chamber. Measured pressure over the sample was 1.9×10^{-5}torr when water vapor was introduced compared to usual operating pressure of 1×10^{-7} torr with vacuum. The monitored $^{30}Si^+$ ion intensity (not shown) was constant during the course of the depth profile. Each data point is the average counts per second measured over a 2 second count time. Data points for m/z = 10.3 have been binned into average intensity over a 8 second count time at depth beyond the phosphorus implant. The primary ion beam was operated with a current of 870nA and a 250μm square raster. The ^{31}P implant was previously prepared with impact energy of 80 keV and a dose of 1×10^{16} atoms/cm^2.

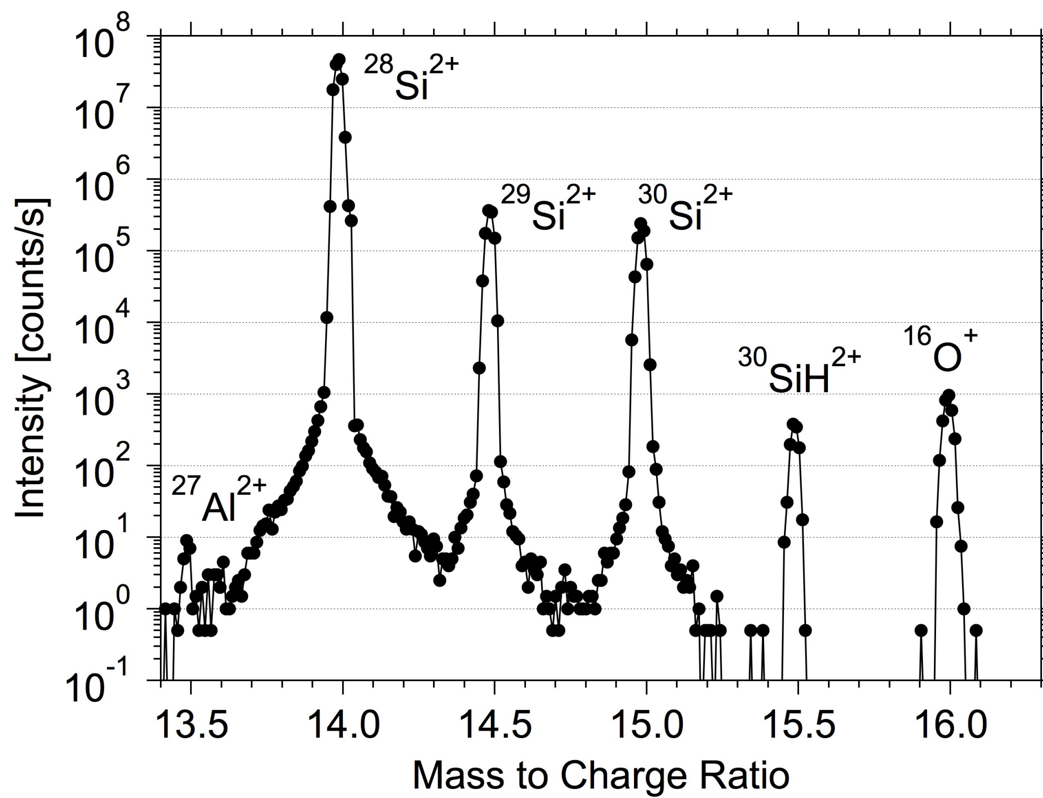

Figure 2.3. Mass spectra of amorphous silicon hydride on an aluminum substrate sputtered with 8keV Ar^{+}. A 1μA primary ion current was used with a 500μm square raster.

High-resolution mass spectra of the silicon hydride sample were acquired to confirm the $^{30}SiH^{2+}$ peak assignment at m/z = 15.5. The $^{28}SiH^{2+}$ and $^{29}SiH^{2+}$ ions are not observed in the low resolution mass spectra of figure 2.3 due to the dominance of the Si^{2+} peaks at those masses. To observe these molecules and better confirm the peak assignment, high-resolution mass spectra ($m/\Delta m = 4000$) of an amorphous silicon hydride sample were acquired. Hydrogen is already part of the sample matrix so no additional flood gas was required. At m/z = 15.5, only one peak was observed in the high-resolution mass spectrum (not shown). The $^{30}Si^{2+}$ and $^{29}SiH^{2+}$ ions are expected to have a mass difference of $5.3x10^{-3}$u. These ion peaks are resolved in the mass spectrum of figure 2.4 with a mass difference of $5.5x10^{-3}$u. Similarly in figure 2.5 a measured mass difference of $4.7x10^{-3}$ u separates the $^{28}SiH^{2+}$ ion peak from the more intense $^{29}Si^{2+}$ near mass 14.5. The expected mass difference is $4.1x10^{-3}$u.

Sputtering near the interface of the silicon hydride and aluminum substrate provided the means of looking for multiply charged aluminum hydride ions. The additional peak near m/z = 14.5 is identified as the $^{27}AlH_2^{2+}$ ion. This ion has a measured mass $9.8x10^{-3}$u greater than $^{29}Si^{2+}$ and the expected mass difference is $1.0x10^{-2}$u. This ion was absent from mass spectra acquired closer to the sample surface away from the interface.

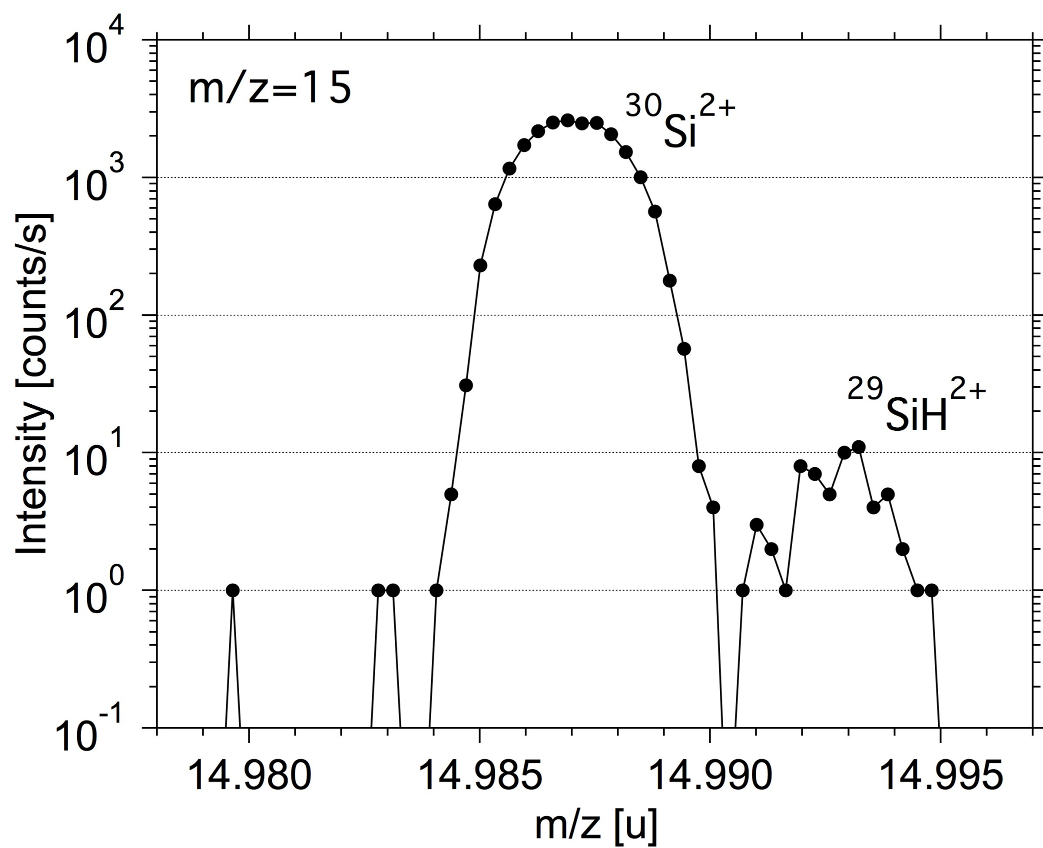

Figure 2.4. High-resolution mass spectrum near m/z = 15.0 of amorphous silicon hydride sputtered with 8 KeV Ar^+ primary ion beam. The primary ion beam had a current of 900nA with no raster of the beam.

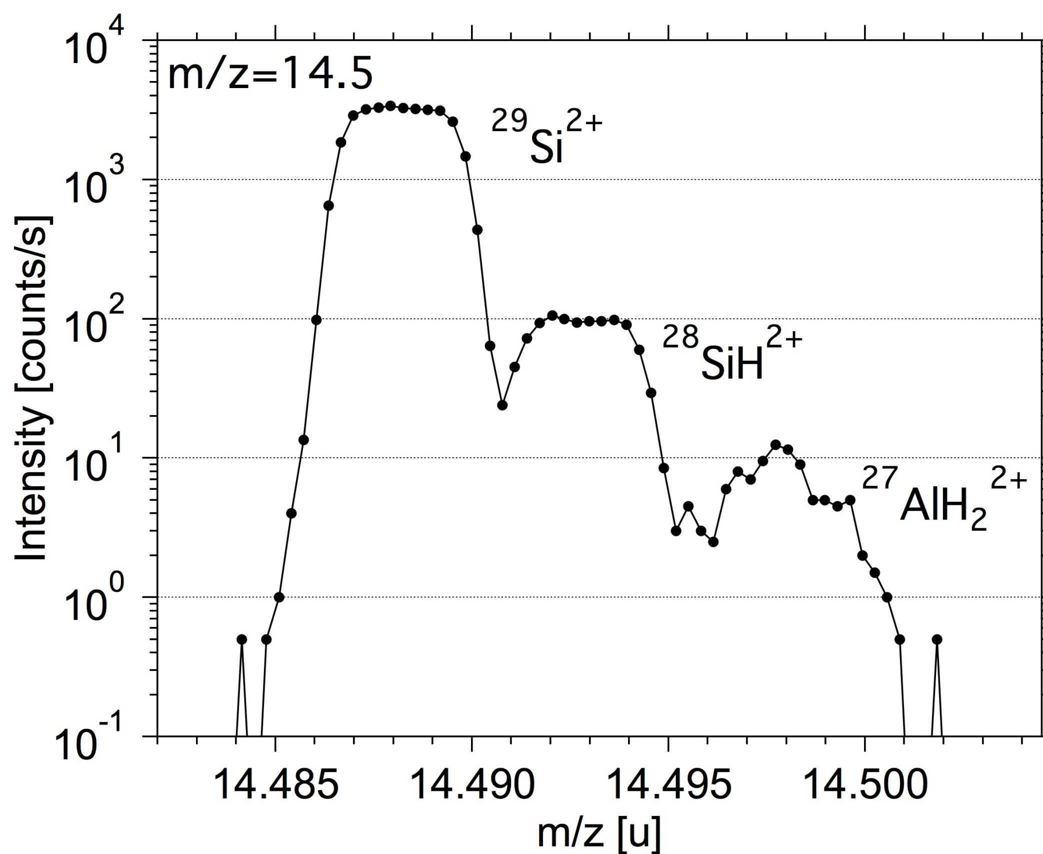

Figure 2.5. High-resolution mass spectrum near m/z = 14.5 of amorphous silicon hydride sputtered with 8 KeV Ar^+ primary ion beam. The primary ion beam had a current of 900nA with no raster of the beam.

An additional high-resolution mass spectrum was acquired near mass 14 to observe the $^{27}AlH^{2+}$ ion that is expected to have a mass $6.2x10^{-3}$u greater than that of $^{28}Si^{2+}$. The two ions are resolved in the mass spectrum in figure 2.6 with a mass difference of $6.6x10^{-3}$u separating the two. The AlH^{2+} ion had predicted to be stable (Gill 1988, Nefedova 1995) but had not been previously observed. The ion may be produced with greater secondary ion intensity by sputtering a copper on aluminum grid (Franzreb 2004b). The peak assignment of AlH^{2+} ion was further confirmed by its mass to charge ratio relative to N^+ and CH_2^+ ion peaks observed near m/z=14 present due to the addition of atmospheric flood gas to the sample chamber.

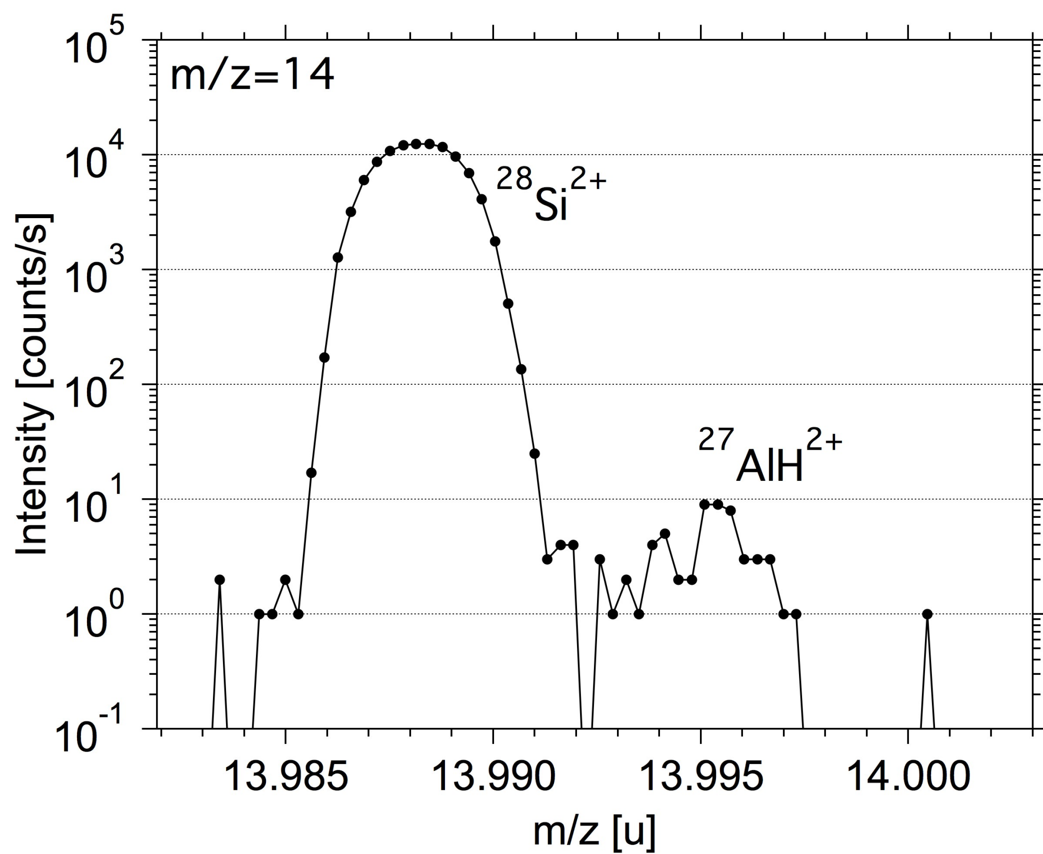

Figure 2.6. High-resolution mass spectrum near m/z = 14.0 of amorphous silicon hydride sputtered with 8 KeV Ar^+ primary ion beam. The primary ion beam had a current of 900nA with no raster of the beam.

2.3 Mechanism of formation for SiH^{2+}

Joyes (1968, 1969) has stated that cations sputtered directly from the surface are neutralized by electron tunneling and that observed secondary ions are actually formed by Auger electron emission. The core hole excited state is created during the collision cascade and has a long enough lifetime for the Auger decay to occur several angstroms from the sample surface.

$$Si^{*} \rightarrow Si^{+} + e^{-}$$

This appears to be the mechanism by which multiply charged secondary silicon ions, Si^{n+}, form.

$$Si^{*,+} \rightarrow Si^{2+} + e^{-}$$

Auger electrons correlated with multiply charged silicon ions sputtered from silicon with a primary ion beam have been observed (Wittmaack 1980) and the energy profile of sputtered Si^{2+} ions has been observed to be similar to that of Si^{+} (Schauer 1992).

Energy profiles of Si^{+}, Si^{2+} and SiH^{2+} sputtered from amorphous silicon hydride are shown in figure 2.6. These energy profiles were made with the energy filter centered to allow transmission of ions having energies of 4500±10eV (*z). No gas phase ions are observed for these three ions at sample potentials greater than 4500V. The few angstrom distance required for a singly charged cation to travel before undergoing Auger electron emission and avoid neutralization from electron tunneling

from the sample surface is too small to be detected in the energy profile. A similar Auger electron emission mechanism is suggested for SiH^{2+} ion:

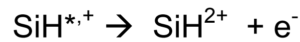

$$SiH^{*,+} \rightarrow SiH^{2+} + e^-$$

Energy is transferred from the primary ion to the sputtered atom during a collision. The initial kinetic energy of the sputtered ion originates from some fraction of the collisional energy. Both low and high-energy collisions may produce low-energy ions observed in the energy profile close to 4500V but high-energy ions require high-energy collisions. As a result, the energy profiles of secondary ions often have a change in slope with a low-energy "peak". This is the case for the energy distributions of both Si^+ and Si^{2+} in figure 2.7. High-energy collisions are more likely to fragment the SiH^{2+} molecular ion and the energy distribution with initial kinetic energy decreases more steeply and lacks the low energy peak.

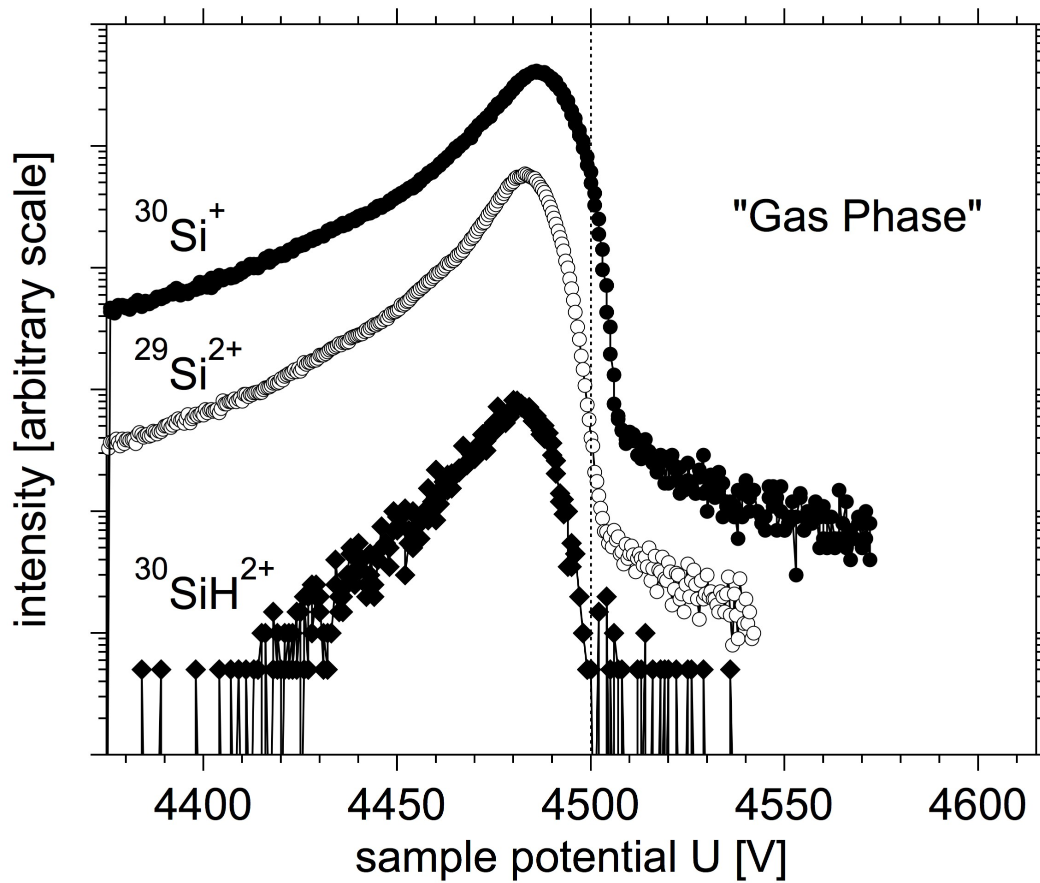

Figure 2.7. The energy profile of $^{30}SiH^{2+}$ (m/z = 15.5), $^{29}Si^{2+}$ (m/z =14.5) and also $^{30}Si^{+}$ (m/z = 30). Each was obtained by sputtering a-SiH on aluminum substrate with a 1 µA of 8 KeV Ar^{+} primary ion beam with a 500µm square raster. The energy filter was centered to allow transmission of ions within a narrow range of energies centered on 4.5keV.

2.4 Other Doubly Charged Diatomic Cations

The observation of stable (or long-lived) SiH^{2+} ions was an indication that these electron-deficient species could survive the intense Coulomb repulsion. SiH^{2+} still has a total of three valence electrons to make a bond and so it was decided to explore the stability of BeH^{2+} that retains only a single valence electron. Quite surprisingly stable (or long-lived) BeH^{2+} was detected.

The BeH^{2+} ion is observed in the mass spectrum of argon sputtered beryllium metal at $m/z = 5$ in figure 2.8 when the toluene vapor is added to the sample chamber. The background increases by an order of magnitude with the addition of the toluene vapor. No BeH^{2+} peak is observed in the mass spectrum made without the addition of the toluene vapor despite the lower background intensity. Further confirmation of the peak assignment was made by similar mass spectra produced with D_2O vapor added to the sample chamber (Franzreb 2005). With addition of deuterium to the sample surface, a BeD^{2+} peak at $m/z = 5.5$ was observed. A D_2H^+ peak observed at $m/z = 5$ also had the correct relative mass difference from BeH^{2+}.

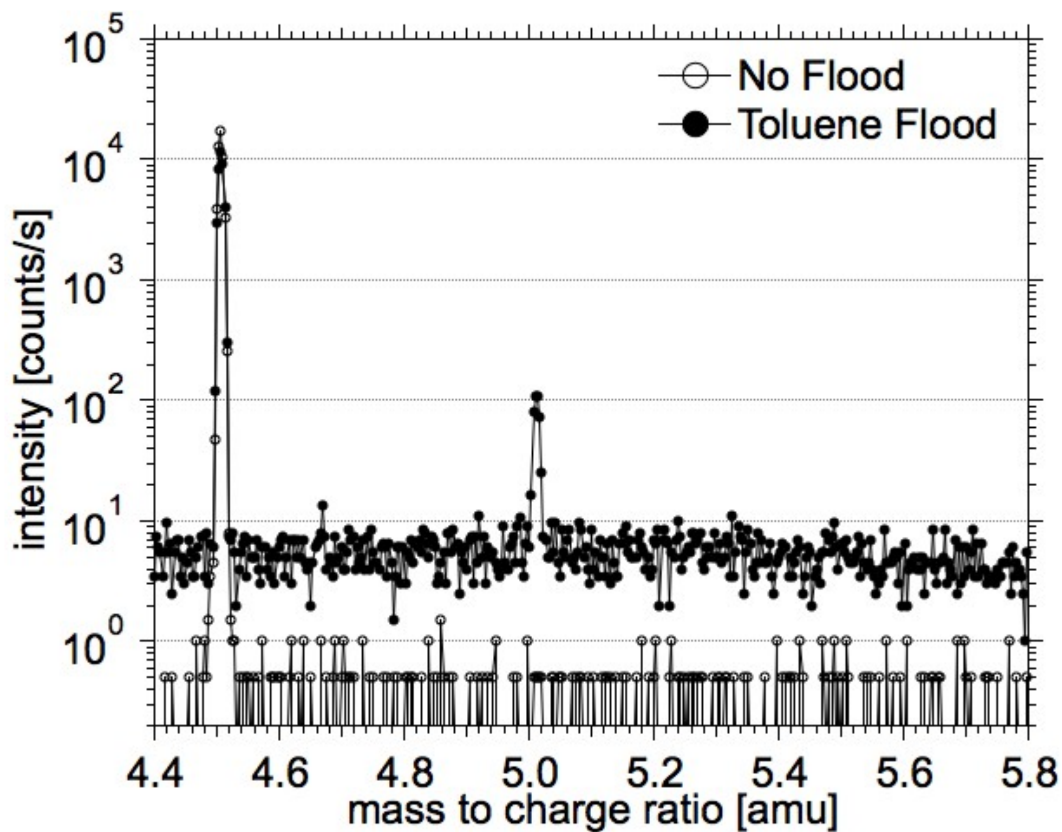

Figure 2.8. Two positive ion mass spectra obtained by sputtering beryllium metal with 8KeV Ar^+ primary ion beam with (closed circles) and without (open circles) exposure to toluene vapor at the sample surface. The primary ion beam current was 1.5μA with a 250μm square raster. Toluene vapor was introduced with flood pressure $3x10^5$torr at the sample surface.

The homonuclear ions Mo_2^{2+} and Mg_2^{2+} were also observed in mass spectra made by sputtering metal samples of these elements with argon ion beams. The small peaks at half mass were previously observed in mass spectra of argon sputtered molybdenum for the purpose of observing the diatomic argon ion Ar_2^+ (Franzreb 2003). The small peaks at m/z=94.5 and 95.5 are two of the many observable Mo_2^{2+} isotopomers in the mass spectrum of figure 2.9. An 8keV Ar^+ ion beam with 2μA beam current was used to acquire this mass spectrum. Mass spectra were measured at different sample potentials and a greater Mo_2^{2+} ion intensity was observed in mass spectra taken of gas phase ions. The mass spectrum of figure 2.9 was made using a sample potential of 4557V and an energy filter that allowed transmission of secondary ions having energies of (4500*z)±60eV. The measurement of gas phase Mo_2^{2+} ions formed away from the sample surface indicates a different formation mechanism than that of SiH^{2+}.

The many molybdenum isotopes provide a useful method for confirming the peak assignment. Table 2.1 provides theoretical peak intensities for these dications calculated from the natural isotopic abundance using a binomial expansion. The relative, background subtracted, peak intensities of the observable ions at two different sample potentials are also included in table 2.1 and good agreement with the calculated theoretical values is found.

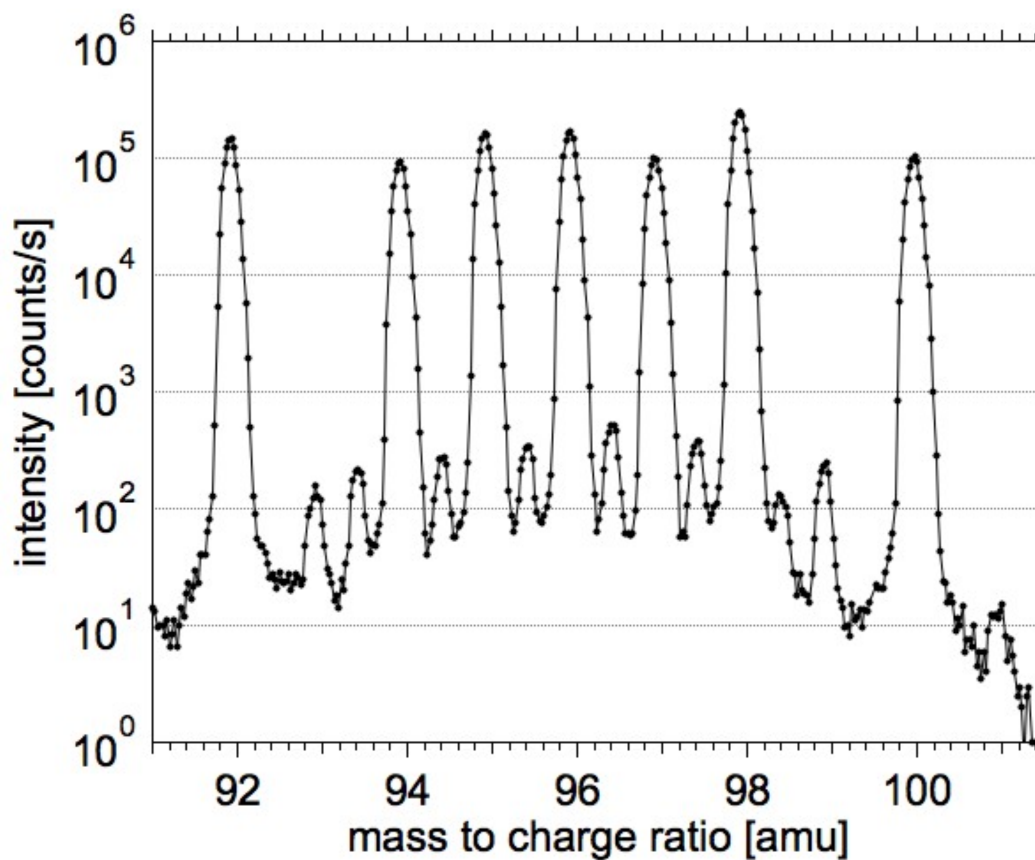

Figure 2.9. A positive ion mass spectrum showing the singly charged isotopes of molybdenum and also doubly charged molybdenum dimmers, Mo_2^{2+}. The spectrum was obtained by sputtering molybdenum foil with 8Kev Ar^+ primary ion. The sample had a potential of 4557V and the mass spectrometer was tuned to allow ions of z*(4500V ± 60eV).

Mass to charge ratio (m/z)	Theoretical abundance Mo_2^{2+} (%)	Abundance relative to m/z = 96.5 [%]		
		Theoretical	Experimental (4557V)	Experimental (4577V)
92.0	2.2	*	*	*
93.0	2.7	25	30.9 ± 2.4	32.1 ± 3.5
93.5	4.7	43	41.8 ± 2.9	42.2 ± 4.2
94.0	5.8	*	*	*
94.5	5.8	53	48.2 ± 3.3	49.6 ± 4.8
95.0	12.8	*	*	*
95.5	7.1	65	59.8 ± 3.9	62 ± 5.6
96.0	13.1	*	*	*
96.5	10.9	100	100 ± 5.3	100 ± 7.5
97.0	10.8	*	*	*
97.5	7.7	71	69.2 ± 4.2	73.6 ± 6.1
98.0	9.1	*	*	*
98.5	1.8	17	19.6 ± 2.2	19.3 ± 3.1
99.0	4.7	43	52.6 ± 3.2	46.1 ± 4.2
100.0	0.9	*	*	*

Table 2.1. Theoretical and experimental abundance of Mo_2^{2+}. The theoretical abundance of each possible Mo_2^{2+} is calculated from the natural isotopic abundance of molybdenum. Experimental intensities and theoretical abundances are reported ratios of each value to that of the m/z =96.5 value as a percent. Those labeled as * are unobservable in the mass spectrum due to intense monatomic molybdenum ion peaks.

The magnesium dications, Mg_2^{2+}, ions were similarly produced by sputtering magnesium metal with 1μA of an 8keV argon ion beam. The Mg_2^{2+} ion peaks are seen at m/z = 24.5 and 25.5 in the mass spectrum of figure 2.10. The background subtracted peak intensity of m/z = 24.5 is 7.1 times greater than the peak intensity of m/z = 25.5. This compares well with the expected ratio of 7.2 calculated from the natural abundance and isotopic ratios. These ions were only observed with a sample offset of 4500V centered on low energy secondary ions. No gas phase Mg_2^{2+} ions were detectable above the background. The ions were not observed in mass spectra made with lower sample potentials either due to a large background from scattered ions or fragmented metastable ions.

Chromium and tungsten samples were similarly investigated by sputtering the metals with high current argon ion beams. No doubly charged diatomic cations were observed above the background detection limit.

2.5 Mechanism of formation of Mo_2^{2+}

An energy profile was not a practical method for investigating the formation mechanism of the Mo_2^{2+} ions. Narrowing the energy filter to sample discrete energies decreases the secondary ion intensity and the intensity of the dications is already low. A pseudo, or low energy resolution, energy profile was constructed instead by measuring mass spectra at different sample potentials with the energy filter centered on (4500*z) but opened to allow ions within ±60eV to pass

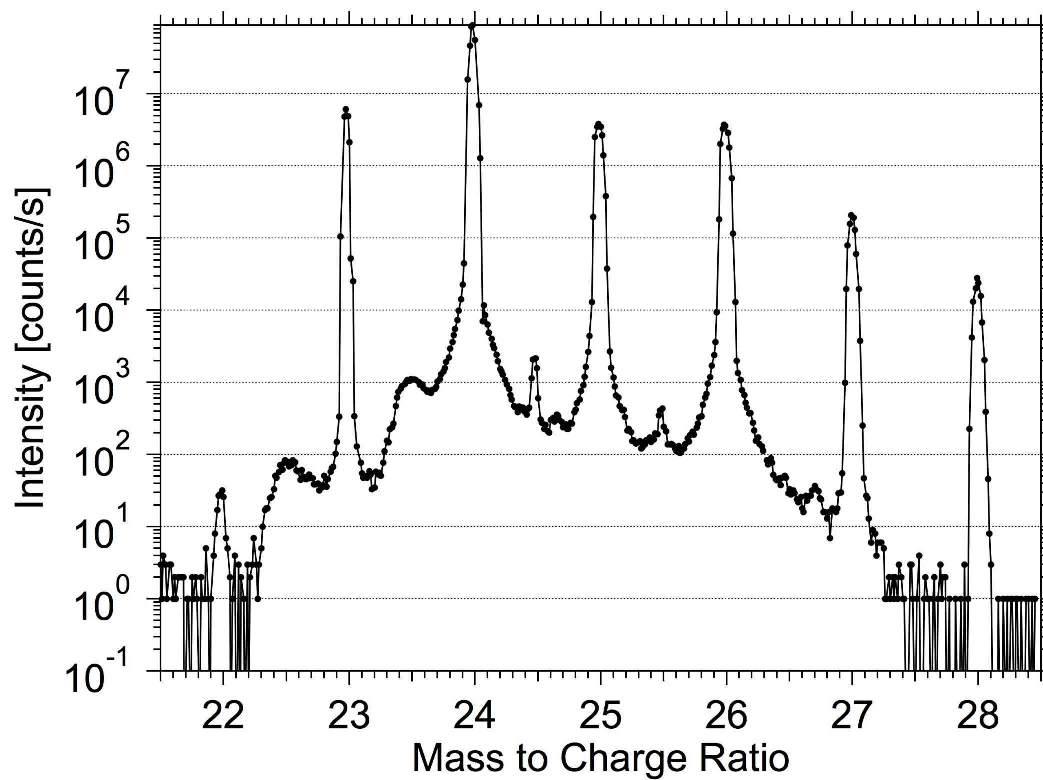

Figure 2.10. A mass spectrum of magnesium acquired by sputtering magnesium with 8 KeV Ar^{+} primary ion. The primary ion beam had a current of 1 μA and a 250 μA square raster. The energy slit was aligned to allow transmission of ions having 4.5keV ±60eV (*z) and sample potential was 4500V.

The four mass spectra used to construct the pseudo energy profile are shown in figure 2.11 with the sample potential indicated for each. The four mass spectra are shown on an arbitrary intensity scale for comparison. The relative intensities of the peak intensities in the four mass spectra are not preserved in figure 2.11. The pseudo energy profiles of four Mo_2^{2+} peaks in figure 2.12 are created from the background subtracted ion intensities of these peaks in the mass spectra of figure 2.11. The width of the energy window (± 60eV) can be seen in the measured ion intensities with a sample potential of 4542V. With this sample potential, the energy slit is centered for transmission of gas phase ions but the ±60eV width of the energy slit also includes low energy sputtered ions.

The $^{90}Mo^+$ ion is formed at the sample surface and the intensity of this ion at 4542 is high due to the large width of the energy slit. Energy profiles of intense peaks of ions formed at the surface often have a shoulder that would appear to be gas phase ions. This shoulder in the energy profile is actually due to scattering in the spectrometer and is exaggerated in the pseudo energy profile due to the large width of the energy slit.

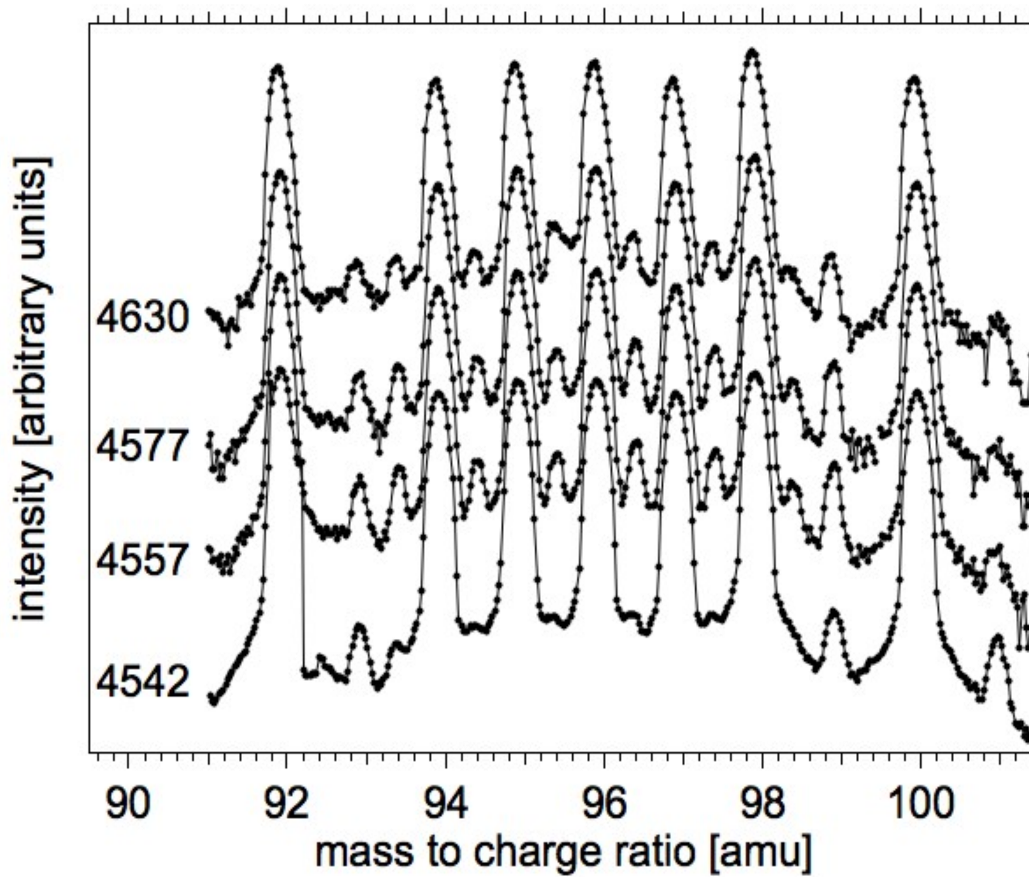

Figure 2.11. Four mass spectra as per figure 2.9 but with varying sample potentials. Each of these mass spectra was obtained by sputtering molybdenum foil with 8KeV Ar^+ primary ions with sample different sample potentials. The spectrometer was tuned to allow transmission of secondary ions with an energy of z*(4500±60) eV. The intensity scale is arbitrary.

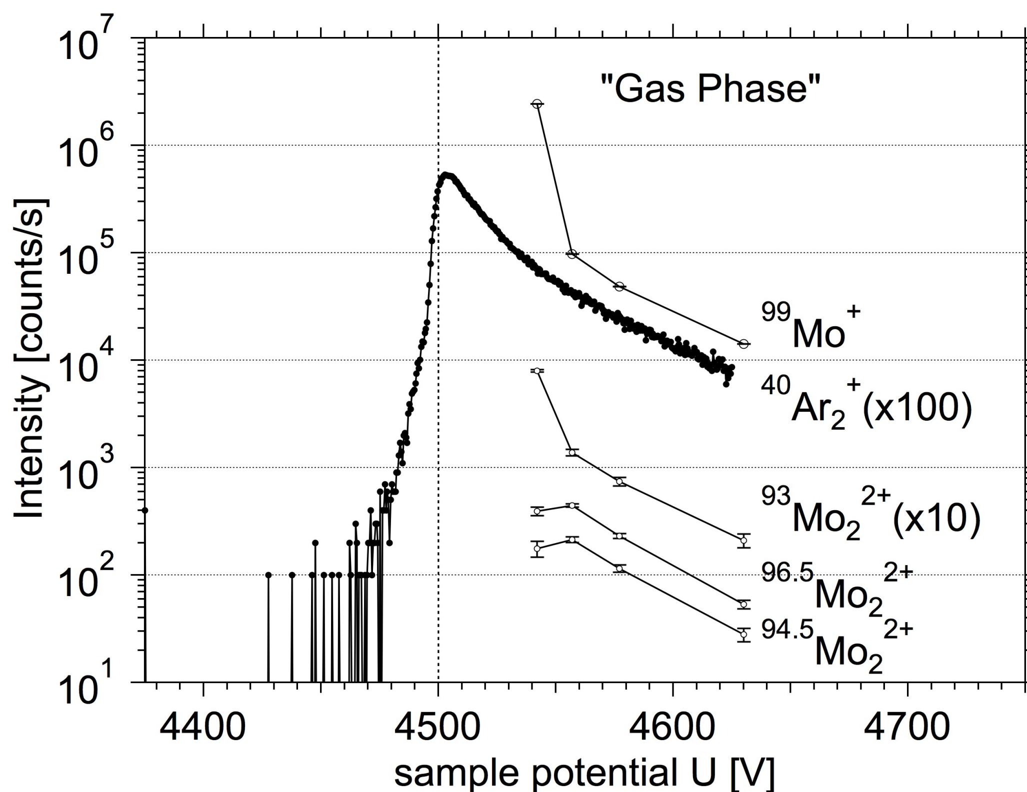

Figure 2.12. A pseudo energy profile of three Mo_2^{2+} isotopomers at m/z = 93, 94.5 and 96.5. The pseudo energy profiles were made from measured background subtracted ion intensities in mass spectra made using different sample potentials with the energy slit positioned to allow transmission of ions having energies of 4.5keV ±60eV (*z). Error bars are propagation of errors on background subtraction with puissant statistics used for peak and background. A pseudo energy profile of $^{99}Mo^{+}$ is also included from data obtained in the same mass spectra. For comparison, an energy profile of Ar_2^{+} from argon sputtered beryllium metal is included. The argon dimer energy profile was made with the energy slit positioned to allow transmission of ions having energies of 4.5keV ±10eV (*z).

The pseudo energy profiles of the Mo_2^{2+} ions indicate that they are formed in the gas phase only. The pseudo energy profiles of these ions are similar to the energy profile of the argon cluster ion at higher sample offsets. At 4542V the intensity of the Mo_2^{2+} ions at m/z = 94.5 and 96.5 is less than observed at 4557V because these ions are not formed at the sample surface. The Mo_2^{2+} ions at m/z = 93 are observable with higher offsets at this even mass number due to the lack of a molybdenum isotope at this mass. At the 4542V offset, a mass interference with the sputtered $^{92}MoH^+$ ion is observed by the increased intensity compared to the 4557 offset.

The diatomic argon ion, Ar_2^+, is formed away from the surface. The mechanism is believed to be an electron transfer from incident primary argon ions and neutral sputtered argon dimers (Franzreb 2003). At a distance of 100μm from the sample surface, the argon dimer is formed with easily measureable intensity. The pseudo energy profiles of $^{94.5}Mo_2^{2+}$ and $^{96.5}Mo_2^{2+}$ resemble the energy profile of the argon dimer and indicate the possibility of a similar formation process.

The proposed mechanism of formation of the Mo_2^{2+} is a resonant electron transfer between the incident argon ions and singly charged Mo_2^+ sputtered from the surface:

$$Ar^+ + Mo_2^+ \rightarrow Ar + Mo_2^{2+}$$

To test the idea of a resonant electron transfer between the argon ion and the singly charged molybdenum dimer, a similar mass spectrum of the

molybdenum was made using a xenon ion beam. Mass spectra of the molybdenum sample made using both xenon and argon ion beams with a 4630 sample offset are shown in figure 2.13. The lack of secondary Mo_2^{2+} ions in the xenon sputtered flux supports the resonant electron transfer mechanism in the argon ion beam experiments.

A similar pseudo energy profile could not be constructed for the Mg_2^{2+} ions because they were only observable at one sample potential.

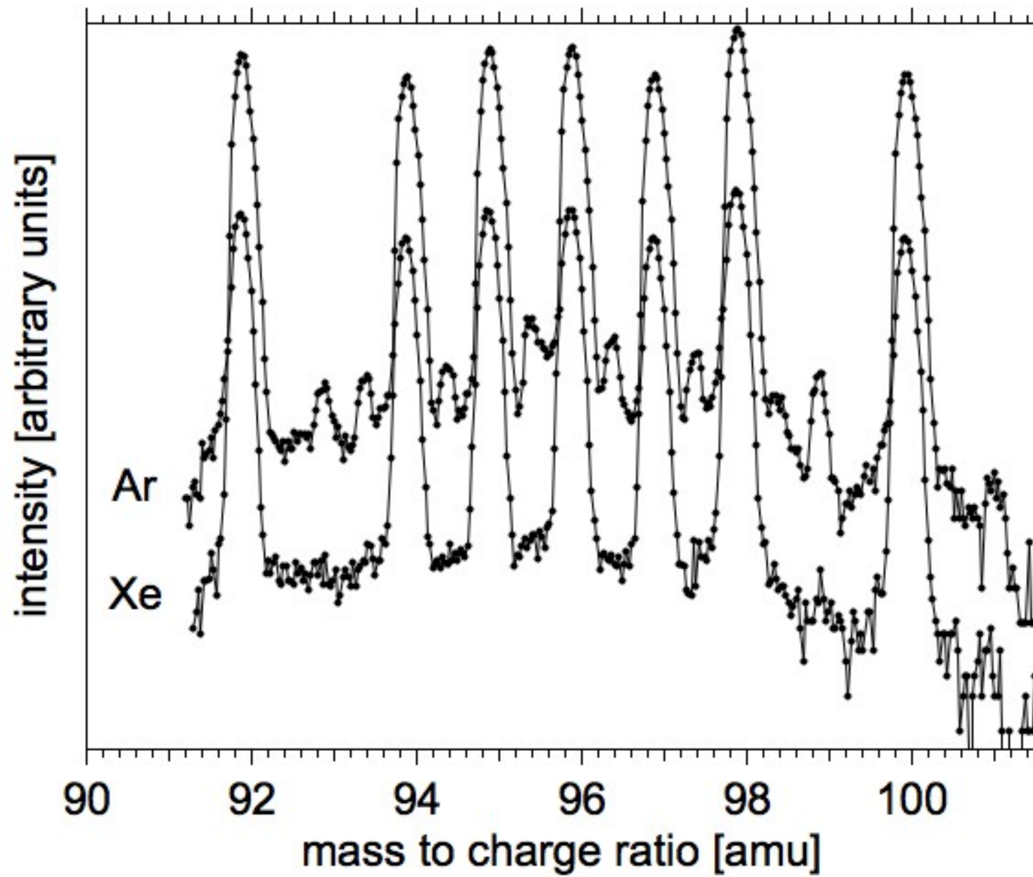

Figure 2.13. Two mass spectra obtained by sputtering of molybdenum foil; one with 8KeV Ar^+ primary ion and the other with 5.5 KeV Xe^+ primary ion. Each spectrum was acquired with a sample potential of 4630V with the instrument tuned to allow transmission of z*(4500 ±60) eV energy secondary ions.

2.6 Mechanism of formation of BeH^{2+}

The BeH^{2+} ion was intense enough for an energy profile measurement and this is reproduced in figure 2.14 with the energy profiles of Be^{2+} and Ar_2^+ included. Both sputtered ions and neutrals are observed in the BeH^{2+} energy profile. The sputtered ions are produced by the Auger electron emission of singly charged beryllium hydride dimers near the sample surface. No low-energy peak in the energy profile is observed due to fragmentation of high-energy ions having secondary collisions while leaving the surface.

The mechanism by which BeH^{2+} forms in the gas phase is not yet understood. The resonant electron transfer mechanism observed for the Mo_2^{2+} ion from argon sputtered molybdenum is not likely occurring in the formation of BeH^{2+}. The second ionization energy of BeH is likely greater than that of Mo_2 due to the lower valence shell. A more likely mechanism involves a collision between Be^{2+} and hydrogen atom or hydrogen containing molecule. For the dication to form in a metastable state, some collisional energy must be carried away by another particle. A three-body collision mechanism is one possibility, with M being a third body:

$$Be^{2+} + H + M \rightarrow BeH^{2+} + M$$

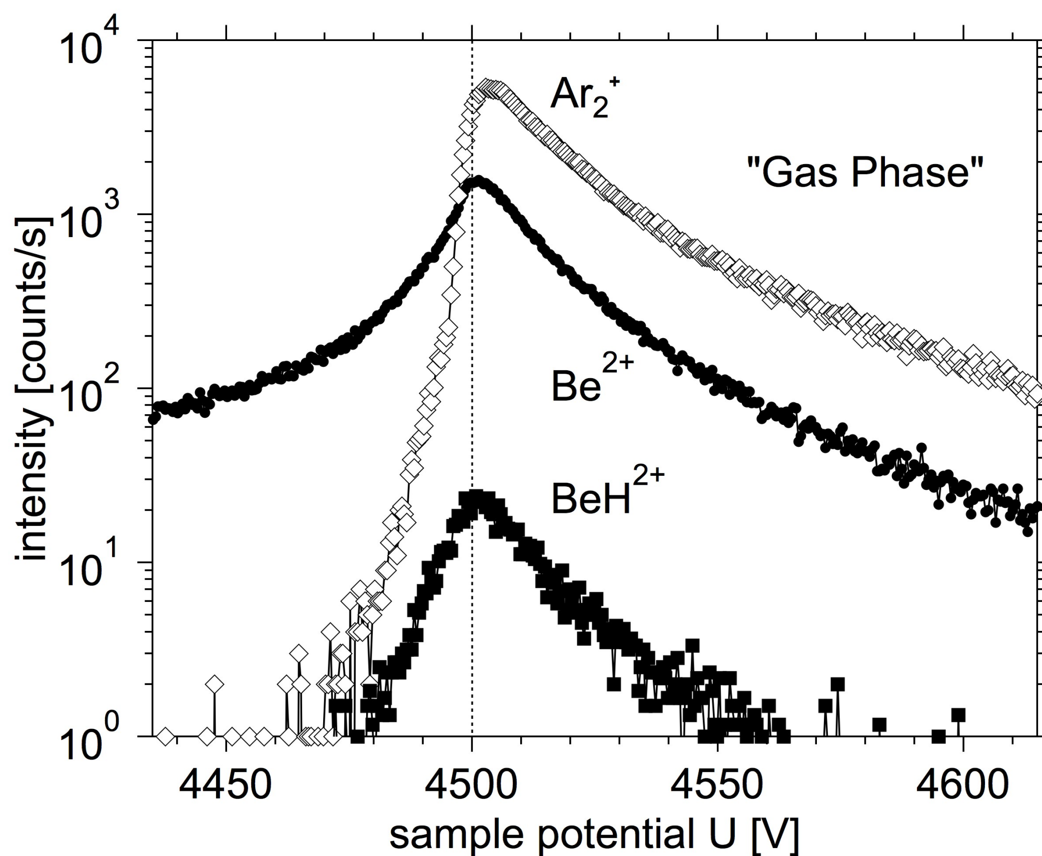

Figure 2.14. Positive ion signal intensity as a function of sample potential for BeH^{2+} (m/z = 5) produced by 8KeVAr^+ sputtering of beryllium metal exposed to toluene flooding with a pressure of $1x10^{-5}$torr. The primary ion current density was 2.2mA/cm^2 and secondary ion acquisition time was 6s per data point. Similar profiles for Be^{2+} (m/z = 4.5) and Ar_2^+ (m/z = 80), also obtained by Ar^+ sputtering of beryllium metal exposed to toluene flood, are show for comparison.

The $XeNe^{2+}$ ion has been observed to form from a three-body collision of Xe^{2+} and 2Ne atoms (Jonathon 1986, Johnson 1979). A metastable dication may also form if one of the original colliding atoms or ions is polyatomic. Fragmentation of the activated complex into the dication and a second product provides another means of removing collisional energy. A two-body collision between sputtered Be^{2+} and a polyatomic molecule possessing a hydrogen atom could form the BeH^{2+} ion:

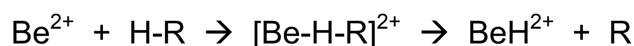

$$Be^{2+} + H\text{-}R \rightarrow [Be\text{-}H\text{-}R]^{2+} \rightarrow BeH^{2+} + R$$

The XeO^{2+} and XeN^{2+} ions have been produced in two-body collisions of Ar^{2+} with the diatomic molecules in the flight path (Jonathon 1986, Tosi 1999, Ascenzi 2003):

$$Ar^{2+} + X_2 \rightarrow ArX_2^{2+} \rightarrow ArX^{2+} + X$$

Whether the BeH^{2+} ions formed in the gas phase are the result of a two or three-body collision or some other mechanism is not resolved in the SIMS experiments.

2.7 Summary

The SIMS technique is well suited for studying small dications. Several of these ions with high charge density have been observed for the first time as sputtered secondary ions. These observations are confirmation of observations by other techniques. The AlH^{2+} has been observed for the first time. Investigation of the formation mechanism of these ions is also possible using the SIMS technique. A pseudo energy profile has shown that the Mo_2^{2+} ion is formed at a relatively large distance from the sample surface. The lack of the molybdenum dimers in mass spectra made with a xenon ion beam confirm that the Mo_2^{2+} ion is formed by a resonant electron transfer from the Mo_2^{+} ion to the Ar^{+} ion. Energy profiles show that the SiH^{2+} and BeH^{2+} ions are formed by an Auger electron emission a few angstroms from the sample surface. The silicon hydride dication is formed exclusively by this mechanism but the beryllium hydride dication also forms at a distance from the sample surface most likely by a two or three-body collision between Be^{2+} and a hydrogen containing molecule.

2.8 References:

Ascenzi, D., Franceschi, P., Tosi, P., and Bassi, D., Kaczorowska, M., Harvey, J. M. (2003). Bond-forming reactions of dications: Production of ArO^+ and ArO^{2+} in the reaction of Ar^{2+} with O_2. *Journal of Chemical Physics, 118*, 2159 - 2163.

Franzreb, K., Williams, P. (2003). Inert gas clusters ejected from bursting bubbles during sputtering. *Physical Review Letters, 91*, 015501 - 015504.

Franzreb, K., Sobers Jr., R. C., Lörinčik, J., Williams, P. (2004a). Formation of doubly positively charged diatomic ions of Mo_2^{2+} produced by Ar^+ sputtering of an Mo metal surface. *Journal of Chemical Physics, 120*, 7983 - 7986.

Franzreb, K, Sobers Jr., R. C., Lörinčik, J., Williams, P. (2004b). Detection of the diatomic dications SiH^{2+} and AlH^{2+}. *Applied Surface Science, 231-232*, 82 - 85.

Franzreb, K., Sobers Jr., R. C., Lörinčik, J., Williams, P. (2005). Observation of small long-lived diatomic dications BeH^{2+} and BeD^{2+}. *Physical Review A, 71*, 024701-1 – 024701-4.

Gill, P. M. W. (1988). How does a dication lose a proton. *Journal Of The American Chemical Society, 110*, 5311 - 5314.

Guilhaus, M., Brenton, A. G., Beynon, J. H., Rabrenović, M., Ragué Schleyer, P. von (1984). First observation of He_2^{2+}: charge stripping of He_2^+ using a double-focusing mass spectrometer. *Journal of Physics B, 17*, L605 - L610.

Jonathon, P., Boyd, R. K., Brenton, A. G., Beynon, J. H. (1986). Diatomic dications containing one inert gas atom. *Chemical Physics, 110*, 239 - 246.

Johnson, R., Manfred, B. (1979). Thermal-energy charge transfer, fiuenching, and association reactions of doubly charged ions in the rare gases. *Physical Review A, 20*, 87 - 97.

Joyes , P. P. (1968). Èvaluation théorique de la pulvérization cathodique isotrope. *Journal de Physique, 29*, 774 - 790.

Joyes, P. P. (1969). Ètude théorique de l'émission ionique secondaire. *Journal de Physique, 30*, 365 - 376.

Nefedova, W., Boldyrev, A.I., Simons, J. (1995). Ab-initio energies and tunneling lifetimes of the doubly-charged AH(2+) (A=Mg-Ar). *International Journal of Quantum Chemistry, 55,* 441 - 457.

Pauling, L. (1933). The normal state of the helium molecule ions He_2^+ and He_2^{2+}. *Journal of Chemical Physics, 1*, 56 - 59.

Schauer, S. N., Williams, P. (1990). Elimination of cluster interferences in secondary ion mass spectrometry using extreme energy filtering. *International Journal of Mass Spectrometry and Ion Processes, 103*, 21 - 29.

Schauer, S. N., Williams, P. (1992). Doubly charged ions of fourth-row elements. *Physical Review B, 46*, 15452 - 15464.

Tosi, P., Correale, R., Wenyun, L., Stefano, F., Bassi, B. (1999). Production of the molecular di-cation ArN^{2+} in the Reaction Ar^{2+}+ N_2. *Physical Review Letters, 82*, 450 - 452.

Weathers, D. L., McDaniel, F. D., Matteson, S., Duggan, J. L., Anthony, J. M., Douglas, M. A. (1991). Triply-ionized B_2 molecules from a tandem accelerator. *Nuclear Instruments and Methods in Physics Research B, 56/57*, 889 - 892.

Wittmaack, K. (1979). Ionization mechanism of H^+ sputtered from hydrogenated silicon. *Physical Review Letters, 43*, 872 - 875.

Wittmaack, K. (1980). Comparison of ion-excited auger electron emission and secondary ion emission from silicon bombarded with noble gas ions. *Nuclear Instruments and Methods, 170*, 565 - 569.

CHAPTER 3

MEASUREMENTS OF SPUTTERED SURFACE OXYGEN CONCENTRATION, SILICON SPUTTER YIELDS AND ION YIELDS

3.1 The Use of Oxygen in SIMS

Presented here is a minor isotope implant method for measuring the concentration of oxygen at the sample surface during steady state sputtering of silicon with primary oxygen ion beams. The minor isotope method allows for in-situ measurement of the surface oxygen concentration from the topmost monolayers where secondary ions originate. Oxygen was observed by Slodzian (1966) to increase positive secondary ion yields and the use of oxygen remains a common practice in SIMS. The secondary ion yield is the fraction of atoms of an element sputtered as a particular ionic form. Unless specified otherwise, the secondary ion yield of an element X generally implies monatomic anions or cations, $X^{\pm}$ but secondary ion yields of polyatomic ions such as SiO^{+} can also be measured.

Increased secondary ion yields improve the detection limit of the SIMS technique. With good ion yields it is possible to achieve sub-part per million detection limits in SIMS. Measured secondary ion yields are also reduced by the transmission efficiency of the spectrometer. The useful ion yield, UY ($X^{\pm}$), is the fraction of the atoms of element X sputtered as ions and detected.

Oxygen also surprisingly increases negative ion yields. The authors who first reported this (Lewis 1973) appeared to have used oxygen in negative SIMS analysis without realizing the significance of the increased negative ion yields. Later the significance was noted and confirmed (Williams 1978) with a study of increased negative secondary ion yields for several elements when oxygen is used as a primary ion beam or the sample is exposed to oxygen gas during sputtering.

Cesium is typically used to increase negative secondary ion yields rather than oxygen. High yields of negative secondary ions were first observed for several metals sputtered with a cesium beam by Krohn (1962) and later shown to increase ion yields of minor elements within a sample by Williams (1977). Electronegative and electropositive elements are used in SIMS to increase positive and negative secondary ion yields respectively (Anderson 1970). These "reactive species" may be introduced to the sputtered surface by the primary ion beam or a flood gas may be introduced to the sample chamber where it adsorbs to the sputtered surface.

In this study the surface oxygen concentration of silicon sputtered with primary oxygen ion beams was measured using a silicon sample implanted with a minor isotope of oxygen, ^{18}O. The sputtered surface oxygen concentration was varied using primary oxygen ion beams of different impact energies and angles. Several isotopes of other elements were co-implanted with ^{18}O in the silicon sample. The implant sample was

prepared by Leonard Kroko, Inc. The positive secondary useful ion yields of several elements were measured simultaneously with the surface oxygen concentration in each depth profile experiment. The silicon sputter yield and its dependence on the surface oxygen concentration were also measured.

3.2. The ^{18}O Implant in Silicon Method For Measurement of Oxygen Concentration at the Sputtered Silicon Surface

Measurement of the concentration of oxygen at the sputtered sample surface is facilitated by SIMS depth profile measurements of a silicon sample implanted with a known dose of ^{18}O isotope. The Williams' group has previously reported this technique (Franzreb 2004, Sobers 2004). A sputter depth profile of the ^{18}O in silicon implant standard is shown in figure 3.1. The figure includes three of the secondary ion intensities measured during this SIMS depth profile acquired using an 8keV O^+ primary ion beam. Steady state sputtering is indicated by the nearly constant secondary ion intensity of the silicon matrix, $^{28}Si^+$, and the primary ion beam isotope, $^{16}O^+$, in figure 3.1. The distribution of implanted ^{18}O atoms with depth is seen by the changing secondary ion signal with time.

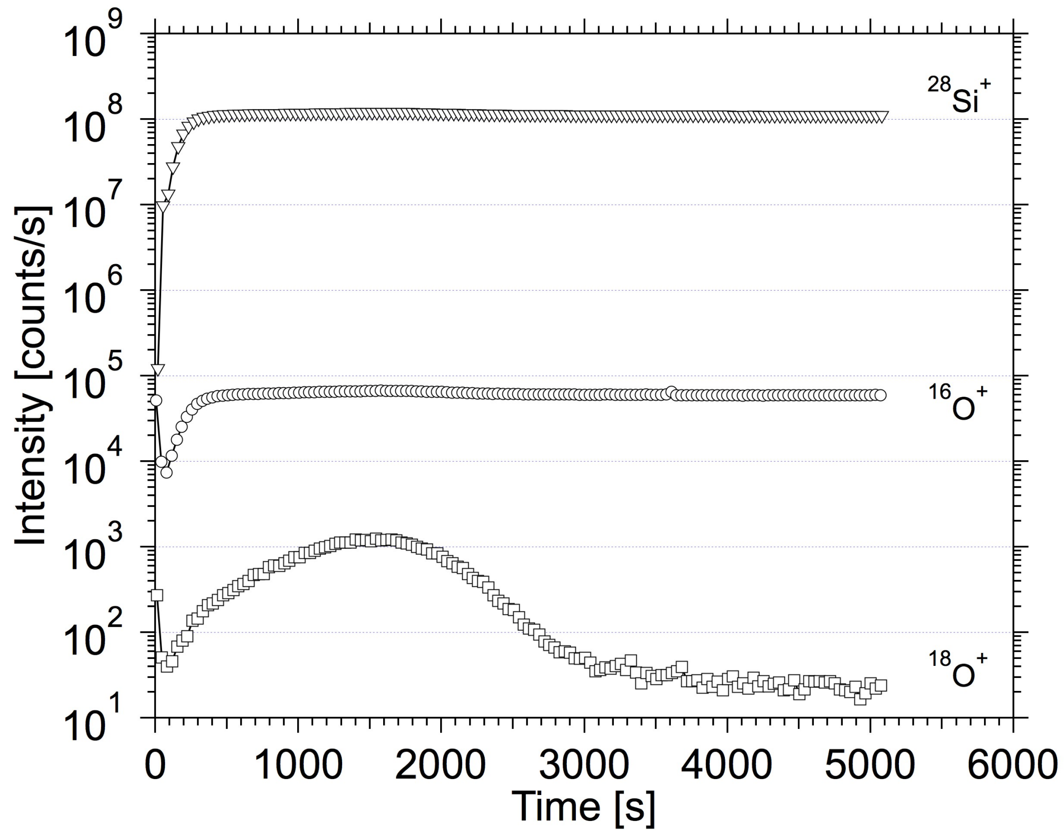

Figure 3.1. A positive SIMS depth profile of an ^{18}O implanted silicon standard. The sample contains several implanted isotopes. The depth profile was made by sputtering the silicon sample with an 8 keV O^+ primary ion beam operated with a 250μm square raster and a 69nA current. Only three of the measured secondary ions are included in this figure. The secondary ions were measured from a 63μm diameter at the center of the sputtered crater and each data point is a 2s measurement of secondary ion intensity.

Determination of the oxygen concentration (or density), C, at the sample surface during a depth profile measurement is made from the ratio of secondary ion intensities of both oxygen isotopes. With identical chemical and physical properties (disregarding the slight difference in atomic mass) the ion yield of both isotopes is the same to within 1%. The ratio of the abundance of the two isotopes at the sample surface from which secondary ions originate is the same as the ratio of the secondary ion intensities. The method is applied by taking the ratio of the steady state, average secondary intensities, I, of $^{16}O^+$ and $^{18}O^+$ and the ^{18}O atom concentration at the peak of the implant profile.

$$C(^{16}O)_{surface} = \frac{I\,(^{16}O^+)}{I\,(^{18}O^+)_{peak}} C(^{18}O)_{peak}$$

For the depth profile of figure 3.1, the source of the surface oxygen atoms, ^{16}O, is the primary oxygen ion beam. The same method is applicable to surface oxygen concentration measurements during depth profiles in which oxygen is introduced to the sample surface by way of oxygen flood gas in the sample chamber.

The peak of the ^{18}O implant profile is used because it is has the greatest secondary ion intensity above any background and is easily recognizable. The peak of the other implanted isotopes is likewise used for useful ion yield measurements. The first depth profile experiments of the implant standard were for the purpose of measuring the atom density at the peak of the implant profiles of each isotope.

3.3. Characterization of the ^{18}O Implant in Silicon Sample

The implanted atoms of each isotope are distributed over a range of depths with the peak of the distribution dependent on the impact energy during the implantation process. The implantation energy is typically an order of magnitude greater than the primary beam energies used in SIMS and the peak of the distributed implanted atoms is hundreds of nm deep. Figure 3.1 illustrated the ^{18}O method for measuring surface oxygen concentrations during a SIMS depth profile. The same SIMS depth profile is shown again in figure 3.2 but with more of the measured secondary ion intensities included. With known peak atom densities of each isotope and an accurately measured sputter rate, this one SIMS depth profile experiment provides both the sputtered surface oxygen concentration (using the ^{18}O implant) and also the useful ion yields of each implanted element (including oxygen).

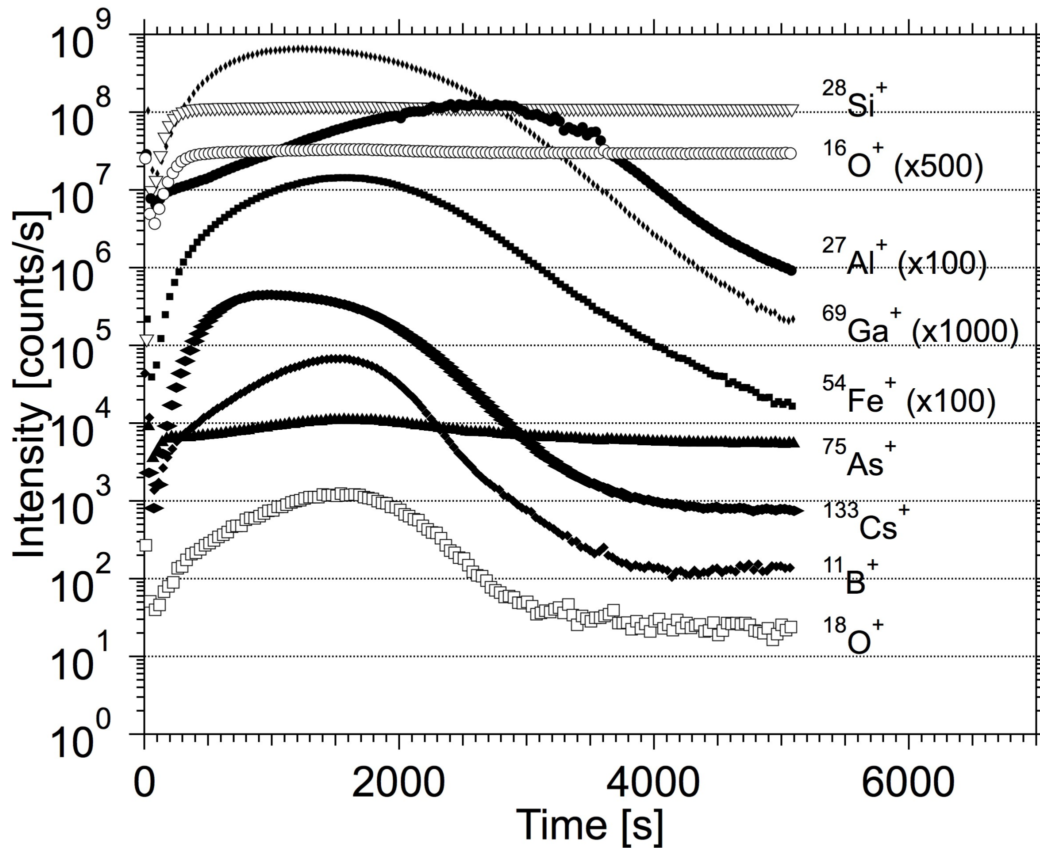

Figure 3.2. A positive secondary ion sputter depth profile of silicon implanted with several isotopes obtained with an 8 keV O^+ primary ion beam. The primary ion beam was operated with a 250μm square raster and a 69nA current. For clarity, the measured intensity of ^{54}Fe, ^{16}O, ^{27}Al and ^{69}Ga have been multiplied by values of 100, 500, 100 and 1000 respectively. Secondary ions were measured from a 63μm diameter at the center of the sputtered crater and the intensity was measured for 2 seconds for each data point. Ions of 4500V ± 60V were transmittable and the sample voltage was 4460V to decrease gas phase ions detected.

Initial SIMS depth profiles of the implanted silicon sample were made for the purpose of determining the atom densities at the peaks of the implanted profiles. The peak atom densities were found by recognizing that useful secondary ion yields are constant over any depth during steady state sputtering conditions. The useful secondary ion yield, UY, of an element X, is the fraction of the number of atoms, n, of that element (or isotope) sputtered that are measured as ions:

$$UY(X^+) = \frac{n(X^+)}{n(X)}$$

Useful secondary ion yields may be measured using the total implant depth profile. The sample must be sputtered to sufficient depth to ensure that all implanted atoms are removed. Using this method, the useful ion yield is determined from the implanted dose in the sputtered area and the integrated secondary ion intensities over the depth range of the implanted isotope.

$$UY(X^+) = \frac{\Sigma\, I(X^+)}{[\text{dose}(X)] \bullet [\text{Area Sputtered}]}$$

At the peak of an implant profile (or any depth interval), the useful ion yield is the ratio of the secondary ion intensity to the number of atoms sputtered over that depth range. If the atom density of the implanted element or isotope, C(X), is known at any particular depth interval, Δz, in the profile, then the useful ion yield may be determined from just that region of the implant:

$$UY(X^+) = \frac{I(X^+)_{\Delta z}}{C(X)_{\Delta z} \bullet [\text{Volume}]_{\Delta z}}$$

These two considerations of useful ion yield provide a means for measuring the atom density at the peak of the implant profile:

$$C(X)_{peak} = \frac{I(X^+)_{peak}}{\Sigma\ I(X^+)} \times \frac{dose(X)}{\Delta z}$$

For example, the depth sputtered between consecutive ^{18}O data points in figures 3.1 and 3.2 was determined to be 3.7nm from profilometer measurements of the sputtered crater. The total ^{18}O implant dose of 1.4×10^{16} atoms/cm^2 produced an integrated secondary ion intensity of 4.37×10^4 counts/s after background subtraction. The 1176 counts/s measured at the peak of the depth profile indicates an atom density of 1.01×10^{21} atoms/cm^3. The accepted ^{18}O implant peak atom density after repeated measurements was found to be 1.02×10^{21} atoms/cm^3. Table 3.1 provides the peak atom densities of several implanted isotopes in the sample. The depths of the ^{18}O and ^{27}Al implant peaks are also reported. These depth markers were used in later studies for sputter rate determination.

Implanted Isotope	Implanted Dose (atoms/cm^2)	Measured Peak Concentration (atoms/cm^3)	Measured Depth of Peak (nm)
^{18}O	1.40x10^{16}	1.0x10^{21} ± 6x10^{19} (10)	160±10 (6)
^{27}Al	8.30x10^{14}	4.2x10^{19} ± 3x10^{18} (14)	259±25 (9)
^{75}As	8.33x10^{14}	3.5 x10^{19} ± 2x10^{18} (8)	-
^{11}B	5.20x10^{14}	4.2x10^{19} ± 3x10^{18} (14)	-
^{133}Cs	9.00x10^{13}	3.3x10^{18} ± 2x10^{17} (7)	-
^{54}Fe	5.80x10^{14}	3.7x10^{19} ± 3x10^{18} (14)	-
^{69}Ga	5.70x10^{14}	3.2x10^{19} ± 2x10^{18} (6)	-

Table 3.1. Average measured atom densities of implanted elements in silicon at the peaks of the implant profiles. Peak atom densities were determined in part from the total implant dose (also shown). The measured implant peak depth of ^{18}O and ^{27}Al implant are also reported. These two depth markers were often used in later studies for depth scales and sputter rate determination. The uncertainty reported is the standard deviation of the mean. The number of each measurement made is included in parenthesis.

3.4. Measured Surface Oxygen Concentration and Silicon Sputter Yields For Primary Oxygen Ion Beams

The oxygen concentration at the sputtered surface is expressed here as a ratio of oxygen to silicon, O/Si. This ratio is essentially the ratio of ^{16}O/Si as ^{18}O is a minor isotope. The O/Si ratio is the ratio of O/Si atom densities:

$$\frac{O}{Si} = \frac{C(^{16}O)}{C(Si)} = \left(\frac{I(^{16}O^{+})}{I(^{18}O^{+})_{peak}}\right)\left(\frac{C(^{18}O)_{peak}}{C(Si)}\right)$$

The ratio of ^{18}O to Si atom densities at the peak of the ^{18}O implant profile, the ^{18}O/Si ratio, is 0.020 using the measured ^{18}O peak atom density (table 3.1) and the known atom density of silicon. This ratio of ^{18}O/Si is too small to increase ion yields. The O/Si ratio for the depth profile of figures 3.1 and 3.2 is calculated from the $^{16}O^{+}/^{18}O^{+}$ secondary ion intensity ratio of 52 at the peak of the ^{18}O profile after $^{18}O^{+}$ background subtraction and the ^{18}O/Si atom ratio of 0.020. The 8keV O^{+} primary ion beam used to acquire this depth profile produced an O/Si ratio of 1.0. Table 3.2 provides the average measured O/Si ratios for several primary oxygen ion beams using this method. Some of the data contained in table 3.2 was previously reported [Sobers 2004]. The O/Si measurements are made at the peak of the implant profile but reflect a steady state oxygen concentration at the surface.

Primary Ion Beam	Average Measured O/Si Ratio	Average Measured Y_{Si} [atoms/ion]	Average Measured Y_O [atoms/ion]
12.0keV, 23°, O^- (2)	4.4 ± 0.05	0.20 ± 0.01	0.88 ± 0.03
14.5keV, 24°, O^- (2)	4.2 ± 0.02	0.25 ± 0.01	1.0 ± 0.02
17.0keV, 25°, O^- (2)	3.6 ± 0.07	0.29 ± 0.01	1.0 ± 0.02
22.0keV, 26°, O^- (1)	3.7 *	0.26 *	0.98 *
13.0keV, 35°, O^+ (2)	1.5 ± 0.07	0.66 ± 0.01	0.96 *
8.0keV, 39°, O^+ (3)	1.1 ± 0.01	0.85 ± 0.03	0.94 ± 0.08
3.0keV, 52°, O^+ (3)	0.59 ± 0.01	1.9 ± 0.01	1.1 ± 0.02
17keV, 25°, O_2^- (2)	2.8 ± 0.07	0.40 ± 0.02	1.1 ± 0.09
13keV, 35°, O_2^+ (1)	1.3 *	0.77 *	1.0 *
8keV, 39°, O_2^+ (2)	0.8 ± 0	1.3 ± 0.2	1.0 ± 0.2

Table 3.2. Average oxygen to silicon ratios measured at the surface of silicon during sputtering with primary ion beams of various impact energies and angles. The impact angle from normal on the Cameca IMS 3f is determined by the angle of the primary ion column to the sample, the primary ion beam energy, and the sample potential. The $^{16}O/^{18}O$ ratio is measured at the peak of the ^{18}O implant profile after background subtraction. The silicon sputter yield was measured by measured of the volume of silicon removed and the primary ion current. Error bars are the standard deviation of the measured values. An asterisk indicates that either only one experiment is reported for that ion beam or that identical results were found for each experiment with that beam (Y_O for 13keV O^+). The number in parenthesis after each ion beam indicates the number of experiments reported here for that ion beam.

Table 3.2 also provides average measured silicon sputter yields for each primary ion beam. The sputter yield, Y, is the number of atoms sputtered per primary ion striking the surface. A partial sputter yield such as the silicon sputter yield, Y_{Si}, is the number of atoms of that species, n_{Si}, sputtered per incident primary ion, $n_{primary\ ion}$:

$$Y_{Si} = \frac{n_{Si\ sputtered}}{n_{primary\ ion}}$$

Silicon sputter yields were obtained from primary ion beam currents used during the SIMS depth profiles and the volumes of silicon they sputtered. Crater volumes were calculated from the depth and width at half height and the dimensions were measured with a stylus profilometer. Primary ion beam currents were measured using a Faraday cup located in the sample holder of the Cameca. This Faraday cup has a smaller entrance hole that minimizes the loss of secondary electrons better than the primary ion beam Faraday cup installed on the Cameca.

Figure 3.3 provides a comparison of two depth profiles of the ^{18}O in silicon implant sample obtained with different primary oxygen ion beams. The depth profile of figure 3.1, made with an 8keV O^+ primary ion beam, is reproduced here in figure 3.3 with closed symbol data points. The second depth profile, obtained with a 17keV O^- primary ion beam, is represented with open symbol data points.

The greater O/Si ratio produced by the17keV O^- primary ion beam is seen in the larger $^{16}O^+/^{18}O^+$ ratio at the peak of the ^{18}O implant and the

greater sputter rate of the 8keV O^+ beam is seen in the shorter time required to reach the peak of the ^{18}O profile implant. Changing the primary ion beam current of either beam would change the sputter rate but the O/Si ratio would remain unchanged as it depends on the partial sputter yield. The relative sputter yields of the two primary ion beams are reflected in the greater sputter rate of the 8keV O+ beam despite having roughly 60% of the current density of the 17keV O^- beam.

The sputter yield and the surface O/Si of a sample sputtered with an oxygen ion beam depend on the impact angle. More oblique primary ion beams produce sub-oxides. The critical angle has been defined as the maximum oxygen ion beam angle from normal that will produce a stoichiometric SiO_2 surface layer. Using Rutherford backscattering, RBS, the critical angle ranges from 25° to more than 30° depending on the impact energy (Deenapanray 1999). RBS measures the average bulk oxygen concentration over the several monolayers sampled and the maximum O/Si ratio observed with this technique is 2. The ^{18}O minor isotope method for measuring the surface oxygen concentration samples only the topmost monolayer from which atoms are sputtered and O/Si ratios greater than 2 have been observed (Franzreb 2004, Sobers 2004).

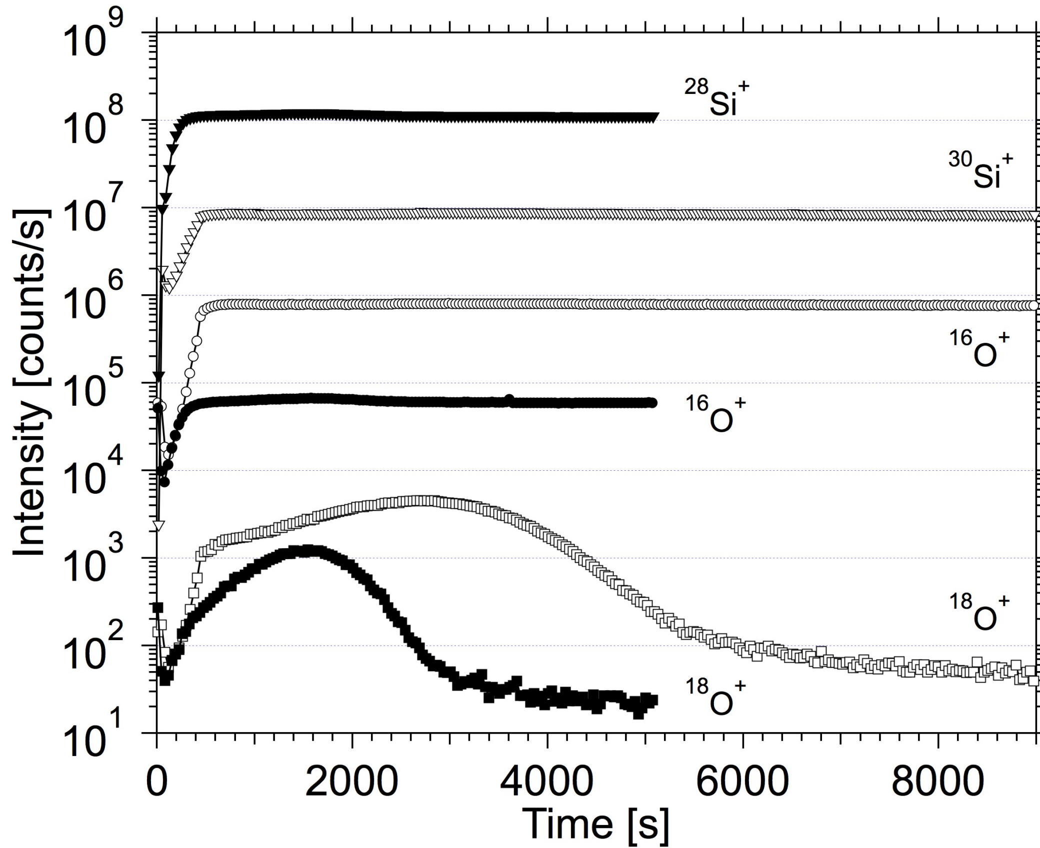

Figure 3.3. Two depth profiles of the ^{18}O implant in silicon standard. Closed symbols are secondary ion intensities measured with a 17keV O^- primary ion beam with an impact angle of 25°. Open symbols are intensities of secondary ions sputtered with an 8keV O^+ primary ion beam with an impact angle of 39°. The sputter rate of the O- beam is 56% that of the O+ beam despite a 1.6 times greater primary ion current density. Sputter rates were determined by profilometer measurements of the sputter craters. A different silicon isotope was monitored during each of the depth profiles. The oxygen to silicon ratio at the sputtered surface of the 17keV O^- ion beam experiment was found to be 3.6 and that of the 8keV O^+ ion beam experiment was 1.1.

The impact angles of the primary ion beams in the Cameca IMS 3f are ultimately defined by the kinetic energy of the primary ion beam and the electrostatic forces between the sample surface, the ion beam particles and the deflector plates used to center the impact location of the primary ion beam with the axis of the secondary column.

Oxygen atoms from a primary ion beam become chemically bound to silicon and are sputtered away by subsequent primary ion impacts. The presence of oxygen atoms at the sample surface decreases the silicon sputter yield as the probability of a silicon atom being sputtered by a primary ion beam particle decreases due to dilution. The surface oxygen concentration produced by a primary ion beam is an equilibrium condition in which oxygen enters and leaves the surface layer with equal rates:

$$\left[\mathrm{O}\right]_{eq} \text{ or } \left(\frac{\mathrm{O}}{\mathrm{Si}}\right)_{eq} = \frac{\text{rate O added}}{\text{rate O removed}}$$

Oxygen may enter the surface layer directly from primary ion beam impacts or from deeper within the sample as the surface layer recedes. A low sputter yield would be expected to produce a greater surface oxygen concentration as the slower erosion of the sample surface allows for a greater buildup of oxygen beneath the surface layer. Primary ion beams that distribute oxygen deeper within the surface increase the rate of oxygen arriving at the surface layer. The constant, steady state, surface oxygen concentration and silicon sputter yield that result ultimately depend on the impact angle and energy of the primary ion beam. If the equilibrium

at the surface layer is not achieved, then steady state sputtering does not occur.

Another condition of steady state sputtering with a primary oxygen ion beam is that the oxygen sputter yield, Y_O, must be 1. Once the surface oxygen equilibrium is established, oxygen ions entering the sample may reside in the sample for some time before being sputtered by later primary ion impacts. Over a given time interval the number of oxygen atoms added to the sample is equal to the number of oxygen atoms leaving the sample regardless of the O/Si ratio.

The ratio of oxygen to sample substrate (silicon in this study) in the sputtered flux is a ratio of the sputter yields. Each sputter yield is a measure of the number of atoms of that element sputtered per incident primary ion. As the oxygen sputter yield is 1, the O/Si ratio in the sputtered flux is inversely proportional to the silicon sputter yield:

$$\left(\frac{O}{Si}\right)_{sputtered} = \frac{Y_O}{Y_{Si}} = \frac{1}{Y_{Si}}$$

This provides a means of calculating the oxygen sputter yield for silicon sputtered with an oxygen ion beam from the measured O/Si ratio and silicon sputter yield. The partial oxygen sputter yields of all depth profile experiments represented by the averaged results in table 3.2 are well within ± 20% of 1. The oxygen sputter yield is 1 if the only source of addition of oxygen to the surface is by the primary ion beam. In experiments where a low-pressure oxygen gas is added to the sample

chamber to oxygenate the surface (Franzreb 2004), the silicon sputter yield is observed to decrease but is not inversely proportional to the O/Si ratio.

The primary ion beams in table 3.2 with more oblique angles of impact produce larger sputter yields. Larger angles from normal produce a more shallow distribution of energy closer to the sample surface. These primary ion beams also implant oxygen atoms closer to the surface and produce smaller O/Si ratios. The average sputter yield is plotted in figure 3.4 against the primary ion beam impact angle from normal. The O/Si ratios are also indicated next to the data points.

The design of the Cameca IMS 3f does not allow for adjustment of the primary ion beam impact angle independently of the energy so each impact angle in figure 3.4 has a different impact energy as indicated in table 3.2. It can still be observed that sub-oxides are produced at impact angles greater than the average critical angle of 30°. A general trend of increasing sputter yield with impact angle is also seen.

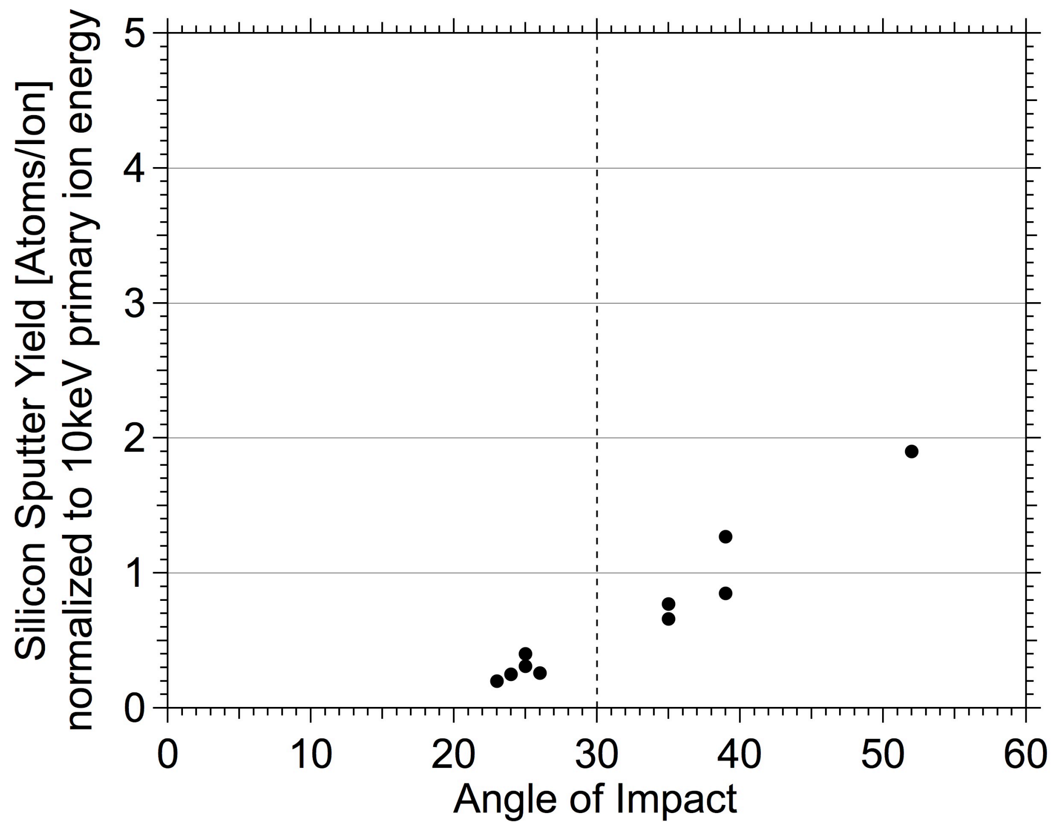

Figure 3.4. Average silicon sputter yields from bombardment with various primary oxygen ion beams. The silicon sample was close to 4.5 kV potential for all experiments. The silicon sputter yields are plotted against the impact angle of the ion beam. Monatomic and diatomic oxygen ion beams are represented by closed and open symbols respectively. The average surface oxygen concentration (reported as the oxygen to silicon atom ratio) is indicated next to the data points. Two points with no error bars, 22 keV O^- and the 13 keV O_2^+ ion beams at 26° and 35° respectively, due to only one measurement for each.

One manner in which primary ion beam impact energy and impact angle can be considered separately on the Cameca IMS-3f is to use isoenergetic diatomic and monatomic primary ion beams. Diatomic primary oxygen ion beams deliver two oxygen atoms per primary ion. On impact, a diatomic primary ion fragments, and the energy of the original primary ion is divided between the two atoms. An 8keV O_2^+ primary ion beam strikes the sample surface at the same angle as an 8keV O^+ primary ion beam but the impact energy is 4keV per oxygen atom.

The average measured silicon sputter yields reported for diatomic primary ion beams in table 2 are calculated on a per oxygen atom basis. With half the energy per impacting oxygen atom, the energy is distributed closer to the surface than is the case for a monatomic primary ion of the same energy. This results in an increase in silicon sputter yield and a decrease in the O/Si ratio. The partial oxygen sputter yields for all depth profile experiments made with diatomic primary oxygen ion beams were all within ± 20% of 1.

3.5 The Energy Dependence of the Sputter Yield

The silicon sputter yields must be normalized to a common impact angle or energy for better comparison. A generally accepted theory of sputtering is that of Sigmund (1969). This is a general theory applicable to projectile particles of all energies. Sigmund applied a power series solution to a sputter yield formula applicable to all energies and particles. With general assumptions about the projectile energy and its mass relative to the target, the equation is reduced to practical forms. For energies used in SIMS experiments (hundreds of eV to tens of keV), Sigmund considers only elastic collisions and removes electronic stopping terms from the equation. The model is linear in that it considers the collision cascade produced from one primary ion to be isolated from the rest.

Sigmund's model considers the statistical distribution of collisional energy in the topmost surface layer from which atoms are ejected and the binding energy, U, of the surface atoms. For metals the sublimation energy is used as the binding energy. Experimental data supporting the 1/U dependence predates Sigmund's equation by almost a decade. Almèn (1961) observed a periodic trend in sputter yield by sputtering different elements with primary noble gas ions having 45keV energy. Wehner (Laegreid 1961 and Rosenberg 1962) also observed the trend using lower energy (0.4keV) primary noble gas ion beams and noted the trend was similar to that of the inverse of the sublimation energy.

A convenient form of Sigmund's backward sputter yield equation for primary ion beam energies applied in SIMS analysis is provided by Steinbrüchel (1985):

$$Y=\frac{3.56}{U}\left(\frac{Z_t Z_p}{(Z_t^{2/3}+Z_p^{2/3})^{1/2}}\right)\left(\frac{M_p}{M_p+M_t}\right)\alpha\left(\frac{M_t}{M_p}\right)S_n(\varepsilon)$$

The binding energy, U, is in units of eV/atom. The atomic and mass number terms originate from Sigmund's elastic stopping power function. The subscripts t and p indicate target atom and projectile (primary ion) atoms respectively. Also originating from the elastic stopping power function is the reduced nuclear stopping power cross section, $S_n(\varepsilon)$ for which Sigmund used tabulated values. Sigmund's original equation faired poorly with low energy primary ion beams and he originally derived a separate equation for primary ion beams below 1keV energy. A better fit with experimental data over a larger range of impact energies is achieved with an equation for the reduced nuclear stopping cross section provided by Wilson (1977):

$$S_n(\varepsilon)=\frac{0.5\ln(1+\varepsilon)}{\varepsilon+0.14\varepsilon^{0.42}}$$

The reduced energy, ε, is the ratio of the kinetic energy of the projectile, E (keV), of the projectile in the center of mass system to the coulomb energy of the target and projectile atoms at the bohr radius distance:

$$\varepsilon=E/\left(0.0308\left(\frac{M_t+M_p}{M_t}\right)Z_t Z_p(Z_t^{2/3}+Z_p^{2/3})^{1/2}\right)$$

The relative masses of the target and projectile atoms are accounted for in the function $\alpha(M_t/M_p)$. A suitable equation for $\alpha(M_t/M_p)$ provided by Zalm (1983) is:

$$\alpha\left(\frac{M_t}{M_p}\right) = 0.15 + 0.13\frac{M_t}{M_p}$$

The expected energy dependent silicon sputter yields for three different primary ion beams calculated with Sigmund's theory are shown in the semi-log plot of figure 3.5. The reduced nuclear stopping cross section is responsible for the general Gaussian shape of the curve and the location of its peak but not the height of the peak. For a particular substance such as silicon, the height of the peak is due to the mass and atomic number terms in Sigmund's equation. Silicon sputter yields are greater for argon bombardment than for neon bombardment for example. Relative sputter yields of two different substances are also due to the binding energy of each. The α function is constant for a particular target and projectile combination.

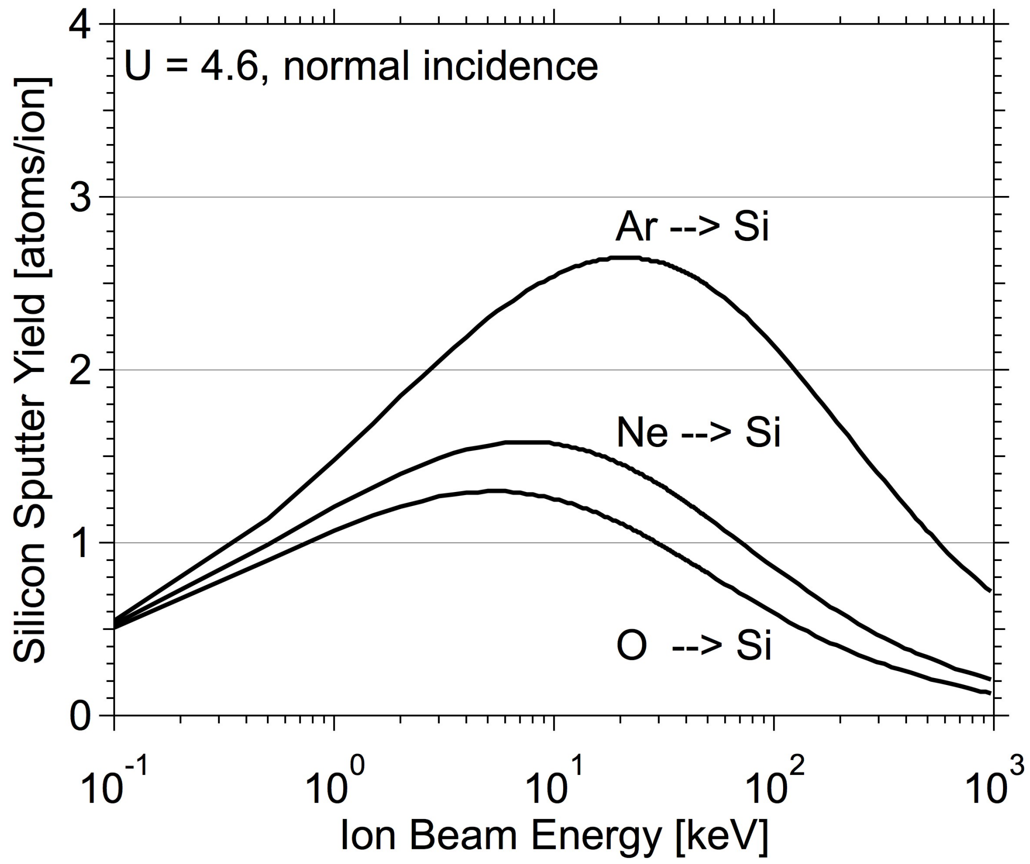

Figure 3.5. Theoretical silicon sputter yields, Y_{Si}, for three different primary ion beams vs. impact energy at normal incidence. The theoretical silicon sputter yields are calculated from Sigmund's sputter yield theory with Wilson's stopping power equation and the cohesive energy of silicon, U = 4.6 eV/atom.

3.6 The Angular Dependence of the Sputter Yield

Sigmund states that for a particular substance the sputter yield depends on the elastic stopping power and the angle of incidence, θ. The sputter yield equation above is for normal incidence. Sputter yields increase with increasing impact angle from normal up to a maximum around 70° to 80°. A $1/\cos(\theta)$ function has been used for small angles from normal but the agreement has been shown to be poor. It is recognized that a better function is:

$$Y_\theta = Y_0(\cos\theta)^{-f}$$

Slightly different values for f appropriate for SIMS have been reported in the literature. Sigmund's solutions of the general sputter yield equation produce an energy dependent value for f. A value of 5/3 for f is generally accepted for primary ion beam energies used in SIMS based on experimental data and Sigmund's theory. The theoretical angular dependence of the sputter yield is shown in figure 3.6 for sputtering of silicon with 10keV oxygen. This curve is calculated from the theoretical silicon sputter yield for a 10keV primary oxygen ion beam.

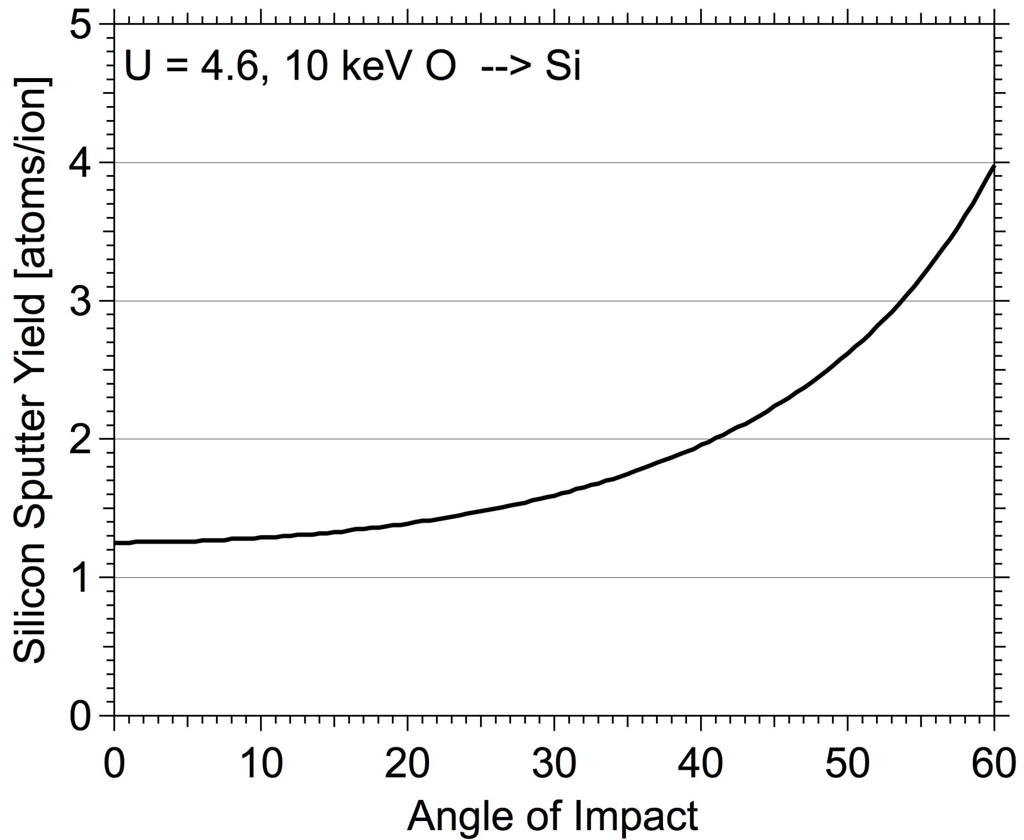

Figure 3.6. Theoretical silicon sputter yields, Y_{Si}, for oxygen primary ion beams at 10keV impact energy vs. impact angle. Theoretical silicon sputter yields are calculated using Sigmund's sputter yield theory starting with 10keV impact energy (figure 3.5) followed by adjustment for impact angle.

3.7 Normalization of Silicon Sputter Yields

Sigmund's theory was used to normalize the silicon sputter yield data in figure 3.4 in order to consider the dependence of the sputter yield on impact angle independently of energy. Each sputter yield was adjusted to its theoretical value if the impact energy of each primary ion beam used had been 10keV. The impact energy is found within the nuclear stopping power term of Sigmund's equation and the ratio of sputter yields at two energies is simply the ratio of this term at the corresponding energies:

$$\frac{Y_{Si}(10keV)}{Y_{Si}(E)} = \frac{S_n(\varepsilon_{10keV})}{S_n(\varepsilon_E)}$$

The silicon sputter yields normalized for 10keV impact energy are plotted against the experimental impact angle in figure 3.7. Circular data points are for monatomic oxygen in beams and triangular data points for diatomic primary ion beams. Two additional data points (open symbols) from a related study (Franzreb 2004) are included after similar normalization. Normalization from the experimental impact energy to 10keV increases or decreases the silicon sputter yield by only a small amount. The peak of the theoretical silicon sputter yield curve for sputtering with primary oxygen ion beams in figure 3.5 occurs close to 5keV impact energy and the theoretical silicon sputter yields of all experimental oxygen ion beam energies are fairly close.

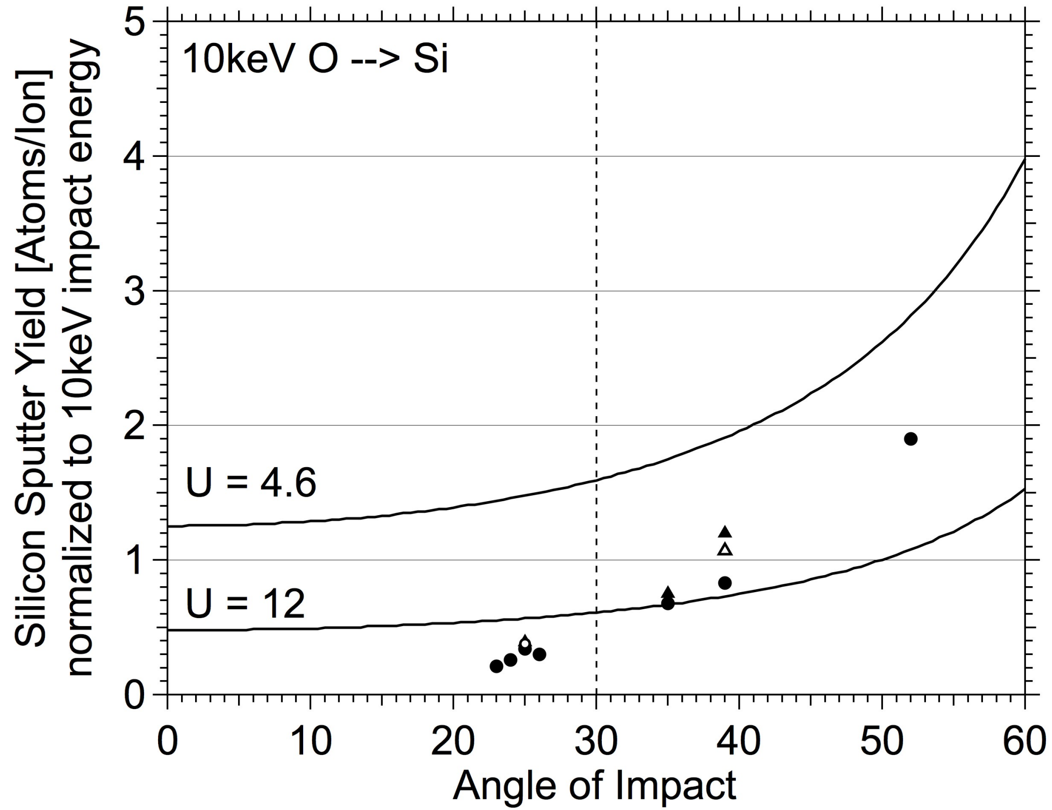

Figure 3.7. Silicon sputter yields, Y_{Si}, for 10keV $O^{\pm}$ (circles) and $O_2^{\pm}$ (triangles) primary ion beams vs. experimental impact angle. Measured average sputter yields have been normalized to 10keV impact energy using Sigmund's sputter yield theory. Silicon sputter yields from diatomic primary ions were normalized from the impact energy per atom. Open symbol data are taken from figure 4 of Franzreb 2004. The two curves are theoretical silicon sputter yields for 10keV oxygen primary ion beams calculated using Sigmund's sputter yield theory. The upper curve is calculated using the cohesive energy of silicon, U = 4.6 eV/atom, and the lower using an arbitrarily larger binding energy of U = 12eV/atom.

The same theoretical silicon sputter yield curve for 10keV primary oxygen primary ion beams using a cohesive energy of silicon (4.6eV/atom) of figure 3.5 is included in figure 3.7 for comparison. The second theoretical curve calculated with a somewhat arbitrarily larger binding energy of 12eV/atom is closer to the normalized silicon sputter yield data points and bisects the data around the average critical angle of 30°. Normalized silicon sputter yields above this theoretical curve are from oxygen ion beams with an impact angle greater than the critical angle and angles closer to normal produce normalized sputter yields below the same theoretical curve.

The dependence of the silicon sputter yield on impact energy may also be considered. The semi-log plot of figure 3.8 shows the average measured silicon sputter yields against the impact energy of the primary ion beam with the energy per atom of diatomic primary ion beams considered. The sputter yield increases with decreasing energy but the impact angle is also more oblique for the lower energy beams. To better consider the impact energy, the silicon sputter yields are adjusted to what they would be if the primary ion beams were at normal incidence by application of Sigmund's angular dependence sputter yield equation:

$$Y_{Si}^{0} = Y_{Si}^{\theta}(\cos\theta)^{5/3}$$

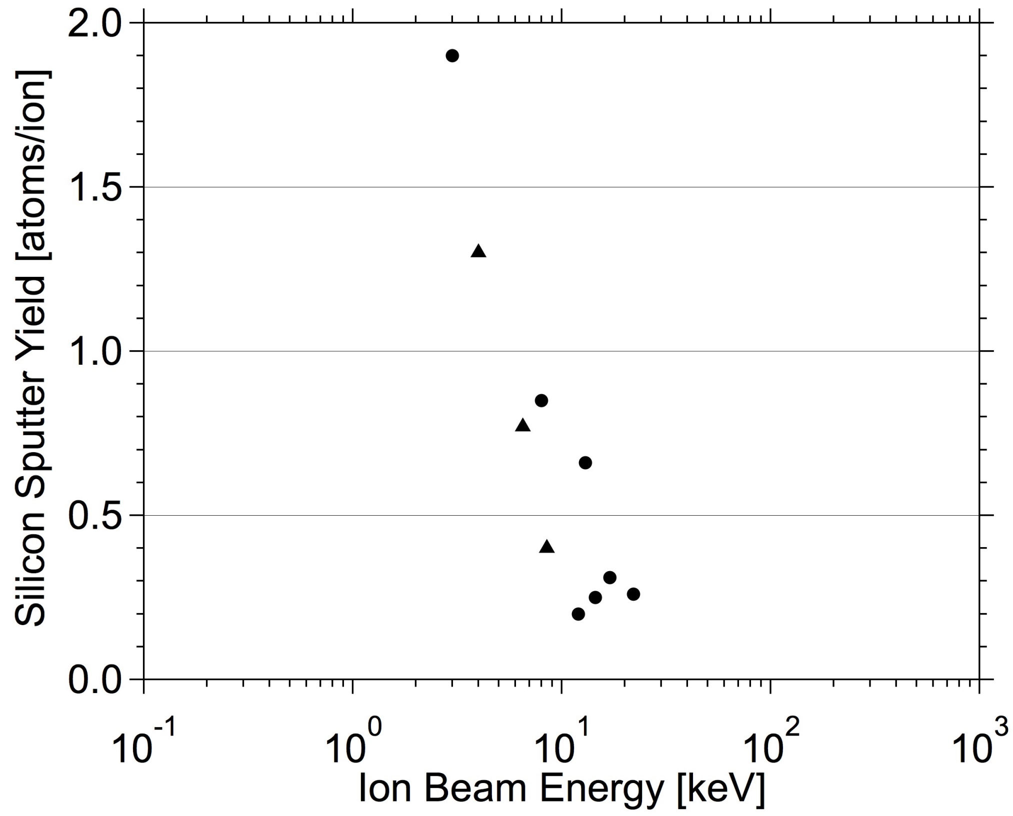

Figure 3.8. Measured silicon sputter yields, Y_{Si}, for $O^{\pm}$ (circles) and $O_2^{\pm}$ (triangles) primary ion beams vs. impact energy at experimental impact angles. Silicon sputter yields from diatomic primary ions are plotted against the impact energy per atom.

A wide range of primary ion beam angles was used in this study and the decrease in silicon sputter yield on normalization to normal incidence is greatest for more oblique angles. The normalized silicon sputter yields are plotted against the per atom experimental impact energy in figure 3.9. Open symbol data is similarly normalized sputter yields from Franzreb (2004). As with figure 3.7, the theoretical curves from Sigmund's theory for sputtering of silicon with oxygen using silicon's cohesive energy and the larger 12eV/atom binding energy are included.

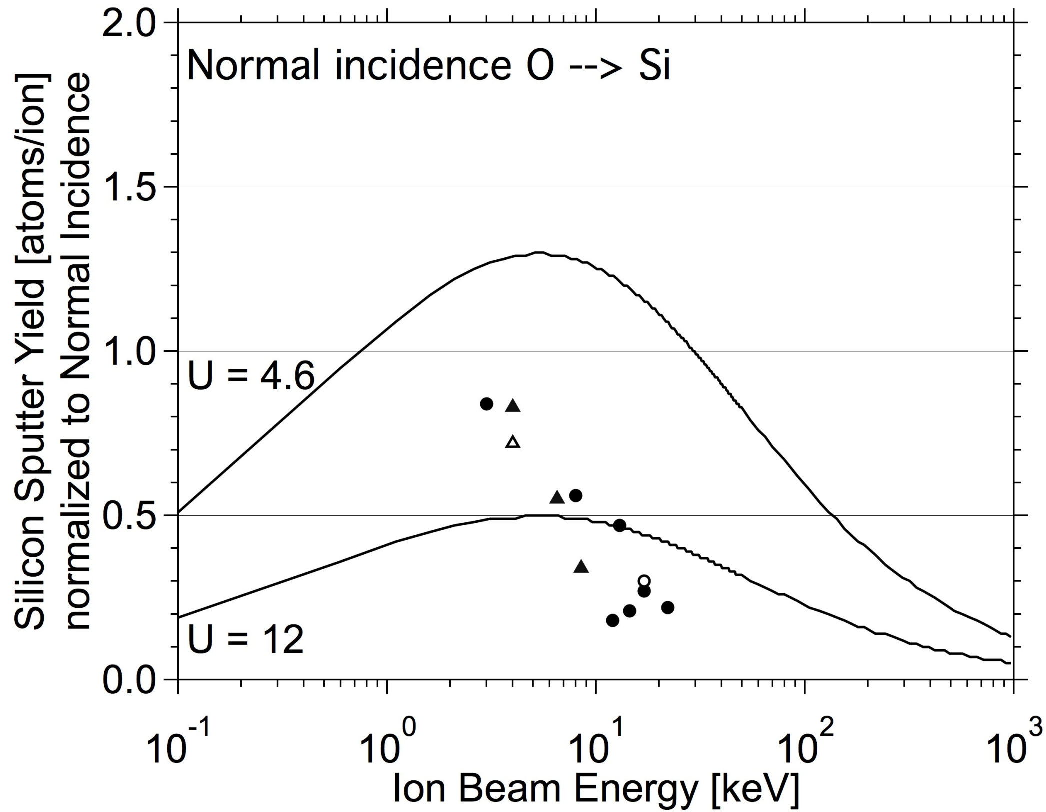

Figure 3.9. Silicon sputter yields, Y_{Si}, for $O^{\pm}$ (circles) and $O_2^{\pm}$ (triangles) primary ion beams vs. impact energy at normal incidence. Measured average sputter yields have been normalized to normal incidence using Sigmund's angular dependence formula. Silicon sputter yields from diatomic primary ions are plotted against the impact energy per atom. Open symbol data are taken from figure 4 of Franzreb 2004. The two curves are theoretical yields for oxygen primary ion beams at normal incidence sputtering silicon calculated using Sigmund's sputter yield theory. The upper curve is calculated using the cohesive energy of silicon, U = 4.6 eV/atom, and the lower using an arbitrarily larger binding energy of U = 12eV/atom.

3.8 Theoretically Oxygen Free or Clean Silicon Sputter Yields

Not surprisingly, Sigmund's sputter yield equation does not describe the normalized silicon sputter yield dependence on angle or energy as oxygenation of the sample surface decreases the sputter yield. The sputter yield theory of Sigmund is applicable to noble gas ion beams that escape the sample readily leaving a continually pure target, but even with a noble gas, the sputter yields of elements with a high affinity for oxygen are lower than expected.

Using Wehner's (Laegreid 1961 and Rosenberg 1962) 500eV sputter yield data for argon ion beams at normal incidence, Seah (1981) calculated the ratio of the experimental sputter yields to theoretical for many elements and Steinbrüchel (1985) expanded on this. For elements with a low oxygen affinity, measured as the enthalpy of reaction per gram of oxygen, the ratio is close to unity. The sputter yield of elements with greater oxygen affinity drops to less than half the predicted values.

The significant decrease in sputter yield for elements with a high oxygen affinity is shown in these early studies was due to poor vacuum. Noting this, Zalm (1983) measured the sputter yields of silicon and molybdenum with a better vacuum system and also with more accurate methods of sputter yield measurement. With the better vacuum, sputter yields of both elements, bombarded with 500eV Ar^+ primary ion beams, increased in the Zalm study and the sputter yield of silicon, having a greater oxygen affinity, increased more.

The decrease in sputter yield may be attributed to a decrease in the number of atoms of the sample in the surface layer or to the changing physical properties of the sample surface. Primary ion beams are sputtering oxygen atoms at the surface in addition to the silicon atoms. The decreased probability of a primary ion striking and sputtering an atom of the sample decreases as the fraction of oxygen atoms increases. The silicon sputter yield of an oxygenated silicon surface is also expected to be less due to increased binding energy and decreased nuclear stopping power of the oxygenated surface.

The clean sputter yield, Y^X, is the theoretical sputter yield one would expect if the oxygen were not bound to the sample surface. The calculation of clean silicon sputter yield presented here is a simple division of the normalized silicon sputter yield by the silicon atom fraction:

$$Y_{Si}^{x} = \frac{Y_{Si}}{X(Si)}$$

Division by the silicon atom fraction is meant to produce a silicon sputter yield that would result if all surface atoms were silicon. A proportionality constant of one is used in this simple approach. The ^{18}O minor isotope implant method provides the O/Si ratio at the surface layer and so lends itself ideally to this calculation and the atom fraction of silicon is easily calculated:

$$X(Si) = \frac{1}{1 + O/Si}$$

Figure 3.10 shows that the normalized silicon sputter yields for all primary ion beams increase when calculated as clean silicon sputter yields. The increase is proportionately greater from primary ion beams with impact angles less than the critical angle due to the smaller silicon atom fraction at the surface produced by these beams. The clean silicon sputter yields here are better described by Sigmund's predicted silicon sputter yields for 10keV per atom oxygen ion beams and a binding energy of 4.6eV/atom.

The same can be said of Sigmund's energy dependent predicted silicon sputter yields for oxygen primary ion beams at normal incidence and the clean sputter yields shown in figure 3.11. Here the more energetic primary ion beams produce the more oxygenated surfaces and the greatest increase in silicon sputter yield when the normalized yields are calculated as clean sputter yields. Again the data best fit the curve for U=4.6eV/atom.

The clean silicon sputter yields reported here are in good agreement with the theoretical silicon sputter yield curves produced by Sigmund's theory with a binding energy of 4.6eV/atom. The agreement of the clean silicon sputter yields with the theoretical curves made using a binding energy of 4.6eV/atom does not necessarily imply that this is the appropriate value to use.

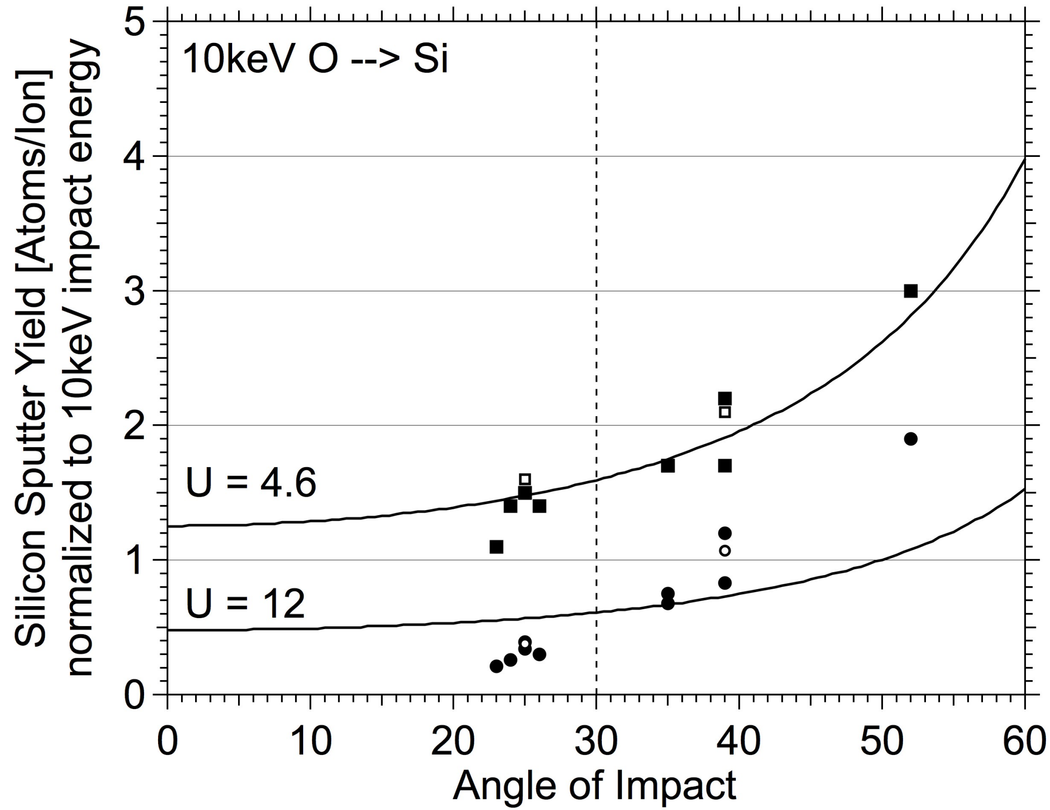

Figure 3.10. Normalized and clean silicon sputter yields calculated from measured silicon sputter yields for $O^{\pm}$ and $O_2^{\pm}$ primary ion beams vs. experimental impact angle. Circular data points are the silicon sputter yields of figure 3.7. Square data points are the corresponding clean sputter yields calculated from the normalized sputter yields. Open symbol data are taken from figure 4 of Franzreb 2004. The two curves are theoretical yields for oxygen primary ion beams at normal incidence sputtering silicon calculated using Sigmund's sputter yield theory. The upper curve is calculated using the cohesive energy of silicon, U = 4.6 eV/atom, and the lower using an arbitrarily larger binding energy of U = 12eV/atom.

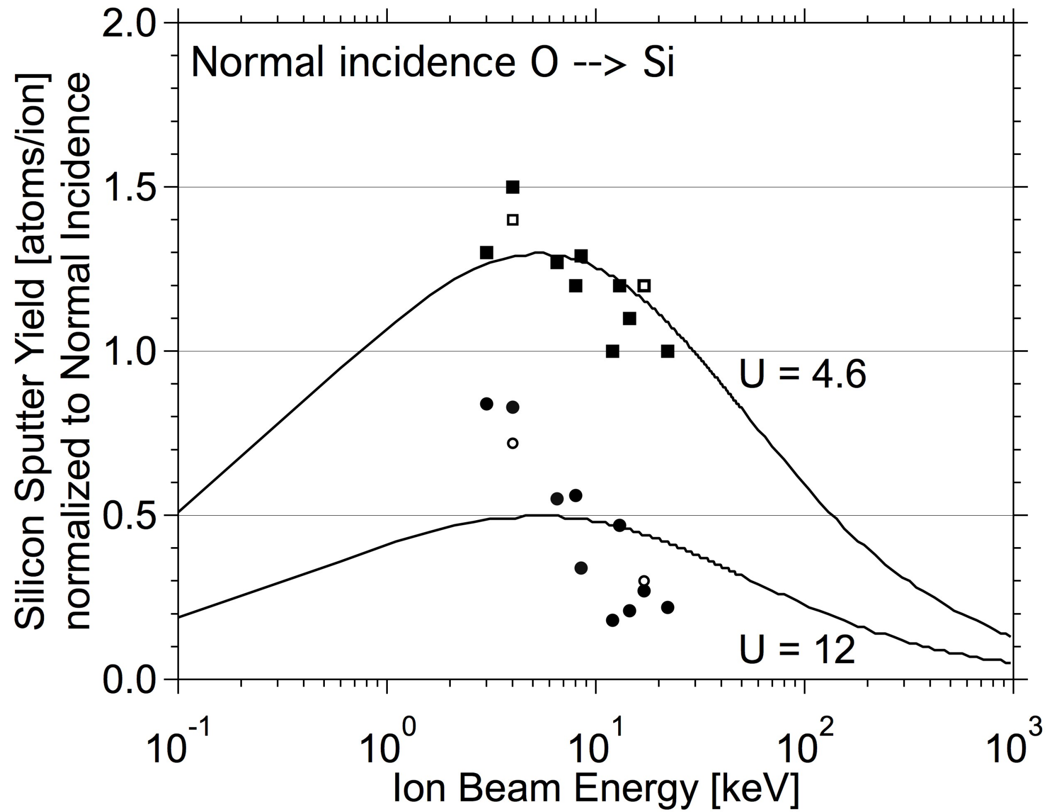

Figure 3.11. Normalized and clean silicon sputter yields calculated from measured silicon sputter yields for $O^{\pm}$ and $O_2^{\pm}$ primary ion beams vs. experimental impact energy. Circular data points are the silicon sputter yields of figure 3.9. Square data points are the corresponding clean sputter yields calculated from the normalized sputter yields. Open symbol data are taken from figure 4 of Franzreb 2004. The two curves are theoretical yields for oxygen primary ion beams at normal incidence sputtering silicon calculated using Sigmund's sputter yield theory. The upper curve is calculated using the cohesive energy of silicon, U = 4.6 eV/atom, and the lower using an arbitrarily larger binding energy of U = 12eV/atom.

Sigmund and many others used a value of 7.8eV/atom for the binding energy of silicon. This larger binding energy predicts lower silicon sputter yields which would provide better agreement with the lower sputter yields measured with noble gas ion beams with poorer vacuum. The cohesive energy of silicon is reported by Gschneidner (1964) to be 4.6eV/atom and is supported by theoretical calculations (Li 1991).

For metals the enthalpy of sublimation is used for the binding energy but for silicon and other non-metals the value is not as clear. The appropriate value may be the cohesive energy or some value derived from it taking into account the number of bonded atoms and the atoms' location at the surface. In the event that a different value of binding energy is found to be more appropriate, the calculations of clean silicon sputter yields from the atom fraction of silicon may require a proportionality constant different from 1. The proportionality constant may also be a function of the silicon atom fraction.

Sigmund's theory is often used in a semi-empirical manner and authors have modified it based on experimental results. Sigmund's general sputter yield equation converges to different solutions by the choice of an index variable. The value of the variable is chosen based on energy so that equations applicable for SIMS, RBS or neutron scattering may be derived. The variable is used in the derivation of the α function and the exponent f in the angular function for sputter yields for example. The α function is a function of energy despite the energy term not

appearing in it. The form of the function itself is energy dependent in its derivation. In practice, authors have adjusted the alpha function based on experimental evidence. Steinbrüchel (1985) for example has proposed one alpha function after observing that the silicon sputter yields predicted for 600eV Ne^+ using the alpha function of Sigmund and that of Andersen and Bay (Andersen 1975) differ by as much as 0.5 atoms/ion.

3.9 Clean Sputter Yields Applied to a Similar Study

For comparison, clean silicon sputter yields were calculated from silicon sputter yields reported in another study (Wittmaack 2000) using a different model of mass spectrometer. In this study silicon sputter yields were measured using both 5keV Ne^+ and 10keV O_2^+ primary ion beams. The 5keV neon beam was used to simulate the clean silicon sputter yields the 5keV per oxygen atom beam would theoretically produce. The theoretical sputter yields of isoenergetic neon and oxygen ion beams in figure 3.5 are similar due the small difference in atomic number and mass.

The experiments were conducted on an Atomika secondary ion mass spectrometer capable of changing the impact angle independently of impact energy. Wittmack found that for more oblique angles, the silicon sputter yields from an oxygen ion beam was approximately 90% of those produced by the neon ion beam of the same impact angle as expected due to low oxygenation of the sample surface. For more oblique impact angles, Wiitmaack found that the silicon sputter yields produced by an

oxygen ion beam were approximately 90% of those produced by the neon ion beam similar to the ratio of theoretical sputter yields in figure 3.5.

The silicon sputter yields from the oxygen ion beam are reproduced in figure 3.12. The circular data points are the silicon sputter yields at the experimental impact angle but normalized to 10keV per atom energy. The distribution of the normalized silicon sputter yields measured on the Atomica about the theoretical silicon sputter yield curve generated using a cohesive energy of 12eV per atom is similar to the results of figures 3.7 and 3.11 measured on the Cameca.

Wittmaack also considered clean sputter yields as the theoretical sputter yield if the surface remained free of oxygen, but his intentions were to develop a formula relating the clean and oxygenated silicon sputter yields (measured with neon and oxygen beams respectively) using the measured surface O/Si ratio. He relied on RBS and electron emission techniques for measurement of surface oxygen concentrations. These techniques measure an average bulk concentration with a maximum O/Si ratio of 2.

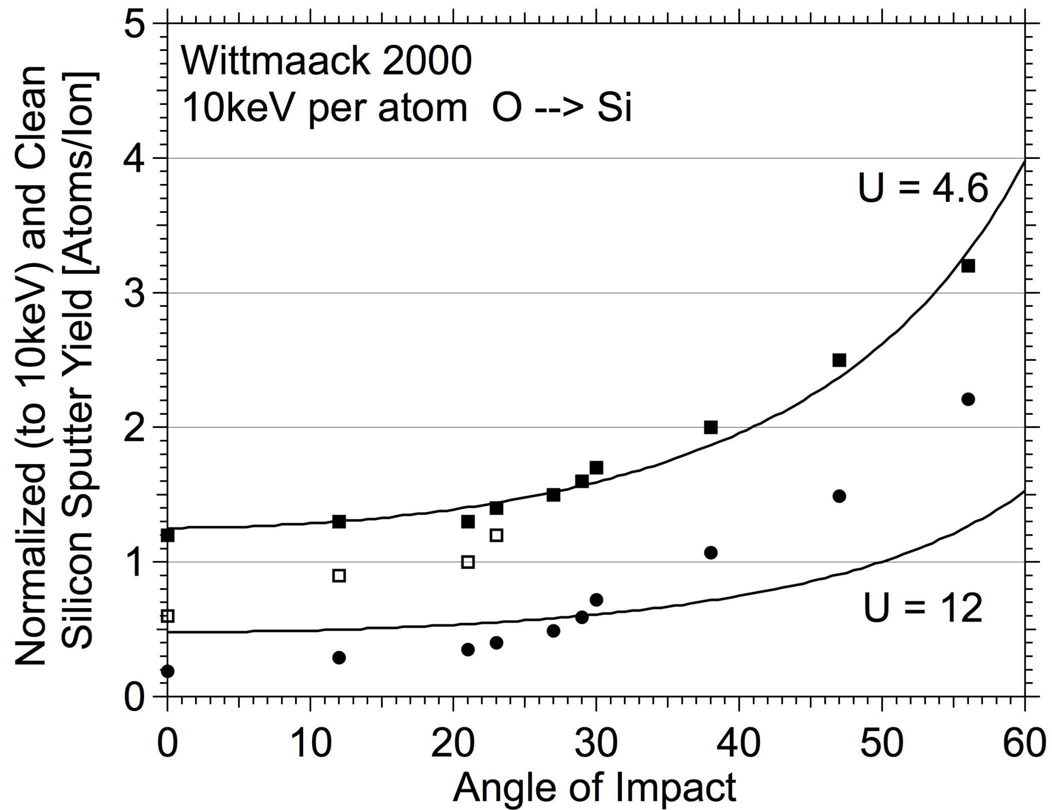

Figure 3.12. Normalized and clean silicon sputter yields for $O_2^{\pm}$ primary ion beams vs. the experimental impact angle using data from Wittmaack (2000). Experimental silicon sputter yields were normalized to 10keV impact energy per atom using Sigmund's sputter yield equations. The two curves are theoretical yields for 10keV monatomic oxygen primary ion beams sputtering silicon using Sigmund's sputter yield theory using the cohesive energy of silicon (U= 4.6 eV/atom) and an arbitrarily larger binding energy (U= 12 eV/atom) and adjusted for impact energy. The original sputter yields were measured using 10keV O_2^+ primary ions. The circular data points are the experiment yields if they had been collected with 20keV O_2^+ primary ions (10 keV/atom). The corresponding closed square symbols are the clean sputter yields calculated with an assumption that the surface O/Si ratio is inversely proportional to the sputter yield. The open square symbols are also clean sputter yields with a maximum O/Si ratio of 2.

The clean sputter yields have been calculated from the normalized silicon sputter yields and included as square data points in figure 3.12 as well. As the surface O/Si ratio is not determined for these data from an ^{18}O implant, the inverse of the silicon sputter yield was used here instead. The clean silicon sputter yields were calculated from the normalized silicon sputter yields and the O/Si ratios with no maximum O/Si ratio (closed square symbols) and with a maximum O/Si of 2 imposed (open square symbols). Clean silicon sputter yields calculated with no maximum O/Si ratio are in better agreement with Sigmund's theoretical curve.

3.10. Normalized Silicon Sputter Yields and the Silicon Atom Fraction

Another consideration of the oxygenation of the sample surface and its impact on the silicon sputter yield is found in figure 3.13 where the silicon sputter yield is plotted against the silicon atom fraction. The normalized silicon sputter yields in this figure have been adjusted to normal incidence and 10keV per atom impact energy. The black data points are normalized silicon sputter yields of oxygen ion beams of several different experimental impact angles and energies. It is not surprising that a linear trend is observed for the normalized silicon sputter yield with silicon atom fraction for primary oxygen ion beams as the silicon sputter yield is inversely proportional to the O/Si ratio.

Blue data points in figure 3.13 are normalized silicon sputter yields from oxygen ion beams with and without the addition of flood gas taken from Franzreb (2004). The surface O/Si ratios were measured in these experiments using the same ^{18}O implant in silicon. The O/Si ratio is not inversely proportional to the silicon sputter yield when oxygen is added to the sample surface using a flood gas but the normalized silicon sputter yields from oxygen ion beams with oxygen flood fit the same linear trend with silicon atom fraction.

The sputter yields of figure 3.14 have similarly been normalized for 10keV impact and normal incidence but with argon ion beams (Franzreb 2004). The oxygenation of the sample surface for these experiments is increased solely by addition of oxygen flood gas. As suggested in this reference, there is a linear trend over a narrow range of silicon atom fractions for the 8keV argon ion beam experiments as indicated by the line drawn through the data points. The silicon sputter yields measured with the two different ion beam energies do not converge into a single trend on normalization as was the case for oxygen ion beams with and without oxygen flood gas.

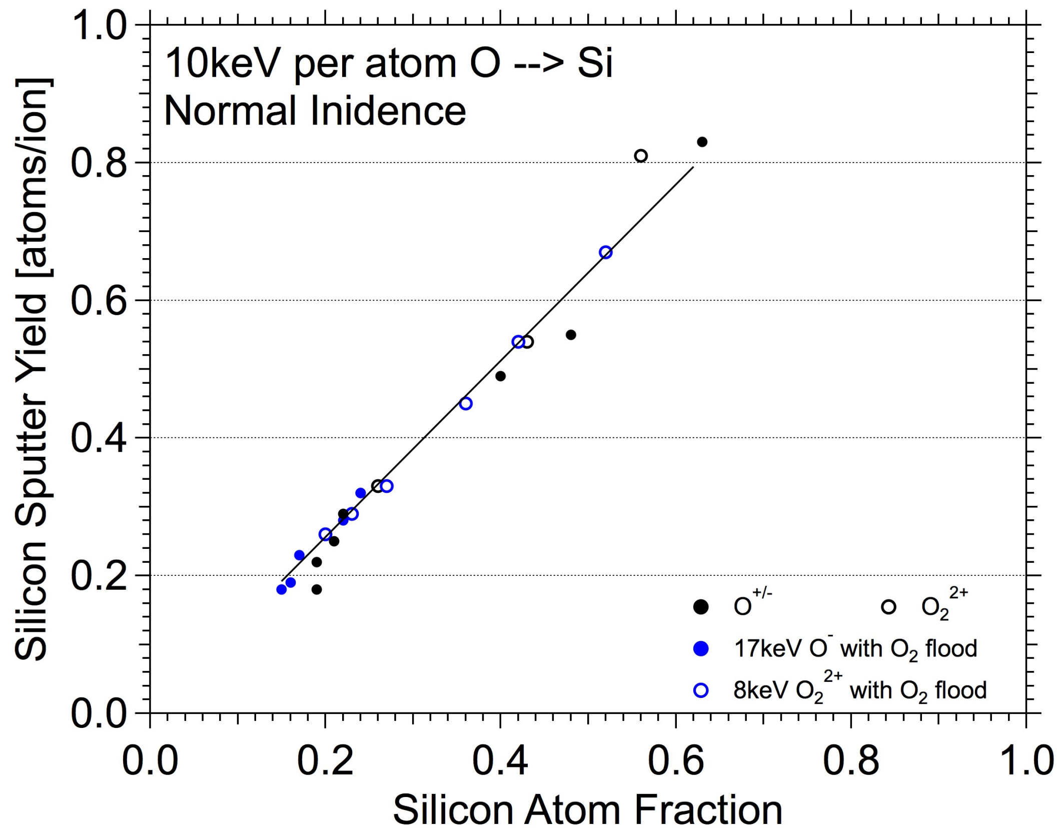

Figure 3.13. Normalized silicon sputter yields of silicon sputtered by oxygen ion beams plotted against measured silicon atom fractions at the sample surface. The sputter yields are normalized for 10keV impact energy and a normal incidence impact angle. Black data points are sputter yields for $O^{\pm}$ and O_2^+ ion beams with a range of experimental impact energies and angles. The blue data symbols are normalized silicon sputter yields calculated from data in Franzreb (2004) for silicon sputtered with a 17keV O^- ion beam (closed symbol) and with an 8keV O_2^+ ion beam (open symbol) with and without the addition of oxygen flood gas. All silicon atom fractions were determined from O/Si measurements using the ^{18}O implant sample.

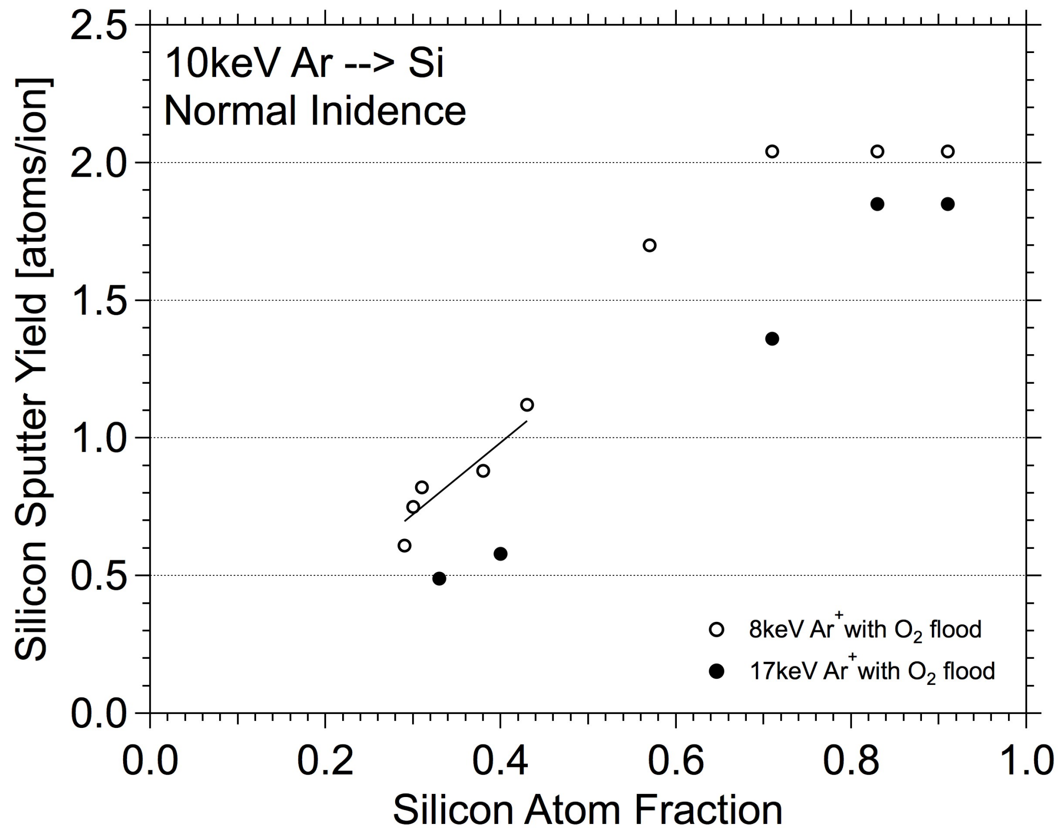

Figure 3.14. Normalized silicon sputter yields of silicon sputtered by argon ion beams plotted against measured silicon atom fractions at the sample surface calculated from data in Franzreb (2004). The sputter yields are normalized for 10keV impact energy and a normal incidence impact angle. Open symbol data points are normalized sputter yields for an 8keV Ar^+ primary ion beam and closed symbol data points are normalized sputter yields for an 17keV Ar^+ primary ion beam. All silicon atom fractions were determined from O/Si measurements using the ^{18}O implant sample. The addition of oxygen flood gas was used to increase the O/Si ratio.

3.11 Normalized and Clean Silicon Sputter Yields for Argon Sputtered Silicon with Oxygen Flood Gas.

The clean silicon sputter yields of experiments made with an oxygen flood gas are also considered using the data of Franzreb (2004). Figures 3.15 and 3.16 are normalized and clean silicon sputter yields plotted against experimental angle and energy respectively for argon sputtered silicon with an oxygen flood gas. Figures 3.17 and 3.18 are similar plots of normalized and clean silicon sputter yields against experimental impact angle and energy for silicon sputtered with oxygen ion beams with the addition of oxygen flood gas. Yields plotted against experimental angle have been normalized to 10keV per atom and yields plotted against energy have been normalized to normal incidence.

Full symbol data points in figures 3.15 to 3.18 are silicon sputter yields normalized to 10keV or normal incidence. The multiple sputter yields for each primary ion beam are due to the different oxygen gas pressures in the sample chamber for each experiment with a particular argon ion beam. The average clean sputter yield calculated for each primary ion beam is shown as an open data point with the standard deviation included as the error bar.

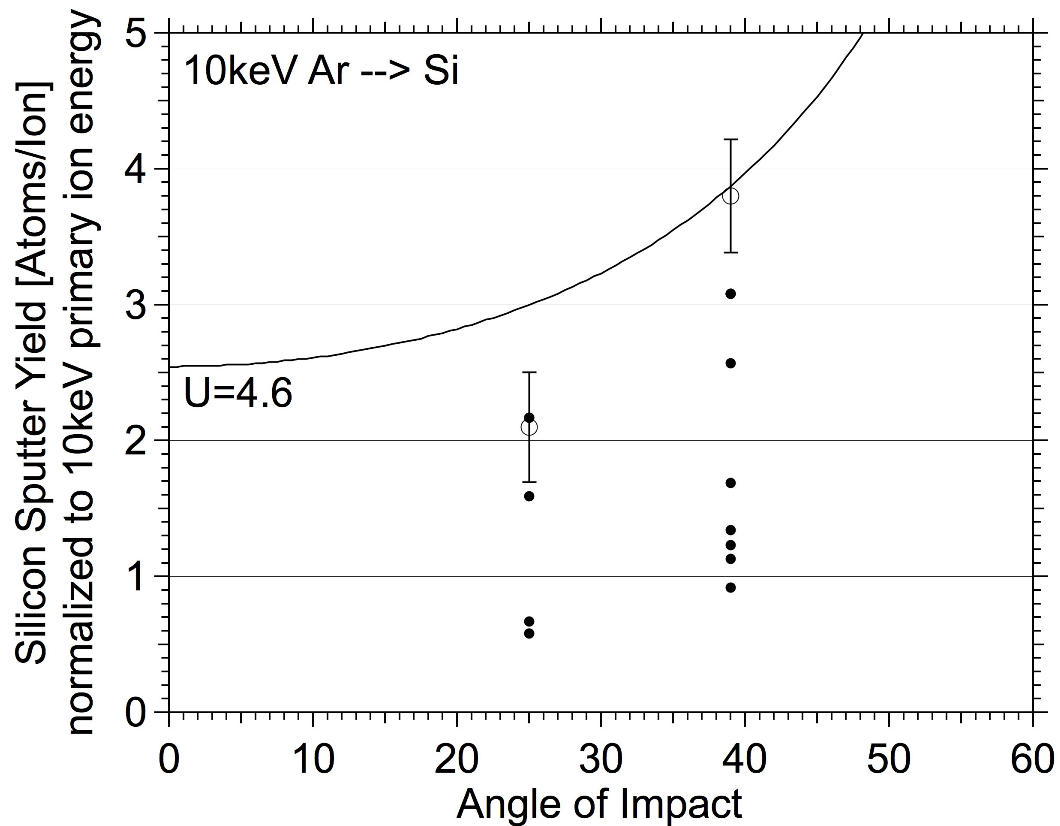

Figure 3.15. Normalized and clean silicon sputter yields for argon ion beams calculated from data in Franzreb (2004) plotted against the experimental impact angle. Closed symbol data points are the experimental sputter yields normalized to 10keV impact energy. The multiple normalized sputter yields at each impact angle are due to experiments conducted with different oxygen flood gas pressures in the sample chamber. Clean sputter yields are calculated from each normalized sputter yield. The average clean sputter yield at each impact angle is shown as an open symbol data point. The error bar is the calculated standard deviation. The curve is the theoretical silicon yield vs. impact angle for argon primary ion beams at 10keV impact energy using Sigmund's sputter yield theory. The 4.6eV/atom cohesive energy of silicon has been used.

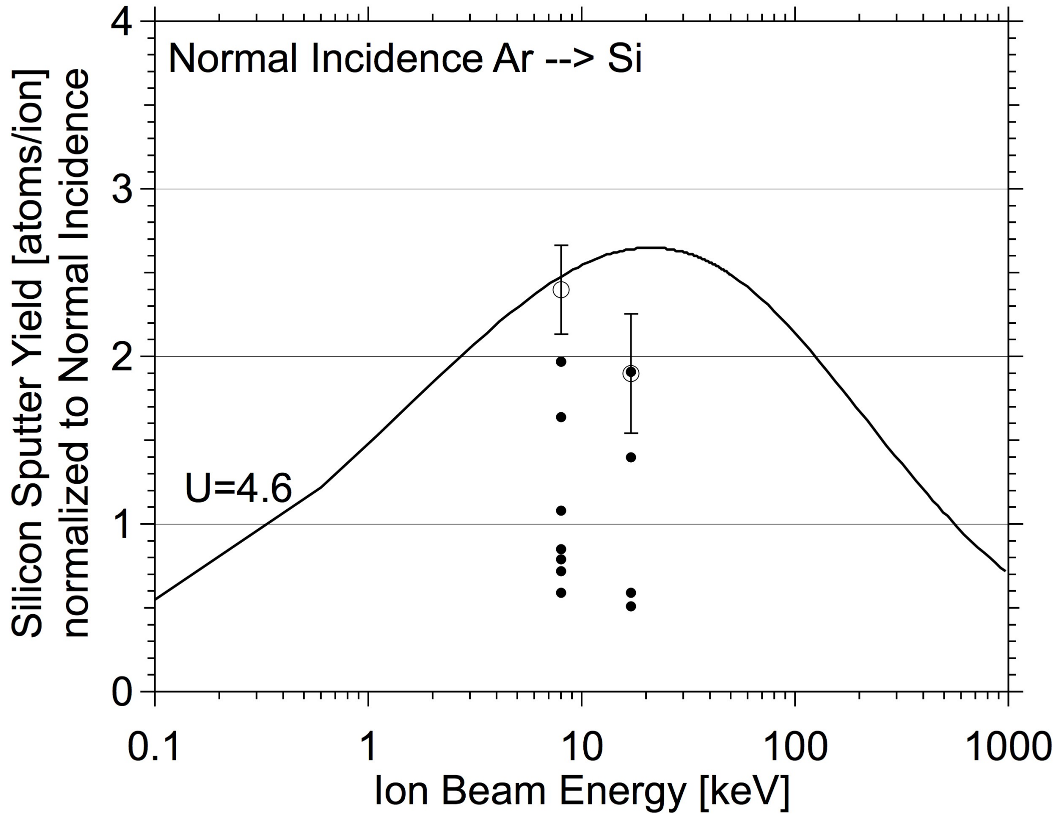

Figure 3.16. Normalized and clean silicon sputter yields for argon ion beams calculated from data in Franzreb (2004) plotted against the experimental impact energy. Closed symbol data points are the experimental sputter yields normalized to normal incidence impact angle. Many normalized sputter yields are present with the same impact energy due to experiments conducted with different oxygen flood gas pressures in the sample chamber. Clean sputter yields are calculated from each normalized sputter yield. The average clean sputter yield at each impact angle is shown as an open symbol data point. The error bar is the calculated standard deviation. The curve is the theoretical silicon yield vs. impact angle for argon primary ion beams at normal incidence using Sigmund's angular sputter yield equation. The 4.6eV/atom cohesive energy of silicon has been used.

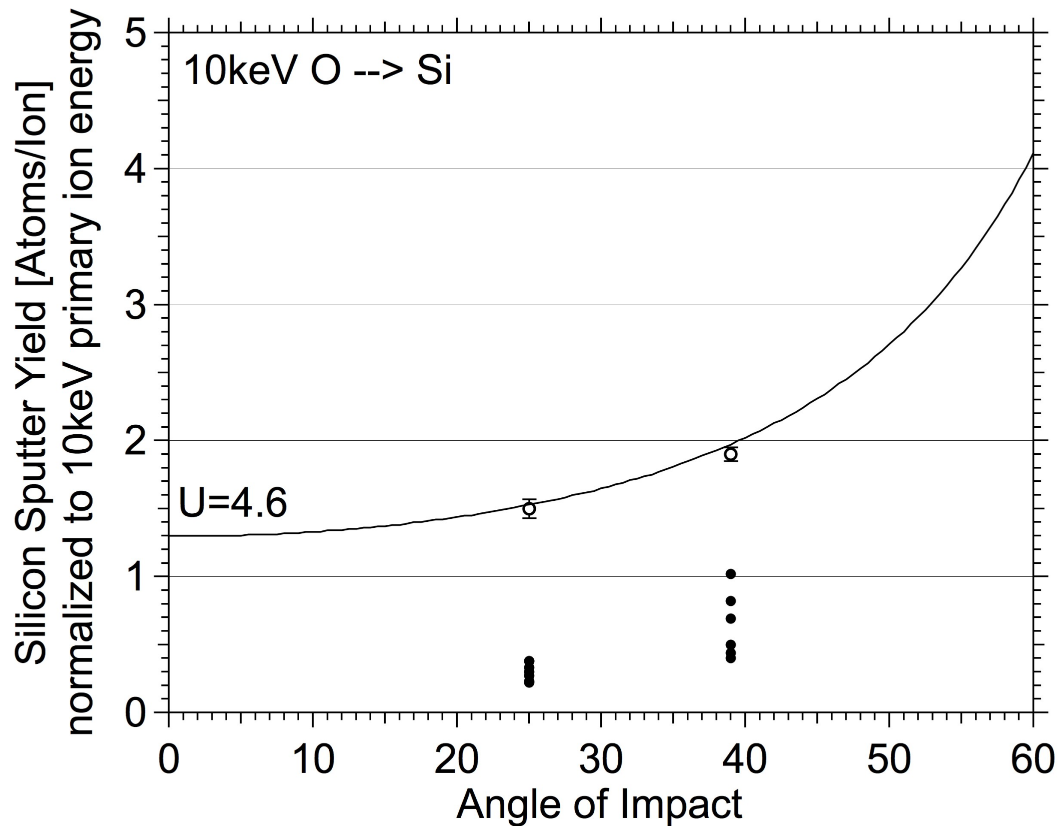

Figure 3.17. Normalized and clean silicon sputter yields for oxygen ion beams calculated from data in Franzreb (2004) plotted against the experimental impact angle. Closed symbol data points are the experimental sputter yields normalized to 10keV impact energy. The multiple normalized sputter yields at each impact angle are due to experiments conducted with different oxygen flood gas pressures in the sample chamber. Clean sputter yields are calculated from each normalized sputter yield. The average clean sputter yield at each impact angle is shown as an open symbol data point. The error bar is the calculated standard deviation. The curve is the theoretical silicon yield vs. impact angle for argon primary ion beams at 10keV impact energy using Sigmund's sputter yield theory. The 4.6eV/atom cohesive energy of silicon has been used.

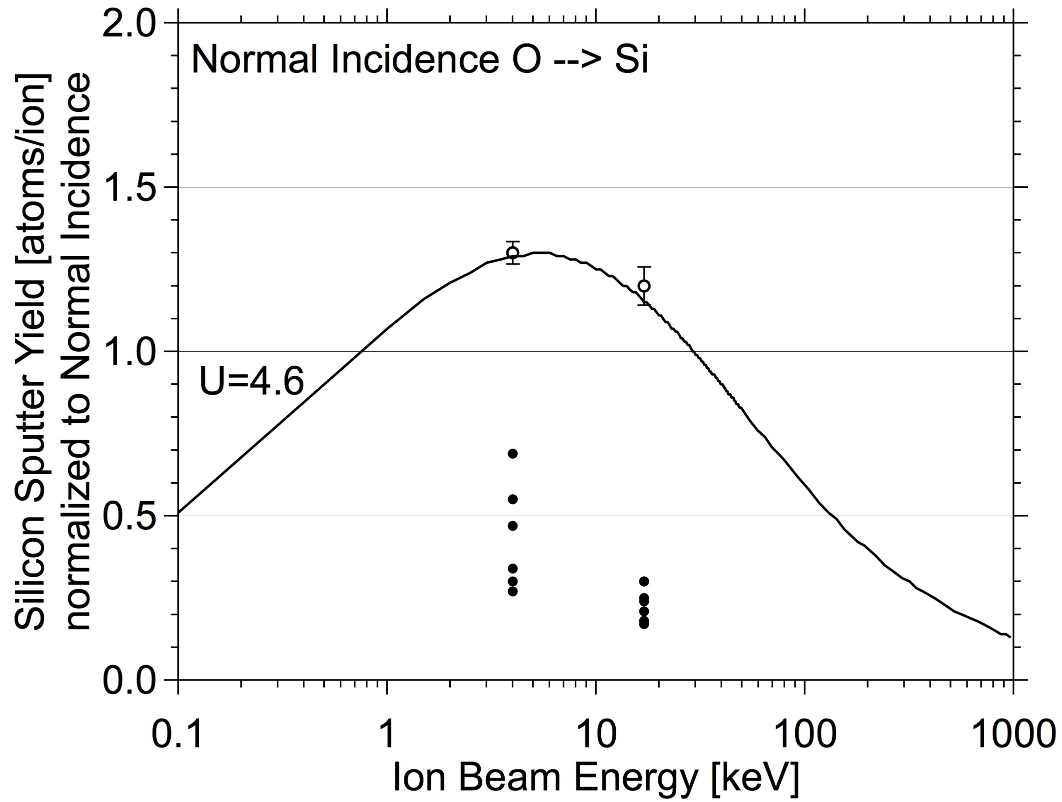

Figure 3.18. Normalized and clean silicon sputter yields for oxygen ion beams calculated from data in Franzreb (2004) plotted against the experimental impact energy. Closed symbol data points are the experimental sputter yields normalized to normal incidence impact angle. Many normalized sputter yields are present with the same impact energy due to experiments conducted with different oxygen flood gas pressures in the sample chamber. Clean sputter yields are calculated from each normalized sputter yield. The average clean sputter yield at each impact angle is shown as an open symbol data point. The error bar is the calculated standard deviation. The curve is the theoretical silicon yield vs. impact angle for argon primary ion beams at normal incidence using Sigmund's angular sputter yield equation. The 4.6eV/atom cohesive energy of silicon has been used.

It would appear that the distribution of oxygen in the atom layers below the surface layer could be significant in producing the measured silicon sputter yield. The oxygen concentration gradient from the sample surface is steeper when oxygen is introduced as a flood gas with an argon ion beam. The good agreement of clean silicon sputter yields for oxygen ion beams with the theoretical silicon sputter yields predicted using Sigmund's theory and a binding energy of 4.6eV/atom is not lost with the addition of oxygen flood gas. Addition of oxygen flood gas does not increase the oxygen concentration gradient from the sample surface as much when an oxygen ion beam is used.

The binding energy at the sample surface may be a function of the distribution of the oxygen over several layers from the surface. The simple approach of calculating clean silicon sputter yields using a single proportionality constant of one may produce a good fit to theoretical silicon sputter yields for oxygen primary ion beams but perhaps a different proportionality constant is required for argon ion beams with oxygen flooding. More experimental data for argon primary ion beams of different impact energies and angles are needed.

3.12 Useful ion yields

The useful ion yields of several elements were measured in the same SIMS depth profiles used for measurement of O/Si ratios and silicon sputter yields. The ion yield of element X is the fraction of sputtered atoms of that element as monatomic ions:

$$Y(X^{+/-}) = \frac{n_{X^{+/-}} \text{ sputtered}}{n_X \text{ sputtered}}$$

The ion yield is also a function of the ion energy. The actual ion yield is difficult to measure, as some ions do not reach the detector due to scattering. The transmission of the instrument, T, is the fraction of ions that are detected and depends in part on the energy profile of the ion. The useful ion yield of an element X, $UY(X^{\pm})$ is the product of the ion yield and the instrument transmission. The useful ion yield is calculated from the ratio of the number of ions detected to the number of atoms sputtered:

$$UY(X^{+/-}) = \frac{n_{X^{+/-}} \text{ detected}}{n_X \text{ sputtered}}$$

For the sample matrix element, silicon, the total number of secondary silicon ions detected is determined from the total sputter time of the SIMS depth profile and the average, steady state, silicon ion intensity (ions/s). The detectable secondary ions originate in a cylinder defined by the crater depth, D, and the area, A, of the field aperture used to avoid crater edge effects, and the total number of silicon atoms sputtered from this volume is found using the silicon atom density, ρ. The useful silicon ion yield is

calculated from the ratio of the number of secondary silicon ions detected to the number of silicon atoms sputtered over the entire depth profile:

$$UY(Si^{+})=\frac{I(Si^{+})_{ave}\bullet \text{sputter time}}{D_{crater}\bullet A_{aperture}\bullet \rho_{Si}}$$

A total of $8.2\text{x}10^{13}$ silicon atoms were sputtered from within the area defined by the 63µm field aperture during the 5097s during which the depth profile of figures 3.1 and 3.2 were acquired. After adjustment for the isotopic abundance of silicon, the useful ion yield of silicon was found to be $7.6\text{x}10^{-3}$ ions/atom for this depth profile.

The useful ion yields of other elements, implanted into the silicon sample, were measured relative to silicon. The relative useful ion yields are proportional to the ratio of measured secondary ion intensities (with equal counting times) to the atom densities of each element. The measurements are made at the peak of the implant profiles where the atom densities of the implanted implants have been determined (table 3.1):

$$UY(X^{+})=\left(\frac{I\,(X^{+})_{peak}}{n_{X,\,peak}}\right)\left(\frac{n_{Si}}{I\,(Si^{+})_{ave}}\right)UY(Si^{+})$$

The average measured useful positive ion yields sputtered from silicon using primary oxygen ion beams for several elements are plotted against the O/Si ratio in the log-log plots of figures 3.19 and 3.20. Two figures have been used to present the results in order to avoid clutter. The useful ion yield of cesium is high and constant for all surface O/Si

ratios due to its low ionization potential. An estimation of the transmission efficiency of the Cameca IMS-3f may be made from the useful ion yield of cesium assuming 100% ionization but the transmission depends on the shape of the energy distribution also. Cesium has a narrow energy distribution so the 40-50% transmission efficiency of cesium may not apply to other elements. For elements with larger ionization potential, the useful ion yields are less and also increase with oxygenation of the sample surface up to O/Si of 2.

The useful ion yields of silicon, boron, aluminum and oxygen are again considered in figures 3.21 through 3.24 with inclusion of useful ion yields produced using argon primary ion beam with oxygen flood gas in the sample chamber during the SIMS depth profile experiments as open symbol data points (Franzreb 2004). The method of introduction of oxygen to the sample surface does not appear to be a significant factor in the measured ion yields as similar trends are observed with O/Si produced by both oxygen ion beams and argon ion beams with oxygen flood gas. The lower O/Si ratios produced with the argon ion beam reveal the continued decrease in useful ion yield down to approximately an O/Si ratio of 0.1. The useful ion yields are fairly constant for very low O/Si.

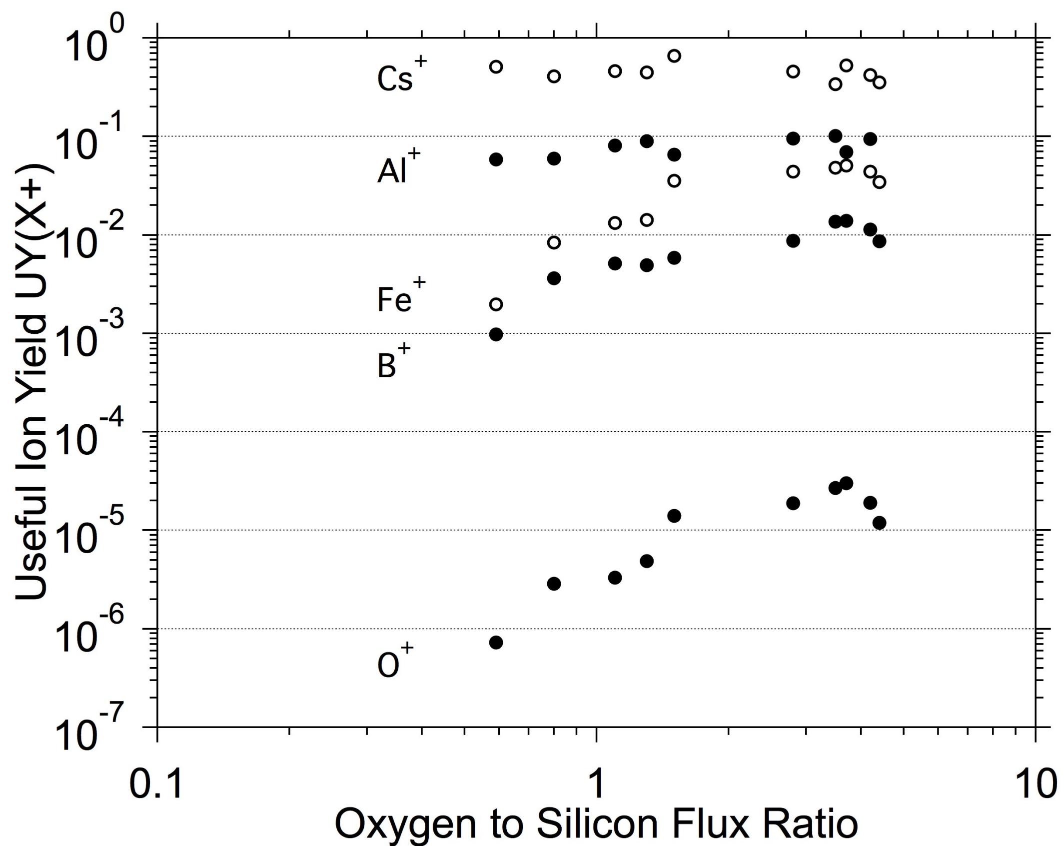

Figure 3.19. A log-log plot of measured useful ion yields for several elements sputtered from a silicon sample with both monatomic and diatomic primary oxygen ion beams. The useful ion yields are plotted against the measured oxygen to silicon ratio. Two figures are used for clarity. Both contain cesium and oxygen useful ion yield data for comparison. Some of the data here was previously reported (Sobers 2004).

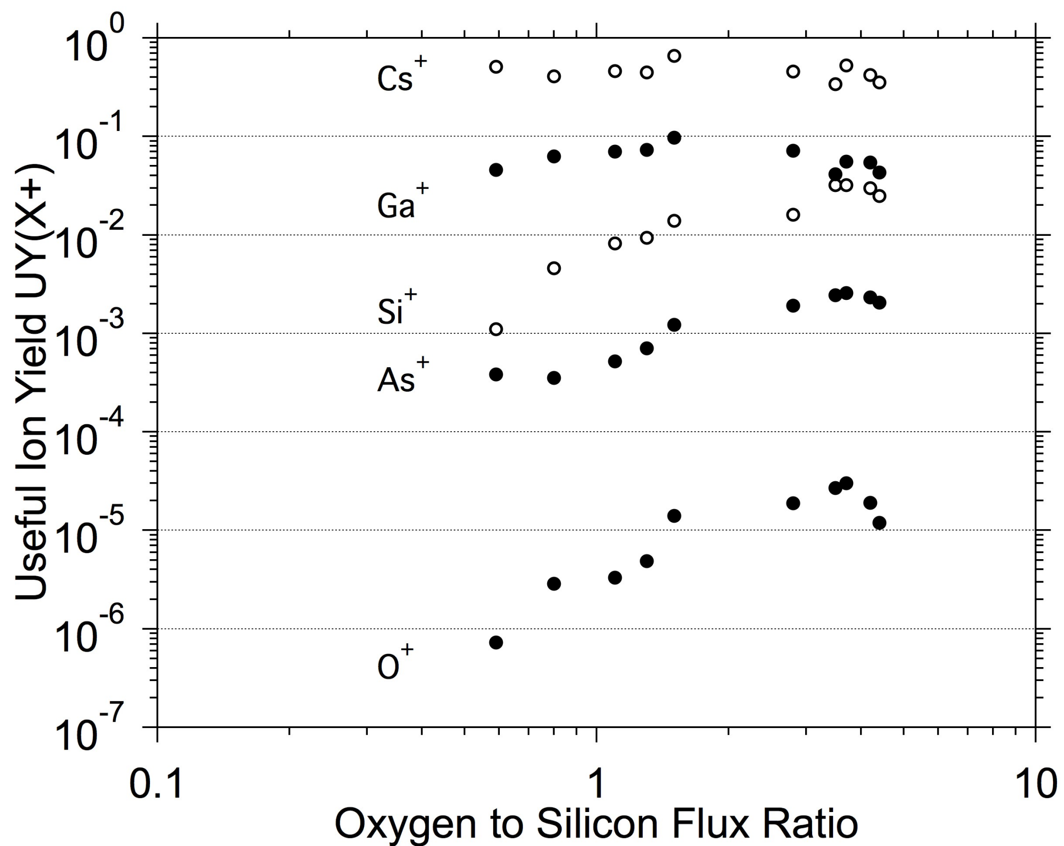

Figure 3.20. A continuation of figure 3.19. A log-log plot of measured useful ion yields for several elements sputtered from a silicon sample with both monatomic and diatomic primary oxygen ion beams. The useful ion yields are plotted against the measured oxygen to silicon ratio. Two figures are used for clarity. Both contain cesium and oxygen useful ion yield data for comparison. Some of the data here was previously reported (Sobers 2004).

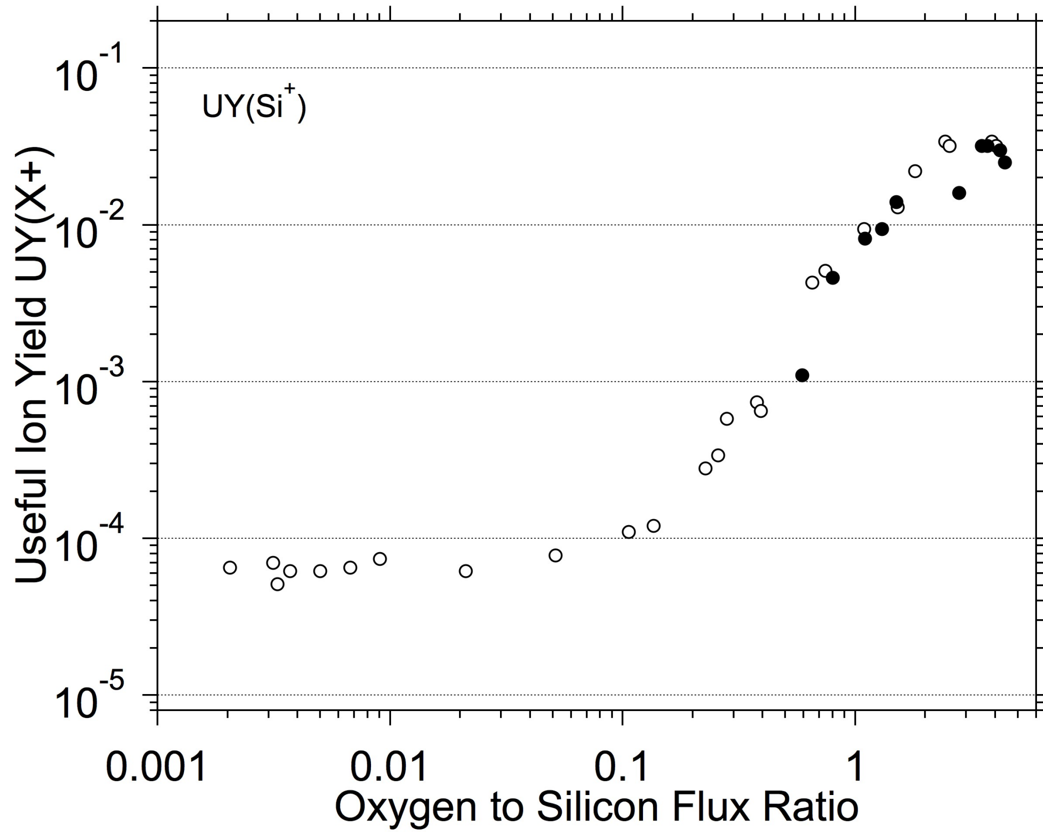

Figure 3.21. Useful ion yields of silicon from sputtered silicon plotted against surface O/Si ratios. Full symbol data is from the sputtering of silicon with oxygen primary ion beams and is the same as that in figure 3.20. Open symbol data (Franzreb 2004) is for silicon sputtered with argon primary ion beams using oxygen flood gas in the sample chamber during the experiment.

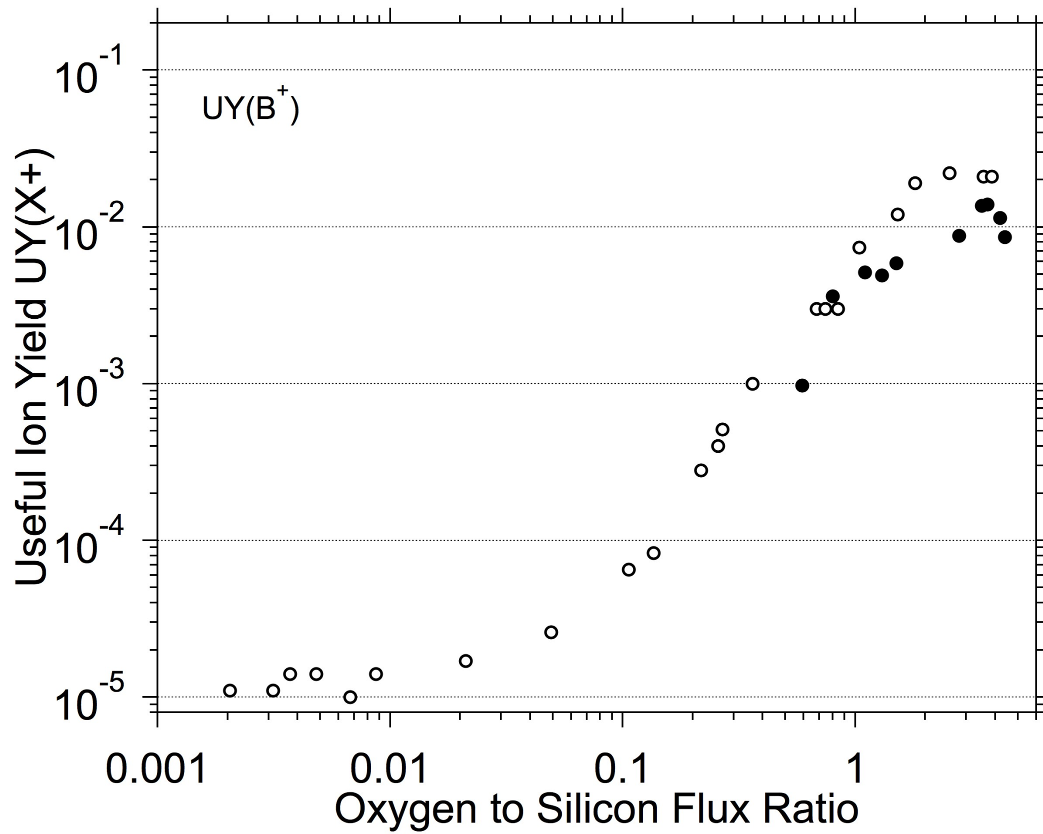

Figure 3.22. Useful ion yields of sputtered boron implanted in silicon plotted against surface O/Si ratios. Full symbol data is from the sputtering of silicon with oxygen primary ion beams and is the same as that in figure 3.19. Open symbol data (Franzreb 2004) is for silicon sputtered with argon primary ion beams using oxygen flood gas in the sample chamber during the experiment.

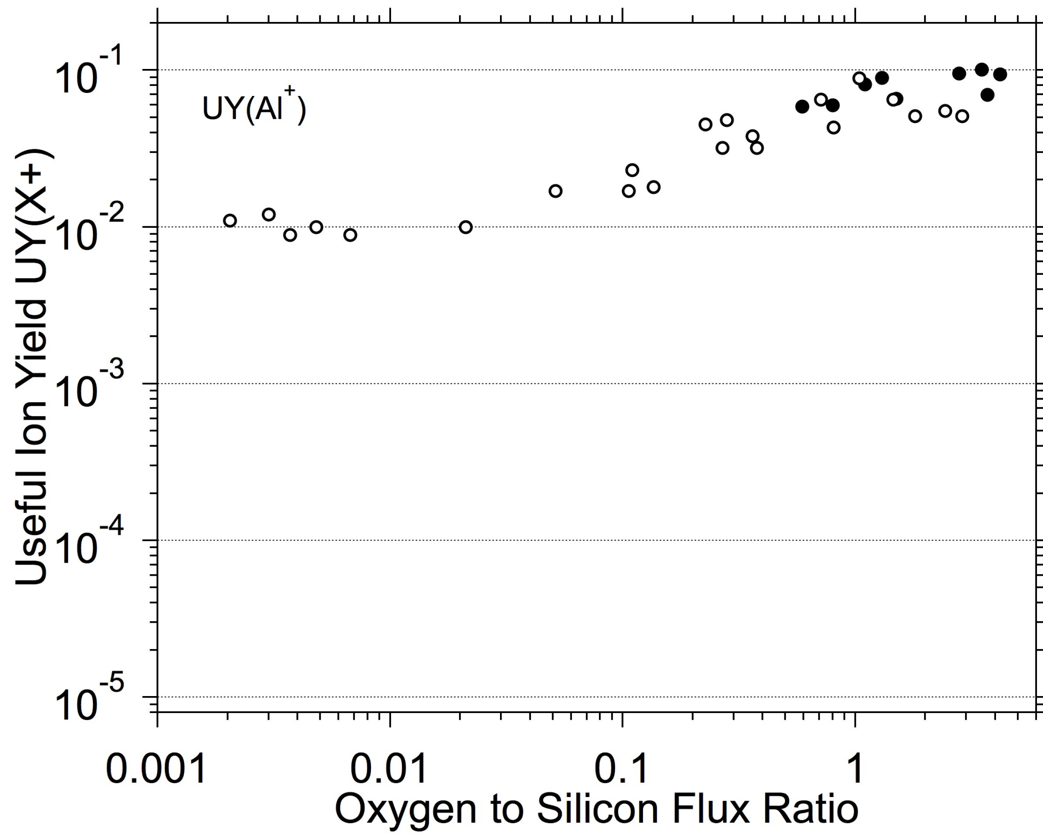

Figure 3.23. Useful ion yields of sputtered aluminum implanted in silicon plotted against surface O/Si ratios. Full symbol data is from the sputtering of silicon with oxygen primary ion beams and is the same as that in figure 3.19. Open symbol data (Franzreb 2004) is for silicon sputtered with argon primary ion beams using oxygen flood gas in the sample chamber during the experiment.

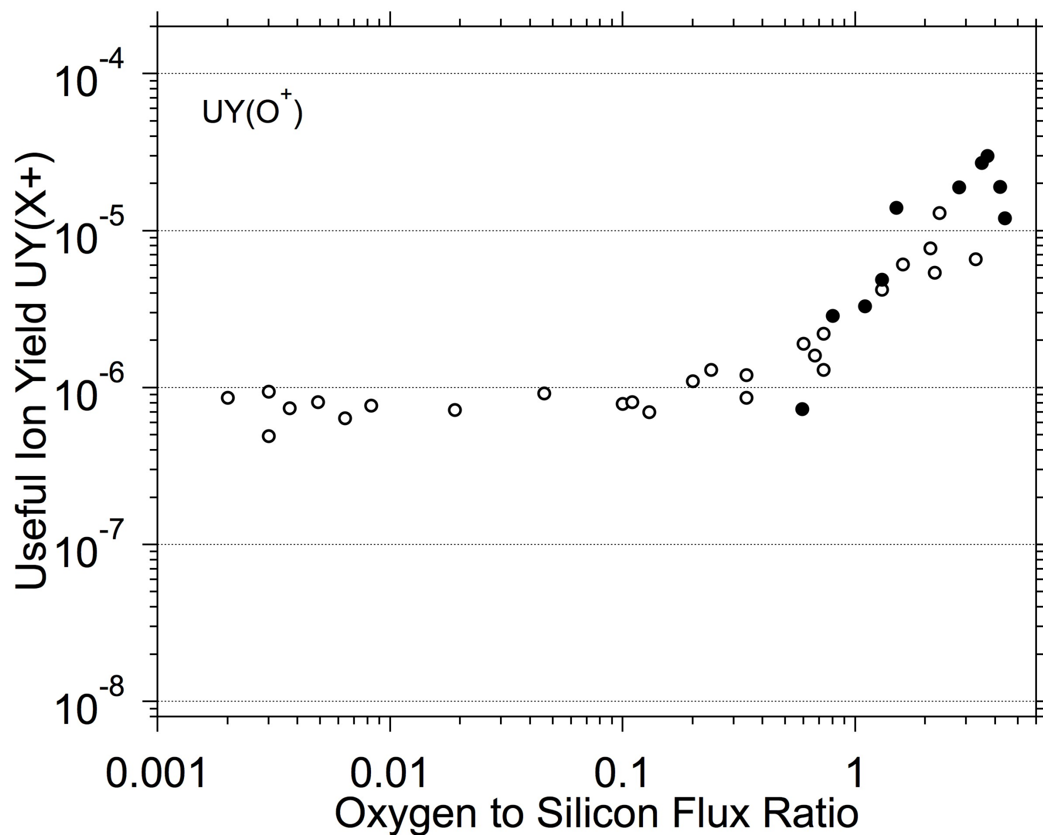

Figure 3.24. Useful ion yields of sputtered oxygen implanted in silicon plotted against surface O/Si ratios. Full symbol data is from the sputtering of silicon with oxygen primary ion beams and is the same as that in figures 3.19 and 3.20. Open symbol data (Franzreb 2004) is for silicon sputtered with argon primary ion beams using oxygen flood gas in the sample chamber during the experiment.

The decrease in useful ion yield of the elements from the maximum value in figures 3.19 through 3.24 is dependent on the ionization potential. The useful ion yield of aluminum at very low O/Si is only an order of magnitude less than under highly oxygenated conditions. The useful ion yield of boron drops three orders of magnitude. The decrease in useful ion yield is not as large as expected given its large ionization potential. At this low surface oxygen concentration, the mechanism of formation of the secondary ions is an Auger electron emission several angstroms from the sample surface. Electron stimulated desorption, ESD, of oxygen by sputtered electrons striking the sample surface may be an extra ionization mechanism for oxygen. Oxygen has been shown to undergo ionization from electron stimulated desorption in SIMS as well (Kilner 1984).

Andersen and Hinthorne (Andersen 1972) demonstrated an exponential dependence of useful positive ion yields of elements when measured against their respective ionization potentials:

$$UY(X^{+}) \propto e^{-IP}$$

A similar trend in useful negative ion yields with electron affinity was also observed. To demonstrate the exponential trend in useful positive ion yields with ionization potential, all elements must be sputtered from the same sample material. The dependence of the useful ion yield (positive or negative) of an element on the sample matrix is referred to as the SIMS matrix effect.

A matrix independent trend in useful ion yield with linear sputter yield (sputter rate) has been shown (Deline 1978a,b, Williams 1980). This trend requires comparison of useful ion yields obtained from different sample matrices using the same primary ion beam current density. The observation is interesting because it is independent of the sample matrix but the sputter yield is a more practical means of comparing useful ion yields.

Figure 3.25 is a semi-log plot of the average measured useful positive ion yields of elements sputtered from the silicon sample with a 3keV O^+ primary oxygen ion beam plotted against the respective ionization potentials of each element. The exponential dependence of the positive ion yield on the ionization potential is seen in the linear fit to the semi-log plot of the data. The useful positive ion yield of the matrix element, silicon, is part of this linear trend.

Both the sample matrix and the primary ion beam used to sputter the sample contribute to the SIMS matrix effect. The role of the primary ion beam in producing the SIMS matrix effect is observed in the slope of the trend in useful positive ions with ionization potential. The average measured useful ion yields produced by a 14.5keV O^- primary ion beam are shown in figure 3.26. The slope of the linear trend in useful ion yields with ionization potential is steeper for the less oxygenated surface produced by the 3keV O^+ primary ion beam in figure 3.25. Table 3.3 provides the slopes of useful ion yields with O/Si for each primary ion

beam considered in this study. For primary ion beams producing sub-oxides of silicon, the slope increases with increasing O/Si.

The useful ion yields for argon ion beams with O/Si less than 0.01 for B, Si, Al, and O from figures 3.21 to 3.24 are plotted against the ionization potentials of the elements in figure 3.27. Also included is the average cesium useful ion yield from the oxygen ion beam experiments as an open symbol data point. A linear trend is observed for all but oxygen (red symbol). The slope of the trend is -1.0 with oxygen excluded.

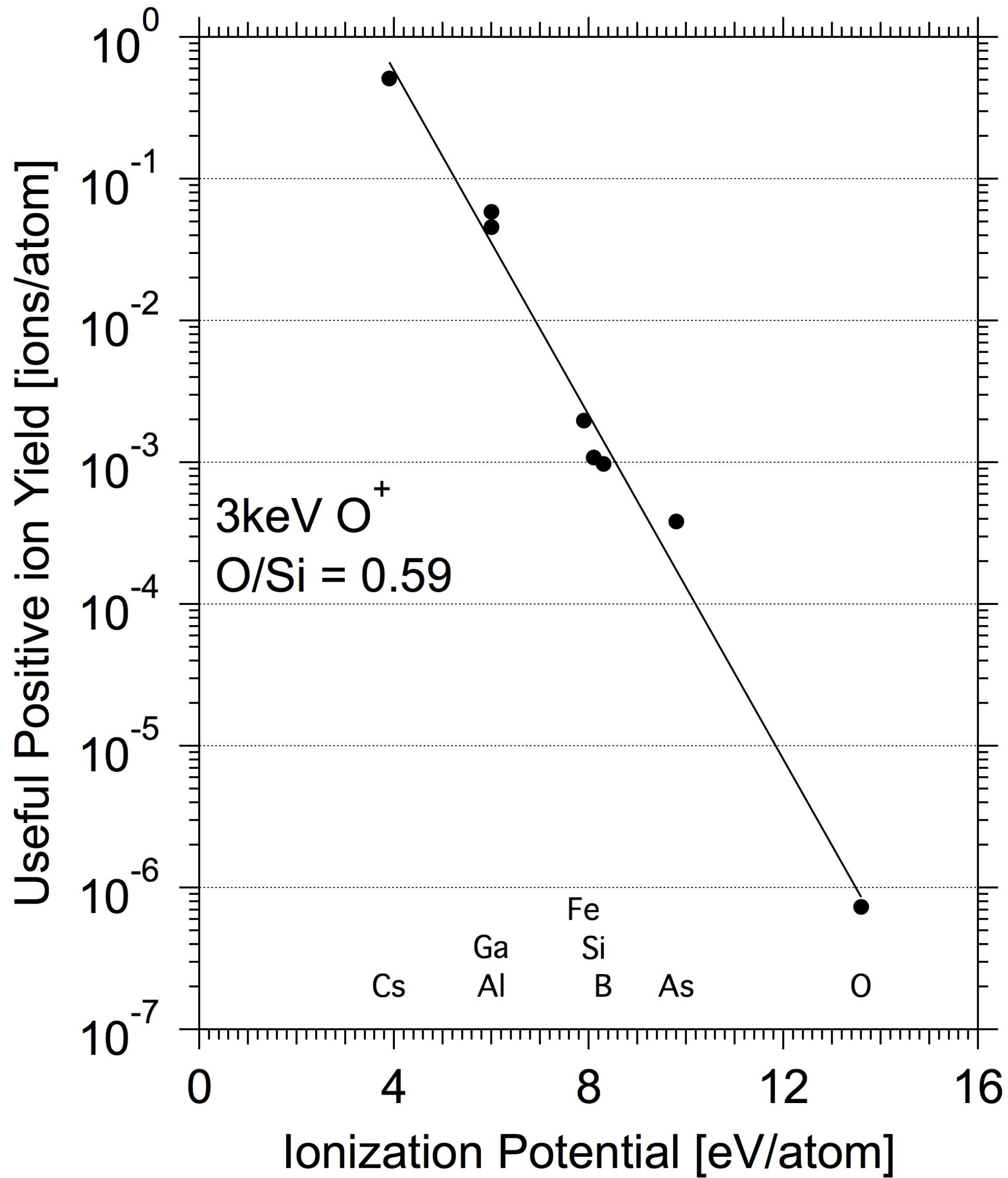

Figure 3.25. Average measured useful positive ion yields plotted against the ionization potential of each element. These ion yields were measured when the silicon implant sample was sputtered with a 3keV O^+ primary ion beam producing an average measured O/Si ratio of 0.59. The slope of the linear trend in this semi-log plot is -0.61.

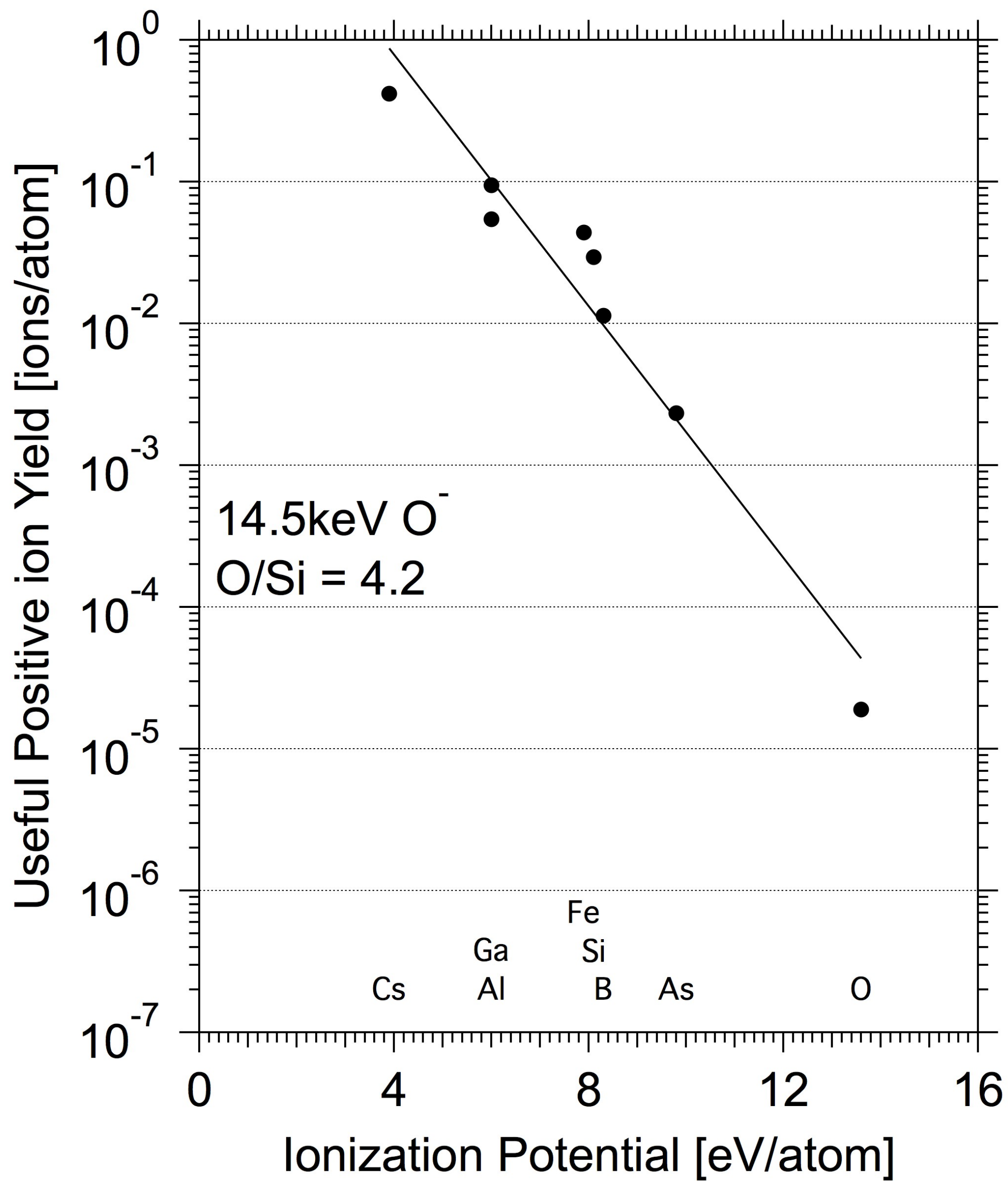

Figure 3.26. Average measured useful positive ion yields plotted against the ionization potential of each element. These ion yields were measured when the silicon implant sample was sputtered with a 14.5keV O^- primary ion beam producing an average measured O/Si ratio of 4.2. The slope of the linear trend in this semi-log plot is -0.44.

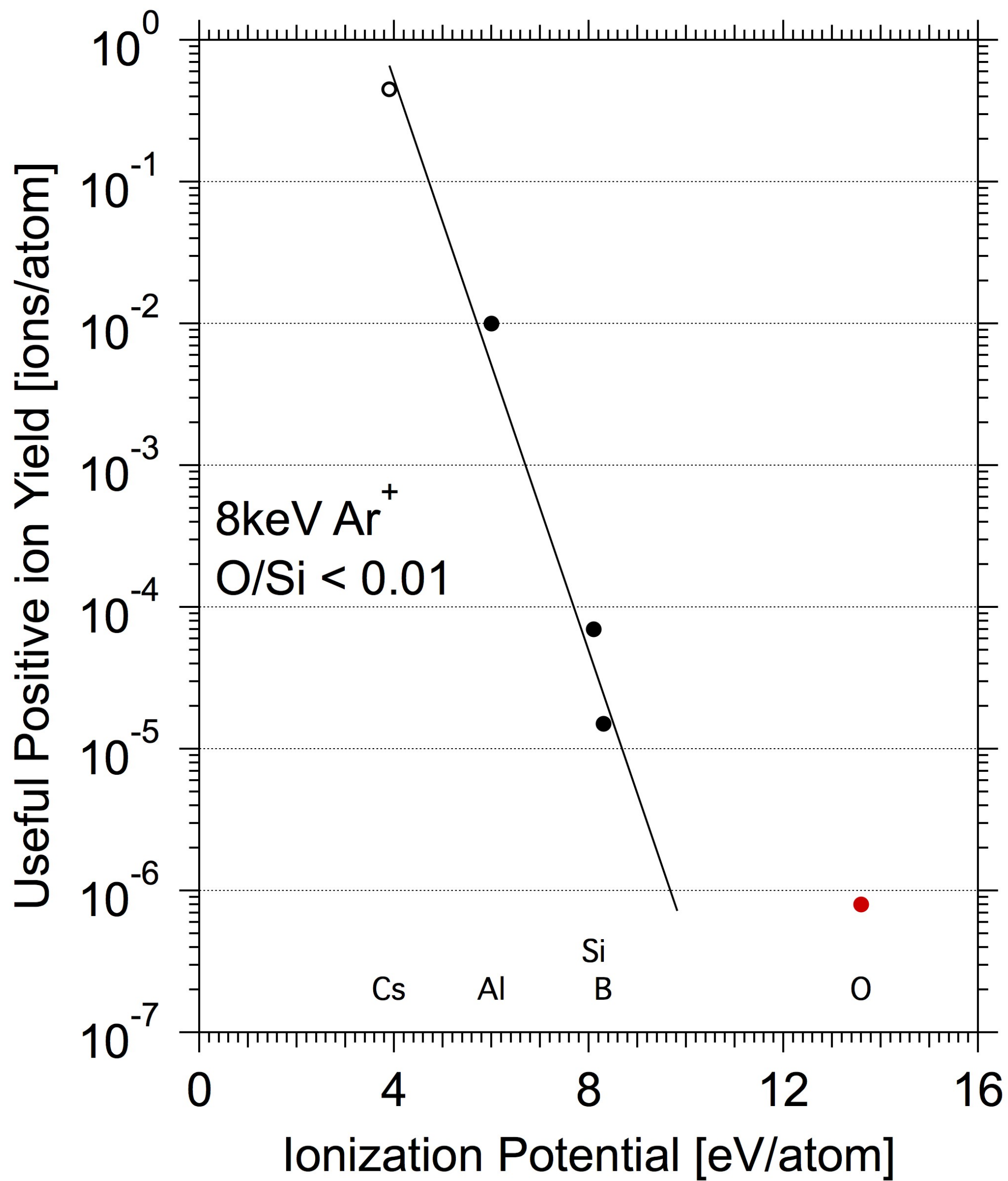

Figure 3.27. Average measured useful positive ion yields plotted against the ionization potential of each element. The useful ion yields of B, Al, Si and O were measured when the silicon implant sample was sputtered with a argon primary ion beams with no addition of oxygen flood gas. This data is taken from Franzreb (2004) and is also found in figures 3.21 to 3.24. The average useful ion yield of cesium (open symbol) of all oxygen ion beam data in figures 3.19 and 3.20. The slope of the linear trend in this semi-log plot is calculated from the data for Si, Al, B and Cs to be -1.0. The useful ion yield of oxygen (red) is not used in the slope calculation.

Beam	Impact Angle	O/Si	1/Y	Slope of log(UY) vs. IP
3.0 keV O^+	52°	0.59	0.53	-0.61
8.0 keV O_2^+	39°	0.80	0.77	-0.55
8.0 keV O^+	39°	1.1	1.2	-0.54
13.0 keV O_2^+	33°	1.3	1.3	-0.52
13.0 keV O^+	33°	1.5	1.5	-0.48
17.0 keV O_2^-	25°	2.8	2.5	-0.45
17.0 keV O^-	25°	3.5	3.2	-0.40
22.0 keV O^-	26°	3.7	3.8	-0.43
14.5 keV O^-	24°	4.2	4.0	-0.44
12.0 keV O^-	23°	4.4	4.9	-0.45
Argon		<0.01		-1.0

Table 3.3. The slope of the useful ion yields of several elements sputtered from silicon with primary oxygen ion beams when the log of the UY(X^+) is plotted against the ionization potential of element X (or the slope of the UY(X^+) vs. IP of element X plotted on a semi-log plot.). The slope of the useful ion yield vs. ionization potential for an argon ion beam is also included.

3.13 Summary

An ^{18}O implant in silicon has been used to measure the concentration of oxygen at the sputtered surface of silicon for oxygen ion beams of different impact energies and angles. Silicon sputter yields for oxygen ion beams are reduced by dilution of silicon at the sample surface except for oblique angles at which the surface O/Si ratio is low. Theoretical clean silicon sputter yields have been calculated from measured silicon sputter yields (normalized for angle or energy) and the atom fraction of silicon at the sample surface. The calculated clean sputter yields of silicon sputtered with oxygen ion beams are in good agreement with theoretical values predicted by Sigmund's sputter theory using a surface binding energy of 4.6eV/atom. Good agreement is also observed when oxygen flood gas is used for silicon sputtered with an oxygen ion beam but not an argon ion beam. This suggests that the sputter yield is dependent not only on the oxygen concentration of the surface layer, but also the oxygen concentration gradient from the sample surface.

Useful ion yields have been measured simultaneously with the surface O/Si in SIMS depth profiles of silicon with oxygen ion beams. Useful ion yields of secondary ions sputtered by oxygen ion beams are in good agreement with those of secondary ions sputtered with argon ions beams with the addition of oxygen flood gas. The useful ion yield of the elements studied appears to be dependent only on the oxygen

concentration of the surface layer and not on the oxygen gradient. Linear trends in semi-log plots of useful ion yield with ionization potential are observed for all oxygen ion beams. The slope of the trend decreases with oxygenation of the sample surface for suboxides due to greater increases in useful ion yield for elements of low ionization potential.

3.14 References

Almén, O., Bruce, G. (1961). Collection and sputtering experiments with noble gas ions. *Nuclear Instruments And Methods, 11*, 257 - 278.

Anderson C. A. (1970). Analytical methods for the ion miroprobe mass analyzer part II. *International Journal of Mass Spectrometry and Ion Physics, 3*, 413 - 428.

Andersen, C. A., Hinthorne, J. R. (1972). Ion Microprobe Mass Analyzer. *Science, 175*, 853 - 860.

Andersen, H. H., Bay, H. L. (1975). Heavy ion sputtering yields of gold: Further evidence of nonlinear effects. *Journal of Applied Physics, 46*, 2416 - 2422.

Deenapanray, P. N. K., Petravic, M. (1999). Angular and Energy Dependence of the Ion Beam Oxidation of Si Using Oxygen Ions from a Duoplasmatron Source. *Surface and Interface Analysis, 27*, 92 – 97.

Deline, V. R., Evans Jr., C. A., Williams, P. (1978a). A unified explanation for secondary ion yields. *Applied Physics Letters, 33*, 578 - 580.

Deline, V. R., Katz, W., Evans Jr., C. A., Williams, P. (1978b). Mechanism of the SIMS matrix effect. *Applied Physics Letters, 33*, 832 - 835.

Franzreb, K., Lörincík, J., Williams, P. (2004). Quantitative study of oxygen enhancement of sputtered ion yields. I. Argon ion bombardment of a silicon surface with O_2 flood. *Surface Sciece, 573*, 291 - 309.

Gschneidner Jr, K. A. (1964). Physical Properties and Interrelationships of Metallic and Semimetallic Elements. *Solid State Physics, 16*, 275 - 476.

Kilner, J. A., Ilkov, L. (1984). Observations of electron stimulated desorption during SIMS profiling of insulators. *Vacuum, 34,* 139 - 143.

Krohn Jr., V. E. (1962). Emission of negative ions from metal surfaces bombarded by positive cesium ions. *Journal of Applied Physics, 33*, 3523 - 3525.

Laegreid, N., Wehner, G. K. (1961). Sputtering Yields of Metals for Ar+ and Ne+ Ions with Energies from 50 to 600 ev. *Journal of Applied Physics, 32*, 365 – 369.

Lewis, R. K., Mirabito, J. M., Tsai, J. C. C. (1973). Primary oxygen ion implantation effects on depth profiles by secondary ion emission mass spectrometry. *Applied Physics letters, 23*, 260 - 262.

Li, X. -P., Ceperley, D. M., Martin, R. M. (1991). Cohesive energy of silicon by the Green's-function Monte Carlo method. *Journal, 44*, 10929 - 10932.

Rosenberg, D., Wehner, G. K. (1962). Sputtering Yields for Low Energy He+, Kr+, and Xe+ Ion Bombardment. *Journal of Applied Physics, 33*, 1842 - 1845.

Seah, M. P. (1981). Pure element sputtering yields using 500-1000 eV argon ions. *Thin Solid Films, 81*, 279 - 287.

Sigmund, P. (1969). Theory of Sputtering. I.Sputtering Yield of Amorphous and Polycrystalline Targets*. *Journal, Physical Review*, *184*, 383 - 416.

Slodzian, G., Henequin, J. F. (1966). Sur l'emission ionique secondaire des metaux en presence d'oxygene. *Comptes rendus hebdomadaires des seances de l'Academie des sciences. Serie B, Sciences physiques, 263*, 1246 - 1249.

Sobers, R. C., Franzreb, K., Williams, P. (2004). Quantitative measurement of O/Si ratios in oxygen-sputtered silicon using 18O implant standards. *Applied Surface Science, 231-232*, 729 - 733.

Steinbrüchel, Ch. (1985). A Simple Formula for Low-Energy Sputtering Yields. *Applied Physics A, 36*, 37 - 42.

Williams, P., Evans Jr., C. A. (1977). Depth profile detection limit of $3x10^{15}$ atom cm^{-3} for As in Si using Cs^+ bombardment negative secondary ion mass spectrometry. *Applied Physics Letters, 30*, 559 - 561.

Williams, P., Evans Jr., C. A. (1978). Anomalous enhancement of negative sputtered ion emission by oxygen. *Surface Science, 78*, 324 - 338.

Williams, P., Katz, W., Evans Jr., C. A. (1980). Towards a universal model for sputtered ion emission. *Nuclear Instruments and Methods, 168*, 373 - 377.

Wilson, W. D., Haggmark, L. G., Biersack, J. P. (1977). Calculations of nuclear stopping, ranges, and straggling in the low-energy region. *Physical Review B, 15*, 2458 - 2468.

Wittmaack, K. (2000). Local SiO_2 formation in silicon bombarded with oxygen above the critical angle for beam-induced oxidation: new evidence from sputtering yield ratios and correlation with data obtained by other techniques. *Surface and Interface Analysis, 29,* 721 - 725.

Zalm, P. C. (1983). Energy dependence of the sputtering yield of silicon bombarded with neon, argon, krypton, and xenon ions. *Journal of Applied Physics, 54*, 2660 - 2666.

CHAPTER 4

ELONGATION OF ION BEAM MIXING TAILS BY STEEP OXYGEN GRADIENT

4.1 Ion Beam Mixing and Elongation of Mixing Tails

Abrupt changes in atom composition with depth are common in semiconductor samples and SIMS depth profiles are often made to measure these features. A trace element may be present as a monolayer or as a doped element with an atom density that changes in a step function. In such cases, the change in measured secondary ion intensity with depth does not appear as sharp in the depth profile due to ion beam mixing (Blank 1979, Williams 1980). After the primary ion beam sputters through an elemental discontinuity in the sample, the secondary ion intensity is observed to decrease exponentially and the depth required for the intensity to drop a factor of ten is defined as the decay length. Briefly, mixing a surface impurity into N subsurface layers makes much of the impurity inaccessible to sputter removal, which is limited to the outer 1-2 atomic layers. Removal of one atomic layer, and the dilute impurity it contains, moves the mixing zone 1 layer deeper into the bulk and thus dilutes the mixed zone impurity, and the surface layer content, by 1/N. The use of oxygen in SIMS to increase useful ion yields can further distort depth profiles. The decay length of silver in silicon was shown by Williams and Baker (Williams 1981) to increase by a factor of ten when oxygen gas was added to the sample chamber during SIMS depth profiling with an

argon ion beam. The authors attributed the increase in decay length to a segregation of silver away from the oxygenated surface during sputtering. This further dilutes the impurity content of the surface layer and reduces the impurity removal rate accordingly. More specifically, they argued that the chemical segregation at the surface was due to a steep oxygen gradient at the sample surface and the greater affinity of silicon for oxygen compared to that of silver.

Another proposed explanation for chemical segregation during SIMS depth profiling is that trace impurities become trapped at the rear interface of a silicon dioxide layer that forms in the mixing region of the ion beam and the sample below (Boudewijn 1984), again removing impurity from the surface layer(s) whence sputtering occurs. Williams and Baker had shown that the decay length of silver does not increase significantly under 8keV O_2^+ ion bombardment as it does with argon ion beams with oxygen flood gas added to the sample chamber and argued that the oxygen ion beam does not produce significant increases in decay length because the oxygen ion beam does not produce a steep oxygen gradient at the sample surface. It was noted by Wittmaack (1984) that the 8keV O_2^+ ion beam on the Cameca IMS-3f does not produce a stoichiometric silicon dioxide layer at the surface due to the relatively high sputter yield resulting from the angle of incidence. Most studies of this phenomenon since then have suggested that the trapping of trace elements beneath a stoichiometric silicon dioxide layer is responsible for the observed

increase in decay length during SIMS depth profiling (Deenapanray 1999, 2000, Elst 1993, Kilner 1992, Menzel 1990, Petravic 1996, 1998, Williams J 1997, Wittmaack 1984, 1986, 1987, Zalm 1992a, 1992b).

A key parameter in deciding between the surface oxide and surface antisegregation explanations for profile broadening is the composition of the sputtered surface layers: does segregation only occur if SiO_2 is formed, or can it be detected at lower oxygen levels? Presented here is a quantitative study of decay lengths as a function of surface oxygen concentration using the ^{18}O minor isotope method discussed in chapter 3 of this dissertation and elsewhere (Franzreb 2004, Sobers 2004). The chemical segregation of gold and other elements in silicon was studied using the ^{18}O implant standard sample and buried or surface monolayers of impurities in silicon. The ^{18}O method measures the oxygen concentration of the surface monolayer from which atoms are sputtered. Other studies of oxygen induced chemical segregation have used methods such as Rutherford backscattering, RBS, to measure the surface oxygen concentration that measure the average bulk oxygen concentration over several monolayers.

4.2 Measurement of Decay Lengths of Gold, Silver and Copper in Silicon

Simultaneous measurements of the decay length of gold in silicon and the surface oxygen concentration were made by sputter coating a thin layer of gold onto the surface of the ^{18}O in silicon implant sample. Figures

4.1 and 4.2 are examples of SIMS depth profiles of the ^{18}O implant in silicon sample with a gold-coated surface made using an 8keV argon ion beam. The decay length of gold in figure 4.1 is relatively short and due to ion beam mixing only. The addition of oxygen flood gas during the depth profile experiment of figure 4.2 significantly increased the decay length of gold.

The sputter rates (and depth scale) for each profile were determined from the previously determined depths of the ^{18}O and ^{27}Al implant profile peaks (table 3.1 of chapter 3 of this dissertation) or in some cases from profilometer measurements of the sputtered craters. The depth scale of figure 4.2 for example was determined knowing the peak of the ^{18}O implant is 160nm deep into the sample and the decay length of gold in silicon for this profile was found to be 114nm. The ratio of $^{16}O^+$ to background subtracted $^{18}O^+$ secondary ion intensities at the peak of the ^{18}O implant profile and the previously determined ^{18}O to silicon ratio of 0.02 provided the O/Si of 2.6. By comparison the O/Si ratio during the depth profile experiment of figure 1 was $7x10^{-3}$ and the gold in silicon decay length was 24nm.

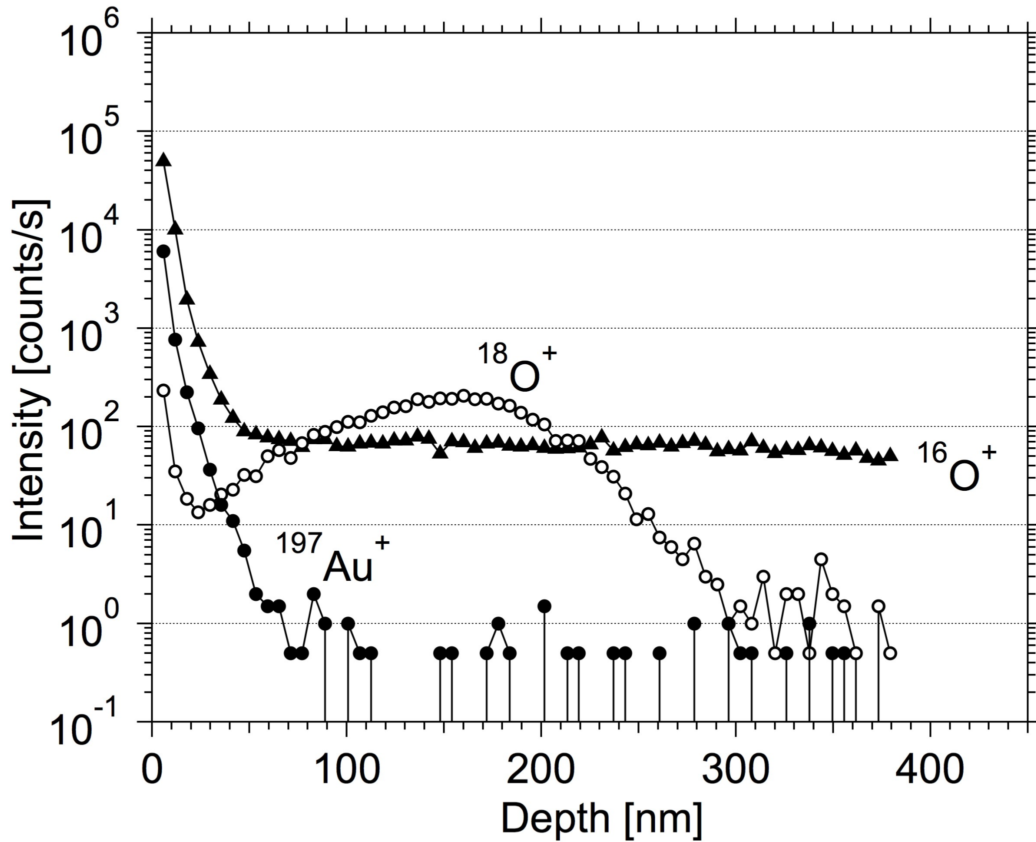

Figure 4.1. A positive SIMS depth profile of a silicon sample acquired with an 8keV Ar^+ primary ion beam having a current of 50nA and a 250µm raster. The silicon sample contains an ^{18}O implant and a thin coating of gold at the sample surface. The ambient pressure in the sample chamber during the depth profile was $2x10^{-7}$ torr. The O/Si ratio was found to be $7x10^{-3}$ from the $^{16}O^+$ and $^{18}O^+$ secondary ion intensities and the ^{18}O and silicon atom densities at the peak of the ^{18}O implant profile. The depth of the peak of the ^{18}O implant was used to determine the sputter rate and the decay length of gold was found to be 24nm.

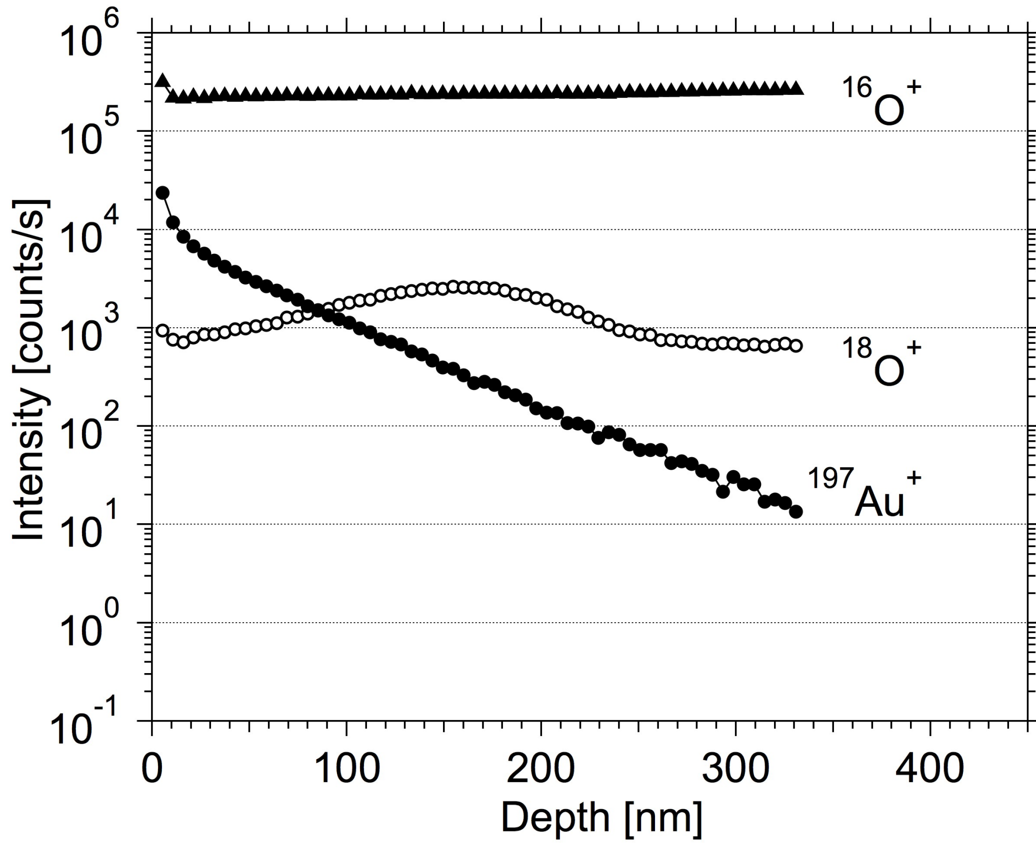

Figure 4.2. A positive SIMS depth profile of a silicon sample acquired with an 8keV Ar^+ primary ion beam having a current of 172nA and a 250µm raster. The silicon sample contains an ^{18}O implant and a thin coating of gold at the sample surface. Oxygen gas was introduced to the sample chamber during the experiment to a pressure of $7x10^{-6}$ torr. The O/Si ratio was found to be 2.6 from the $^{16}O^+$ and $^{18}O^+$ secondary ion intensities and the ^{18}O and silicon atom densities at the peak of the ^{18}O implant profile. The depth of the peak of the ^{18}O implant was used to determine the sputter rate and the decay length of gold was found to be 114nm.

Several depth profiles similar to those of figures 4.1 and 4.2 were made with argon primary ion beams. The results of these experiments are shown in figure 4.3 as a plot of gold in silicon decay length as a function of the surface oxygen atom fraction. Each data point in figure 4.3 is the measured decay length and oxygen atom fraction measured in a single depth profile. Three different argon ion beam energies were used in this study. Negative secondary ions were measured for 17keV argon ion beams but the mixing phenomenon is independent of the polarity of the ions sampled. The pressure of the oxygen flood gas and the ion beam current density were used to control the O/Si ratio. The results shown in figure 4.3 indicate that a stoichiometric SiO_2 surface layer is not required for chemical segregation of gold at the surface argon sputtered silicon. The measured decay length increases with oxygenation of the surface below the stoichiometric silicon dioxide ratio of 2 with no break at this ratio in the trend.

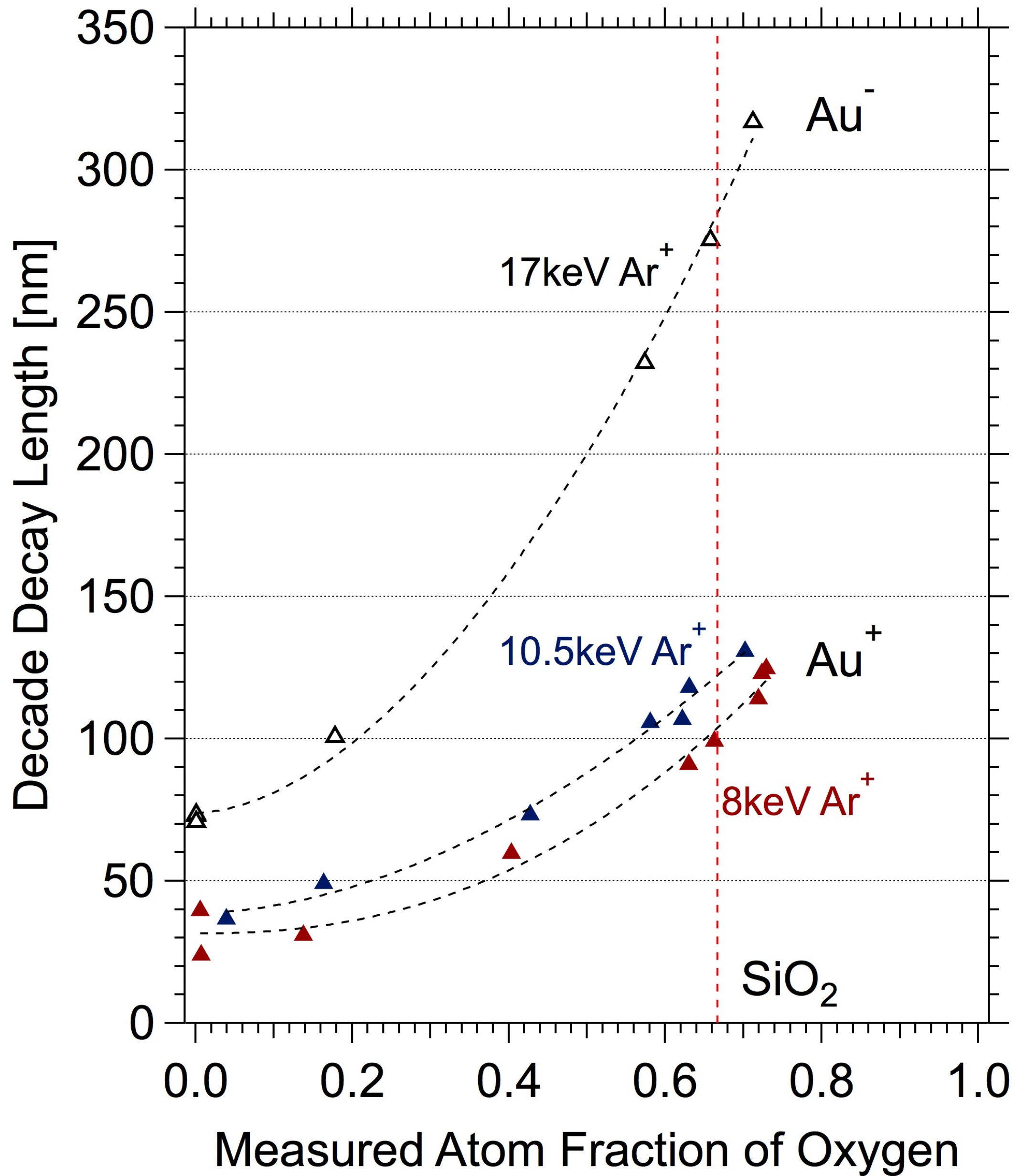

Figure 4.3. Measured gold decay lengths in silicon as a function of the oxygen atom fraction in the sputtered flux. The oxygen atom fraction is determined by the impact angle and energy of the oxygen ion beams (closed circular data points) and by the oxygen flood gas pressure in the sample chamber when sputtering with argon ion beams (triangular data points). Three different argon ion beam energies were used. Positive secondary ions were measured except for experiments with 17keV argon primary ion beams. The vertical red line is the atom fraction of stoichiometric SiO_2.

For comparison, decay length measurements were also made for copper and silver in a similar manner. Measurement of shallow decay lengths of surface layers is difficult because the surface oxide is being sputtered away in the same region while conditions are changing. For this reason, samples containing buried monolayers of copper and silver in silicon were studied. The copper monolayer in silicon was prepared by the LeRoy Eyring Center for Solid State Science at ASU and the silver monolayer sample was of unknown origin. Steady state sputtering is minimally disrupted and quickly reestablished after the ion beam sputters through a buried monolayer. This makes observation of the relatively short decay lengths easier despite low ion yields when the surface oxygen concentration is small.

Figures 4.4 and 4.5 show depth profiles acquired with a 13keV argon ion beam of the buried silver and copper in silicon monolayer samples respectively. Profilometer measurements of sputtered craters established that the depth of the silver monolayer is 87nm and the copper monolayer is 100nm deep. The depth of the monolayer provided an alternate method of sputter rate measurements for later experiments without the need for sputtered crater depth measurements. Depth profiles of the silver and copper monolayer samples acquired with the addition of oxygen flood gas to the sample chamber, A, in figures 4.4 and 4.5 have increased decay lengths similar to that observed for gold.

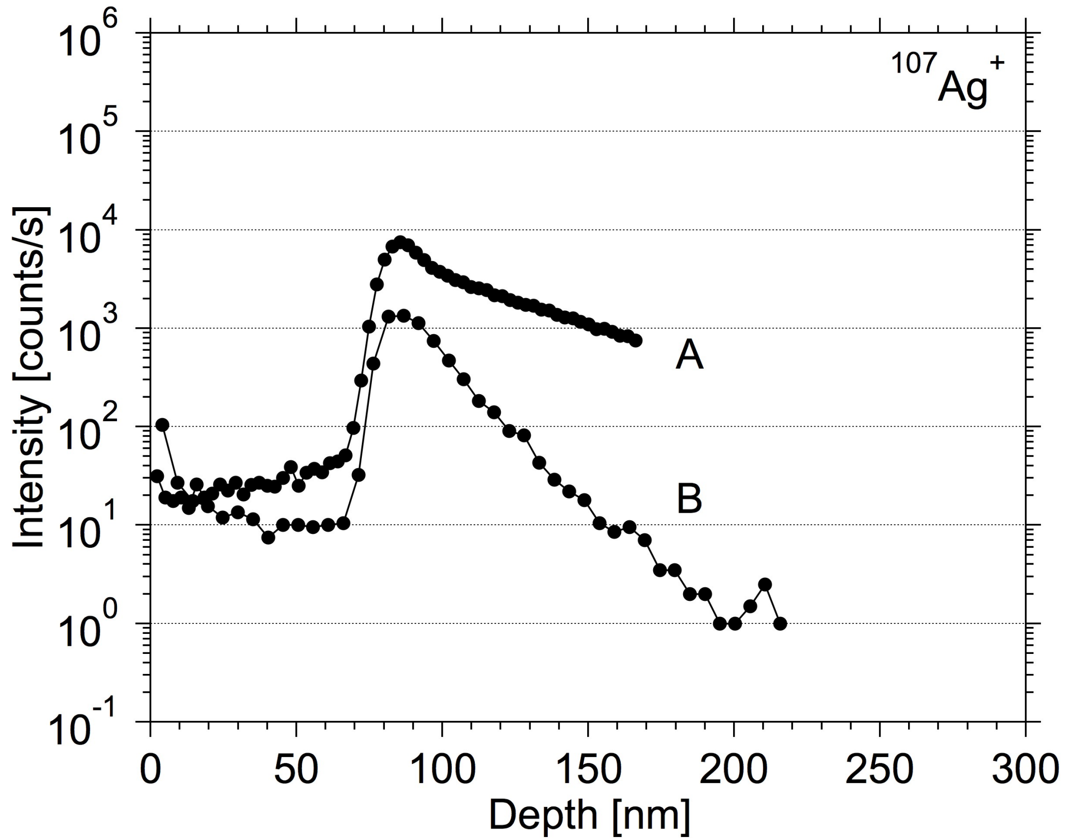

Figure 4.4. Positive SIMS depth profiles of a silver monolayer in silicon sample acquired with a 13keV Ar^+ primary ion beam with and without the addition of oxygen flood gas. The depth scale of each experiment was determined from profilometer measurements of sputtered craters and the depth of the silver monolayer is 87nm. The experiment with the lower intensity secondary ions was made using 75nA primary ion beam and a 300μm raster. The greater secondary ion intensity of the other experiment is due to the higher ion yields produced by the addition of oxygen flood gas to a pressure of $2x10^{-6}$ torr. This experiment used a 75nA primary ion beam with a 300μm raster. Surface oxygen concentrations were determined from depth profile experiments of the ^{18}O implant under the same conditions. The oxygen flood gas produced an O/Si ratio of 2.5 and the decay length of $^{107}Ag^+$ decay length from this same profile was found to be 108nm. The experiment without the oxygen flood gas had an O/Si ratio of $1.1x10^{-2}$ and a 30nm decay length.

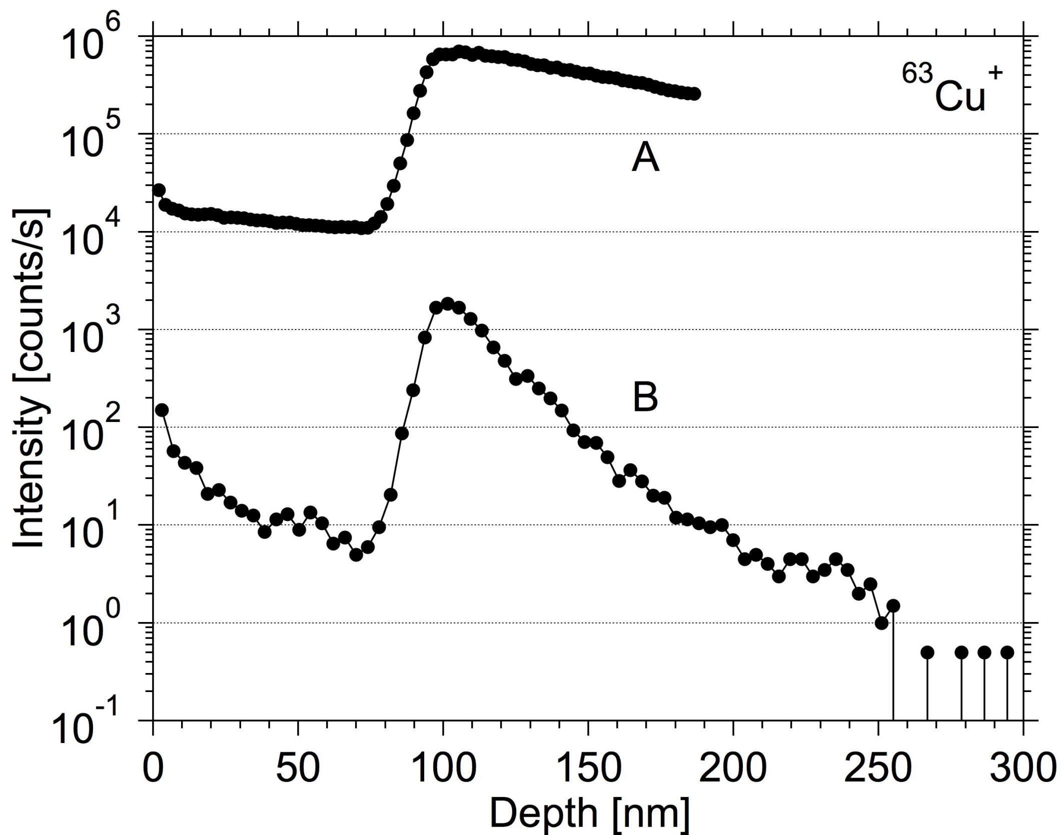

Figure 4.5. Positive SIMS depth profiles of a copper monolayer in silicon sample acquired with a 13keV Ar^+ primary ion beam with and without the addition of oxygen flood gas. The depth scale of each experiment was determined from profilometer measurements of sputtered craters and the depth of the copper monolayer is 100nm. The experiment with the lower intensity secondary ions was made using 280nA primary ion beam and a 500µm raster. The greater secondary ion intensity of the other experiment is due to the higher ion yields produced by the addition of oxygen flood gas to a pressure of $1x10^{-5}$ torr. This experiment used a 360nA primary ion beam with a 500µm raster. Surface oxygen concentrations were determined from depth profile experiments of the ^{18}O implant under the same conditions. The oxygen flood gas produced an O/Si ratio of 2.7 and the decay length of $^{65}Cu^+$ decay length from this same profile was found to be 159nm. The experiment without the oxygen flood gas had an O/Si ratio of $8.5x10^{-3}$ and the decay length is 32nm.

The buried monolayer samples do not contain the ^{18}O implant so simultaneous measurement of surface oxygen concentration and decay length were not possible. Instead, the ^{18}O implant in silicon sample and the buried monolayer samples were loaded into the sample chamber together and rapid consecutive measurements were made of each sample under the same instrument settings. Between measurements, the primary ion beam alignment was checked to avoid crater edge effects.

The average measured decay lengths of copper and silver are plotted as a function of oxygen atom fraction in figures 4.6 and 4.7. The error bars are the standard deviation of multiple decay length measurements at that atom fraction of oxygen. The multiple decay lengths represent rapidly repeated depth profiles under the same experimental conditions and also measurements of different isotopes within each depth profile. While not investigated as thoroughly as gold, the large increase in decay length with addition of oxygen flood is apparent for both silver and copper under bombardment with argon ion beam. The silver monolayer was also investigated using O_2^+ primary ion beam. The much lower decay length for silver using an oxygen ion beam observed by Williams and Baker is reproduced now with a quantitative measurement of the surface oxygen atom fraction.

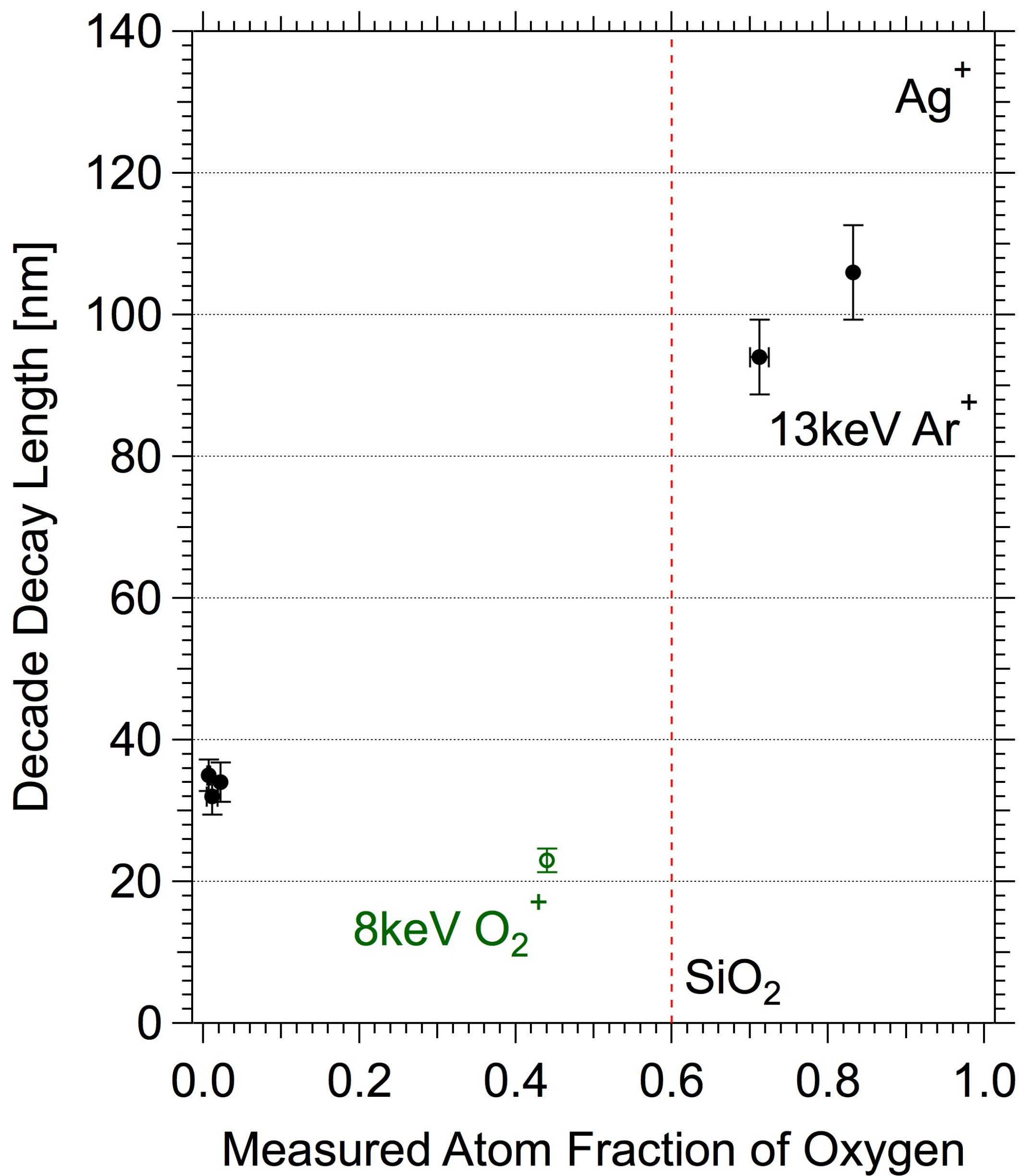

Figure 4.6. Measured decay lengths of a silver monolayer in silicon measured against the surface atom fraction of oxygen. Depth profiles were acquired using an argon ion beam. Oxygenation of the sample surface was accomplished by addition of oxygen flood gas to the sample chamber. The open symbol data point is the measured decay length of the silver while sputtering with an 8keV O_2^+ primary ion beam. The vertical red line is the atom fraction of stoichiometric SiO_2.

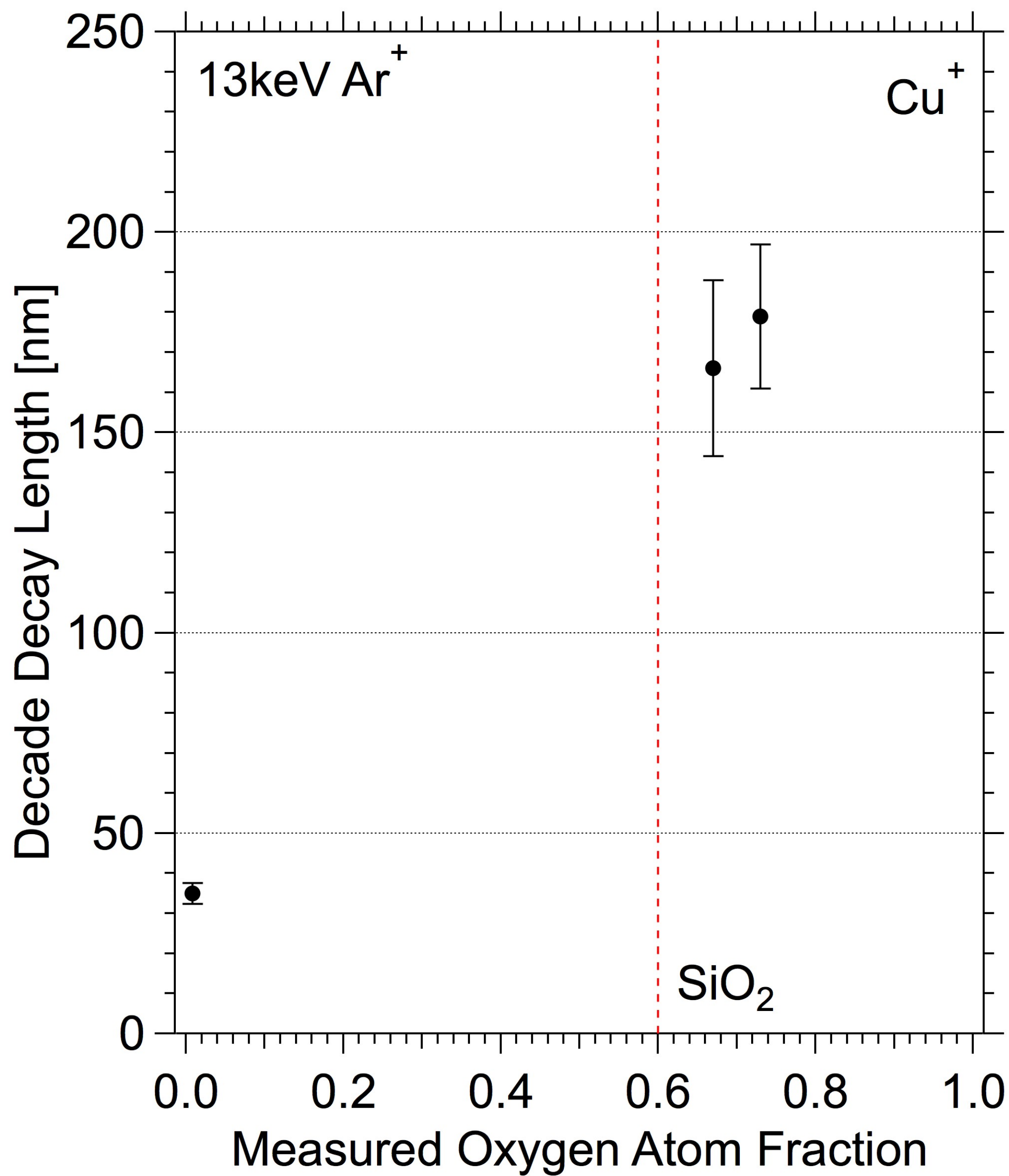

Figure 4.7. Measured decay lengths of a copper monolayer in silicon measured against the surface atom fraction of oxygen. Depth profiles were acquired using an argon ion beam. Oxygenation of the sample surface was accomplished by addition of oxygen flood gas to the sample chamber. The vertical red line is the atom fraction of stoichiometric SiO_2.

Decay lengths of gold were also measured using oxygen ion beams. The surface O/Si produced by oxygen ion beams was controlled by the impact angle of the primary ion beam, with oxygen ion beams impacting closer to normal producing greater O/Si ratios due to the lower sputter yield at near-normal angles. For oxygen ion beams the decay length appears to be dependent on the ion beam mixing depth. Figure 4.8 plots both the measured gold decay length and oxygen atom fraction against the projected range of the ion beam. Projected ranges were calculated from the ion beam energy and angle using TRIM software (Biersack 1980).

The near surface oxygen gradient of silicon sputtered with an oxygen ion beam may be increased with the addition of oxygen flood gas. Several depth profiles of the gold-coated ^{18}O implant in silicon sample were made with oxygen primary ion beams of different energies with the addition of oxygen flood gas to observe the effect on the gold decay length. These data are included in figure 4.9, which reproduces the gold decay length data for oxygen ion beams without oxygen flood and also with 8keV Ar^+ ion beams of figure 4.3. All decay lengths measured with both an oxygen ion beam and oxygen flood gas are represented as closed circular data points. A continuous increase in gold decay length with surface oxygen atom fraction for each oxygen ion beam is observed with no break at stoichiometric SiO_2.

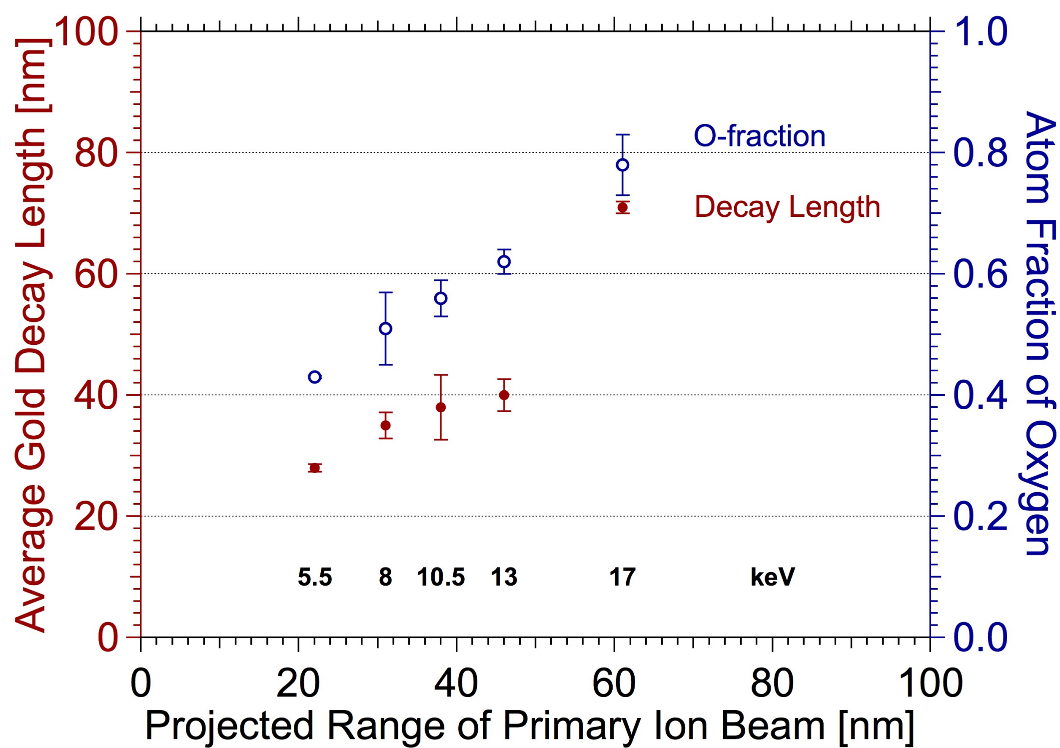

Figure 4.8. Measured gold decay lengths and surface oxygen atom fractions for silicon sputtered with oxygen ion beams plotted against the predicted ion range of each beam. The projected ion ranges were calculated from the impact energy and angles using TRIM software.

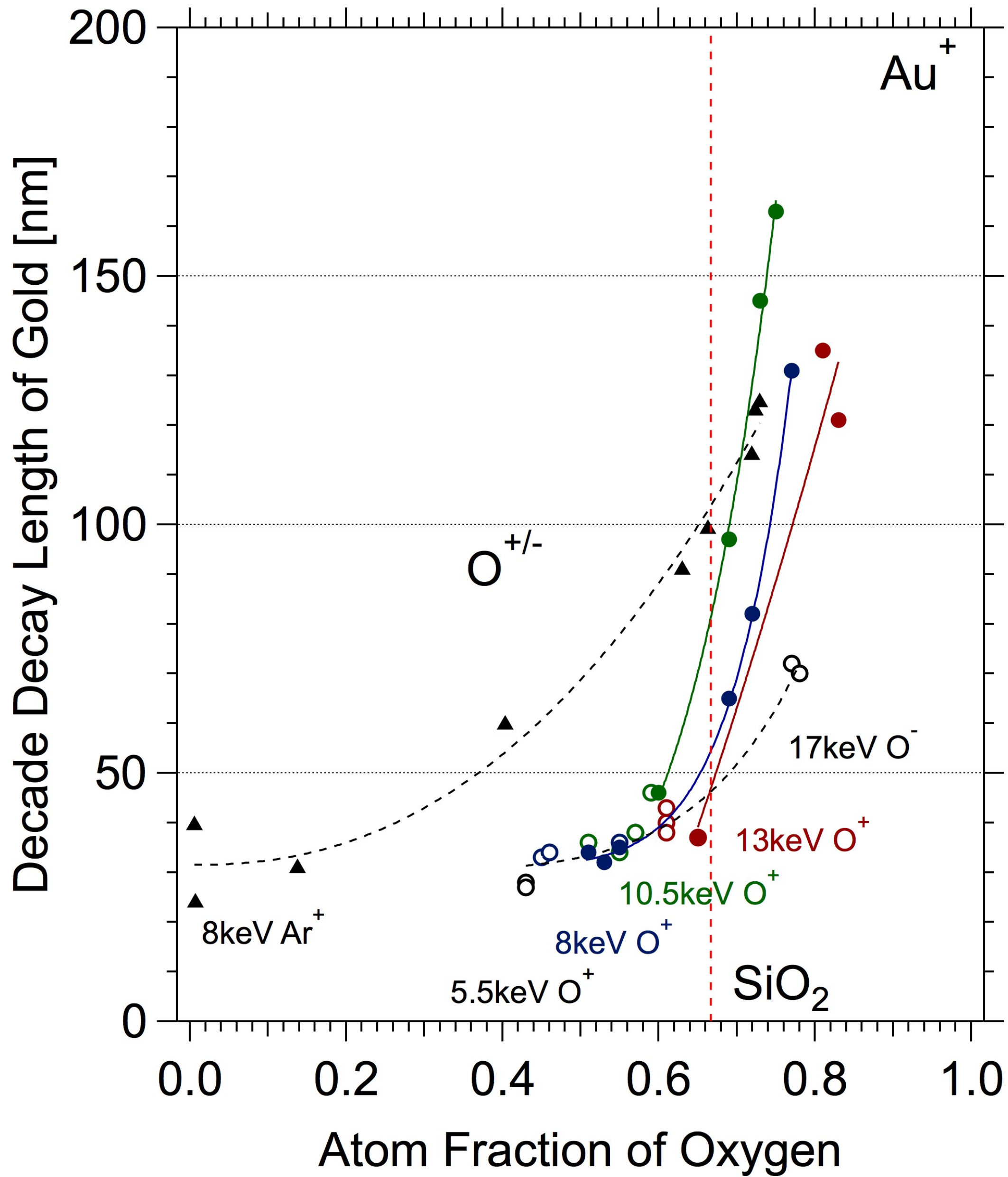

Figure 4.9. Measured gold decay lengths in silicon as a function of the oxygen atom fraction in the sputtered flux for depth profile experiments made with oxygen ion beams of various impact energies and 8keV argon ion beams. The oxygen atom fraction is determined by the impact angle and energy of the oxygen ion beams (open circular data points). Closed circle data points with color are decay lengths of gold measured when sputtering with oxygen ion beams with the addition of oxygen flood gas. For comparison, decay lengths measured from argon sputtered silicon with the addition of flood gas is included as closed triangular data points. The vertical red line is the atom fraction of stoichiometric SiO_2.

4.3 Measurement of Decay Lengths of Gold, Silver and Copper in Silicon

Hues and Williams (Hues 1986) provided further evidence supporting a near surface oxygen gradient model for chemical segregation during sputtering by demonstrating that the decay lengths of calcium and magnesium in silicon decrease with oxygenation of the sample surface. They argued that with higher oxygen affinities, these impurity elements move towards the oxygenated surface rather than away.

Silicon samples containing buried monolayers of both calcium and magnesium were prepared in order to repeat this study in a more quantitative manner. These samples were made at the LeRoy Eyring Center for Solid State Science at ASU. The monolayer samples were loaded into the sample chamber simultaneous with the ^{18}O implant in silicon sample and measurements were made on each under identical operating conditions.

An example of SIMS depth profile of the buried magnesium monolayer sample is shown in figure 4.10. This depth profile was made using a 13keV argon ion beam with no addition of oxygen flood gas. The magnesium monolayer depth was determined by profilometer measurements of the sputtered craters to be 79nm. The measured decay length of magnesium in silicon in this depth profile was found to be 21.6nm using the ^{24}Mg and 22.3nm using the ^{25}Mg isotope. The O/Si ratio was measure to be 3.6×10^{-2} by depth profiling the ^{18}O in silicon sample.

Figure 4.11 contains two depth profiles of the calcium monolayer made using a 10.5keV argon ion beam. The figure shows the measured $^{40}Ca^{+}$ secondary ion intensity with depth and with oxygen flood added to the sample surface (red) and without (black) for comparison. Experiment A in this figure was made using a 45nA primary ion beam current with a 250μm raster, and the oxygen flood gas pressure was $2x10^{-5}$torr. A 70nA primary ion beam with 250μm raster was used to acquire depth profile B. The surface O/Si was measured by alternating measurements of the ^{18}O implant and calcium monolayer samples under identical operating conditions. The O/Si ratio for the 10.5keV argon ion beam with no addition of oxygen flood has been measured previously and is less than 0.01. With low oxygen concentration, the calcium decay length was found to be 22nm. With oxygenation of the sample surface, the decay length was observed to decrease. With an O/Si of 3.2, the decay length of calcium was 14nm.

The measured decay lengths of magnesium and calcium are plotted as a function of the oxygen atom fraction in figures 4.12 and 4.13. Each decay length reported is the average measured decay length from multiple profiles and from multiple calcium secondary ion intensities measured in each profile. Doubly charged calcium ions were also monitored. The error bars in figures 4.12 and 4.13 are the standard deviation of all decay lengths of all secondary ion species from multiple depth profiles.

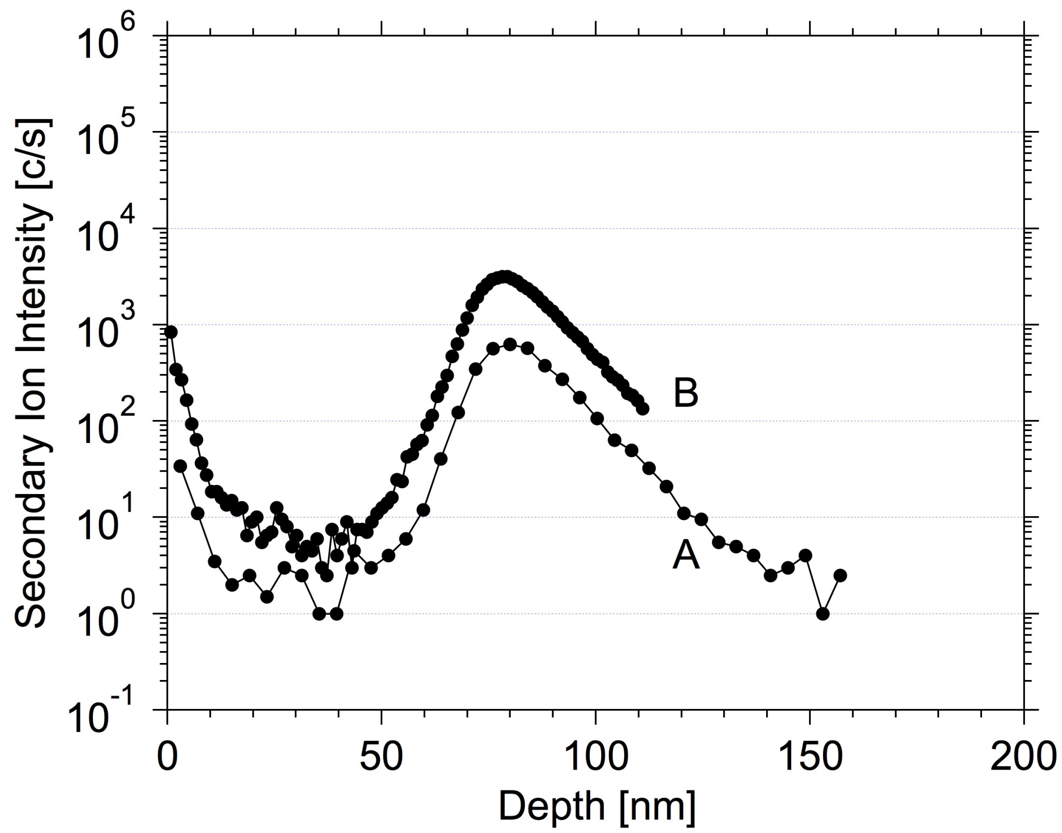

Figure 4.10. Two positive SIMS depth profiles of the magnesium in silicon monolayer sample acquired with 13keV argon ion beams. Profile A was made using a 82nA primary ion beam with a square raster of 250µm and a sample chamber pressure of $1x10^{-7}$ torr. The closed symbol profile was acquired with a 78nA primary ion beam with a square raster of 250µm. Oxygen flood gas was added to the sample chamber during experiment B with a measured pressure of $1x10^{-5}$ torr. The surface O/Si ratios were measured by moving to the ^{18}O in silicon implant and sputtering under the same conditions. The surface O/Si ratio of experiment B was found to be 3.9 and that of experiment A was $3.6x10^{-2}$. The decay length of magnesium was 22nm for experiment A and 21nm for experiment B.

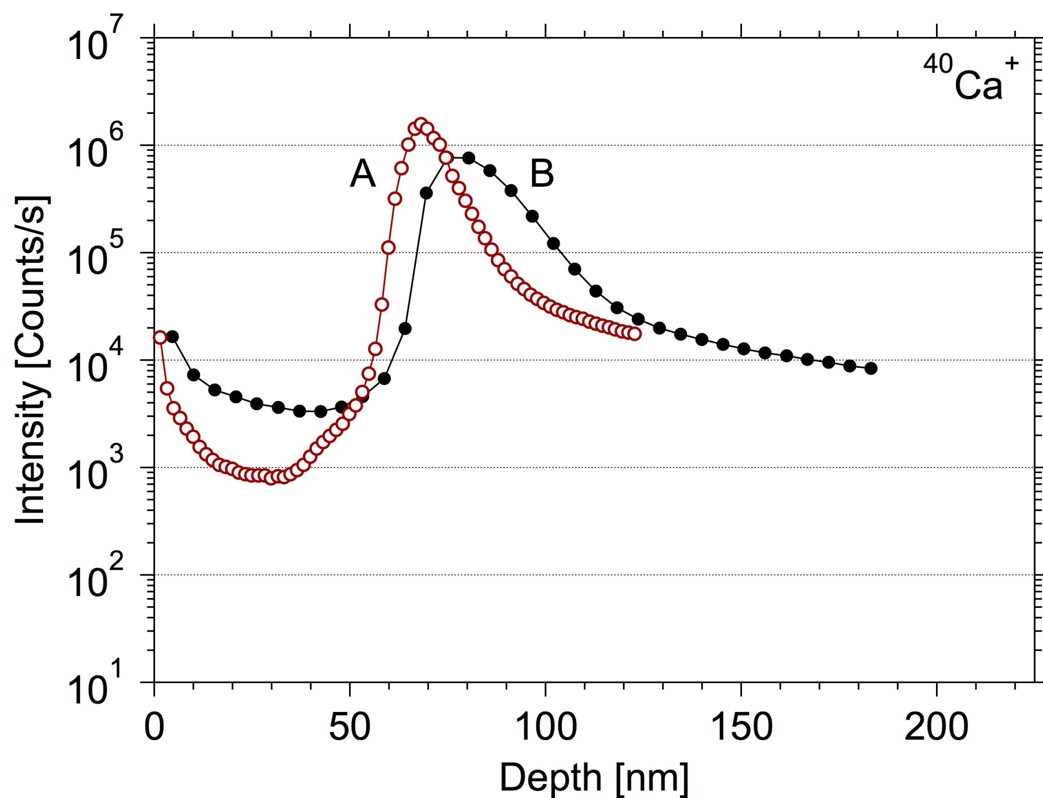

Figure 4.11. Two positive SIMS depth profiles of the magnesium in silicon monolayer sample acquired with 13keV argon ion beams. Profile A was made using a 45nA primary ion beam with a square raster of 250µm. Oxygen flood gas was added to the sample chamber during experiment A with a measured pressure of 2×10^{-5} torr. Profile B was made using a 70nA primary ion beam with a square raster of 250µm. No flood gas was added during this experiment and the base pressure was 1×10^{-7} torr. The surface O/Si of argon sputtered silicon has been observed to be less than 0.01. The surface O/Si ratio of experiment A was measured by moving to the ^{18}O in silicon implant and sputtering under the same conditions. The surface O/Si of experiment A was 3.2. The decay length of magnesium was 14nm for experiment A and 22nm for experiment B.

With addition of oxygen flood gas, the decay length of calcium in silicon decreases as observed by Hues and Williams, but their observations of a decrease in decay length for magnesium were not reproduced here. Instead, the decay length remains fairly unchanged upon oxygenation. Hues used samples for which the Mg or Ca were sputtered onto the surfaces of the respective samples, so that the difficulties of overlap with the decreasing surface oxide layer, discussed earlier, probably complicated the measurements. The present measurements are presumed to be more reliable.

Another interesting observation is that the measured depth of the calcium monolayer is less when the surface is oxygenated which suggests movement of the calcium towards the sputtered surface. Profilometer measurements of the sputtered craters were used to determine the sputter rates of the monolayer. With no addition of oxygen flood gas, the depth of the calcium monolayer was found to be 77nm ± 3nm. The measured depth of the same monolayer is 67nm ±1nm when the sample is sputtered with oxygen flood gas. To check this result, the sputter rates during depth profile experiments of the monolayer sample were compared to those of the ^{18}O implant sample made under the same conditions and found to be in agreement. The sputter rate of the ^{18}O implant was determined from the known depth of the peak of the ^{18}O implant and the sputter rate of the monolayer was found from crater depth measurements.

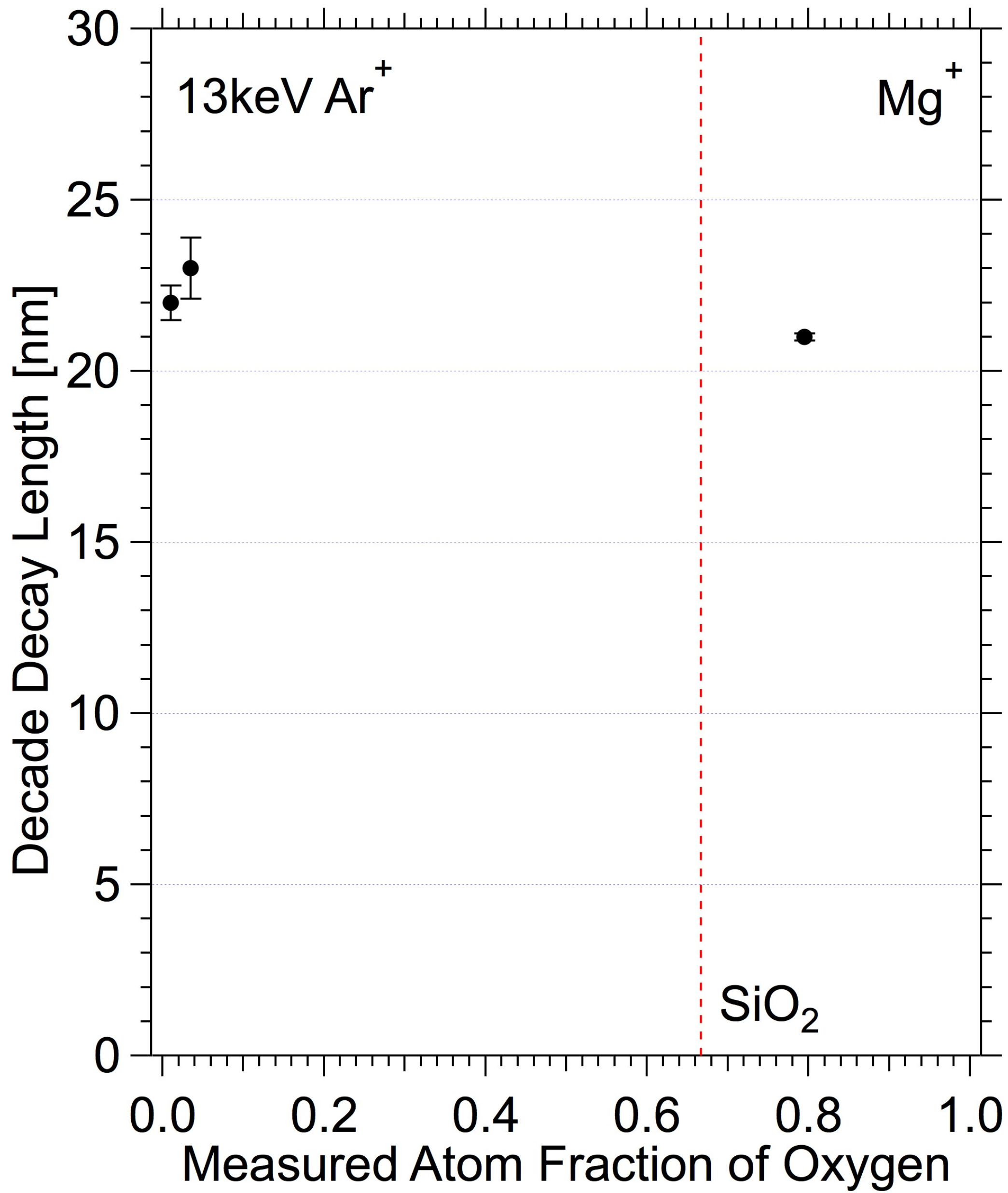

Figure 4.12. Measured decay lengths of a magnesium monolayer in silicon measured against the surface oxygen atom fraction. Depth profiles were acquired using an argon ion beam. Oxygenation of the sample surface was accomplished by addition of oxygen flood gas to the sample chamber. The vertical red line is the atom fraction of stoichiometric SiO_2.

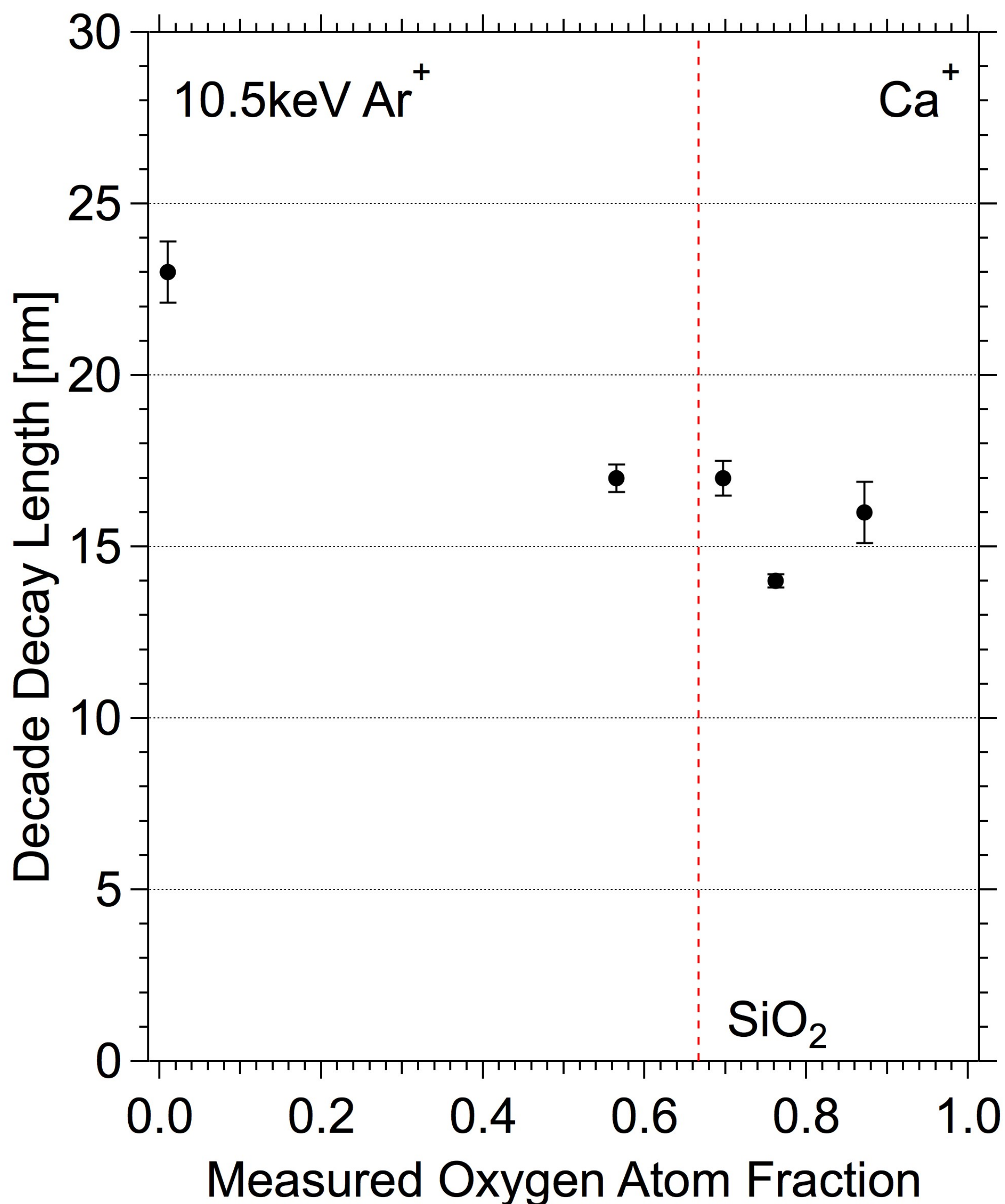

Figure 4.13. Measured decay lengths of a calcium monolayer in silicon measured against the surface oxygen atom fraction. Depth profiles were acquired using an argon ion beam. Oxygenation of the sample surface was accomplished by addition of oxygen flood gas to the sample chamber. The vertical red line is the atom fraction of stoichiometric SiO_2.

4.4 Summary

As discussed earlier there are two models for chemical segregation at the sample surface. One requires a stoichiometric silicon dioxide layer be formed at the sample surface segregating impurities to the backside of the oxide layer. This effect then would be similar to effects seen during growth of thermal oxides on silicon wafers. Chemical segregation is thought to occur by the trapping of impurity elements at the defect-rich interface of this surface SiO_2 region and the un-oxidized sample below. The second model explains chemical segregation as the result of relative affinities for oxygen of the trace element and silicon in the presence of a steep surface oxygen gradient.

The results presented here support the near surface oxygen gradient model proposed by Williams and Baker. The larger gold in silicon decay lengths observed when oxygen is introduced to the sample surface through a flood gas rather than the primary ion beam may be explained by the steep near surface oxygen gradient. The oxygen gradient under oxygen bombardment may be increased with addition of oxygen flood and the decay length of gold was shown to increase. A requirement of a surface silicon dioxide layer for chemical segregation cannot explain continuous increase in decay length of gold in silicon that begins at O/Si ratios well below the oxide stoichiometry. There also appears to be no break in the decay length trend at the stoichiometric SiO_2 ratio. The observations of decay lengths of calcium and magnesium in silicon with

addition of oxygen flood gas also support the near surface oxygen gradient model. The decay length of both would be expected to increase or remain unchanged if the mechanism for chemical segregation was the formation of a surface SiO_2 layer. If the mechanism for chemical segregation was the formation of a surface SiO_2 layer the decay length of both would be expected to increase or remain unchanged, depending on whether or not they were segregated away from the oxide. Calcium and magnesium would be expected to either move to the interface region producing an increased decay length or the decay length would remain unchanged. The decay length of neither increases, indicating that for these elements at least, there is no migration to an interface region, and the decrease in decay length observed for calcium strongly supports the oxygen gradient model.

4.5 References

Biersack, J. P., Haggmarck, L. G. (1980). A monte-carlo computer-program for the transport of energetic ions in amorphous targets. *Nuclear Instruments & Methods, 174*, 257 - 269.

Blank, P., Wittmaack, K. (1979). Implications in the use of sputtering for layer removal - system Au on Si. *Radiation Effects Letters, 43*, 105 - 110.

Boudewijn, P. R., Akerboom, H.W.P., Kempeners, M.N.C. (1984). Profile distortions in SIMS. *Spectrochimica Acta Part B: Atomic Spectroscopy, 39,* 1567 - 1571.

Deenapanray, P.N.K., Petravic, M. (1999). On the migration behavior of metal impurities in Si during secondary ion mass spectrometry profiling using low-energy oxygen ions. *Journal of Applied Physics, 85*, 3993 - 3998.

Deenapanray, P.N.K., Petravic, M. (2000). On the segregation of Ca at SiO2/Si interface during oxygen ion bombardment. *Surface and Interface Analysis, 29*, 160 - 167.

Elst, K., Vandervorst, W. (1993). The influence of oxygen on the analysis of a Pt/Si-structure with secondary ion mass spectrometry. *Journal of Applied Physics, 73*, 4649 - 4659.

Franzreb, K., Lörincík, J., Williams, P. (2004). Quantitative study of oxygen enhancement of sputtered ion yields. I. Argon ion bombardment of a silicon surface with O_2 flood. *Surface Sciece, 573*, 291 - 309.

Hues, S. M., Williams, P. (1986). Oxygen-induced segregation effects in sputter depth-profiling. *Nuclear Instruments and Methods in Physics Research B, 15,* 206 - 209.

Kilner, J.A., McPhail, D.S., Littlewood, S.D. (1992). A quantitative study of copper segregation in silicon under oxygen ion beam bombardment using SIMS. *Nuclear Instruments and Methods in Physics Research B, 64,* 632 - 635.

Menzel, N., Wittmaack, K. (1990). RBS study on bombardment-induced redistribution of copper impurities in silicon using neon, oxygen and nitrogen ion beams at different impact angles. *Nuclear Instruments and Methods in Physics Research B, 45,* 219 - 222.

Petravic, M., Svensson, B.G., Williams, J.S., Glasko, J.M. (1996). Segregation effects in SIMS profiling of impurities in silicon by low energy oxygen ions. *Nuclear Instruments and Methods in Physics Research B, 118,* 151 - 155.

Petravic, M. (1998). On the segregation of metals during low-energy oxygen bombardment of silicon. *Applied Surface Science, 135*, 200 - 204.

Sobers, R. C., Franzreb, K., Williams, P. (2004). Quantitative measurement of O/Si ratios in oxygen-sputtered silicon using 18O implant standards. *Applied Surface Science, 231-232*, 729 - 733.

Williams, J.S., Short, K.T., Petravic, M., Svensson, B.G. (1997). Oxidation of silicon by low energy oxygen ions. *Nuclear Instruments and Methods in Physics Research B, 121,* 24 - 29.

Williams, P., Baker, J. E. (1980). Quantitative analysis of interfacial impurities using secondary-ion mass spectrometry. *Applied Physics Letters, 36*, 842 - 845.

Williams, P., Baker, J. E. (1981). Implantation and ion beam mixing in thin film analysis. *Nuclear Instruments and Methods, 182/183,* 15 - 24.

Wittmaack, K. (1984). Beam-induced broadening effects in sputter depth profiling. *Vacuum, 34,* 119 - 137.

Wittmaack, K. (1986). Abrupt reduction of the partial sputtering yield of copper in silicone due to beam induced oxidation and segregation. *Applied Physics Letters, 48*, 1400 - 1402.

Wittmaack, K. (1987). Exceptionally pronounced redistribution of silver in oxygen bombarded silicon. *Applied Physics Letters, 50*, 815 - 817.

Zalm, P.C., Vriezema, C.J. (1992a). Oxygen bleed-in during SIMS depth profiling: curse or blessing? *Nuclear Instruments and Methods in Physics Research B, 64,* 626 - 631.

Zalm, P.C., Vriezema, C.J. (1992b). On some factors limiting depth resolution during SIMS profiling. *Nuclear Instruments and Methods in Physics Research B, 67,* 495 - 499.

CHAPTER 5

COMPREHENSIVE REFERENCE LIST

Almén, O., Bruce, G. (1961). Collection and sputtering experiments with noble gas ions. *Nuclear Instruments And Methods, 11*, 257 - 278.

Anderson C. A. (1970). Analytical methods for the ion miroprobe mass analyzer part II. *International Journal of Mass Spectrometry and Ion Physics, 3*, 413 - 428.

Andersen, C. A., Hinthorne, J. R. (1972). Ion Microprobe Mass Analyzer. *Science, 175*, 853 - 860.

Andersen, H. H., Bay, H. L. (1975). Heavy ion sputtering yields of gold: Further evidence of nonlinear effects. *Journal of Applied Physics, 46*, 2416 - 2422.

Ascenzi, D., Franceschi, P., Tosi, P., and Bassi, D., Kaczorowska, M., Harvey, J. M. (2003). Bond-forming reactions of dications: Production of ArO^+ and ArO^{2+} in the reaction of Ar^{2+} with O_2. *Journal of Chemical Physics, 118*, 2159 - 2163.

Aston, F. W. (1919). A positive ray spectrograph. *Philosophical Magazine, 38*, 707 - 714.

Aston, F. W. (1920). The mass-spectra of chemical elements. *Philosophical Magazine, 39*, 611 - 625.

Austin, L. W. (1906). On an emission of negatively charged particles produced by canal rays. *Physical Review, 21*, 312 - 319.

Biersack, J. P., Haggmarck, L. G. (1980). A monte-carlo computer-program for the transport of energetic ions in amorphous targets. *Nuclear Instruments & Methods, 174*, 257 - 269.

Blank, P., Wittmaack, K. (1979). Implications in the use of sputtering for layer removal - system Au on Si. *Radiation Effects Letters, 43*, 105 - 110.

Boudewijn, P. R., Akerboom, H.W.P., Kempeners, M.N.C. (1984). Profile distortions in SIMS. *Spectrochimica Acta Part B: Atomic Spectroscopy, 39,* 1567 - 1571.

Deenapanray, P.N.K., Petravic, M. (1999). On the migration behavior of metal impurities in Si during secondary ion mass spectrometry profiling using low-energy oxygen ions. *Journal of Applied Physics, 85*, 3993 - 3998.

Deenapanray, P. N. K., Petravic, M. (1999). Angular and Energy Dependence of the Ion Beam Oxidation of Si Using Oxygen Ions from a Duoplasmatron Source. *Surface and Interface Analysis, 27*, 92 – 97.

Deenapanray, P.N.K., Petravic, M. (2000). On the segregation of Ca at SiO2/Si interface during oxygen ion bombardment. *Surface and Interface Analysis, 29*, 160 - 167.

Deline, V. R., Evans Jr., C. A., Williams, P. (1978a). A unified explanation for secondary ion yields. *Applied Physics Letters, 33*, 578 - 580.

Deline, V. R., Katz, W., Evans Jr., C. A., Williams, P. (1978b). Mechanism of the SIMS matrix effect. *Applied Physics Letters, 33*, 832 - 835.

Elst, K., Vandervorst, W. (1993). The influence of oxygen on the analysis of a Pt/Si-structure with secondary ion mass spectrometry. *Journal of Applied Physics, 73*, 4649 - 4659.

Ewers, P. (1899). Zur Mechanik der canal- and kathoden-strahlen. *Annalen Der Physik Und Chemie, 69*, 167 – 199.

Franzreb, K., Williams, P. (2003). Inert gas clusters ejected from bursting bubbles during sputtering. *Physical Review Letters, 91*, 015501 - 015504.

Franzreb, K., Lörincík, J., Williams, P. (2004). Quantitative study of oxygen enhancement of sputtered ion yields. I. Argon ion bombardment of a silicon surface with O_2 flood. *Surface Sciece, 573*, 291 - 309.

Franzreb, K., Sobers Jr., R. C., Lörinčik, J., Williams, P. (2004a). Formation of doubly positively charged diatomic ions of Mo_2^{2+} produced by Ar^+ sputtering of an Mo metal surface. *Journal of Chemical Physics, 120*, 7983 - 7986.

Franzreb, K, Sobers Jr., R. C., Lörinčik, J., Williams, P. (2004b). Detection of the diatomic dications SiH^{2+} and AlH^{2+}. *Applied Surface Science, 231-232*, 82 - 85.

Franzreb, K., Sobers Jr., R. C., Lörinčik, J., Williams, P. (2005). Observation of small long-lived diatomic dications BeH^{2+} and BeD^{2+}. *Physical Review A, 71*, 024701-1 – 024701-4.

Gehrcke, E., Reichenheim, O. (1906). Anodenstrahlen. *Berichte der Deutschen Physikalischen Gessellschaft, 8*, 559 - 566.

Gehrcke, E., Reichenheim, O. (1907a). Anodenstrahlen. *Berichte der Deutschen Physikalischen Gessellschaft, 9*, 76 - 83.

Gehrcke, E., Reichenheim, O. (1907b). Anodenstrahlen. *Berichte der Deutschen Physikalischen Gessellschaft, 9*, 374 - 379.

Gehrcke, E., Reichenheim, O. (1907c). Anodenstrahlen. *Berichte der Deutschen Physikalischen Gessellschaft, 9*, 200 - 204.

Gill, P. M. W. (1988). How does a dication lose a proton. *Journal Of The American Chemical Society, 110*, 5311 - 5314.

Guilhaus, M., Brenton, A. G., Beynon, J. H., Rabrenović, M., Ragué Schleyer, P. von (1984). First observation of He_2^{2+}: charge stripping of He_2^+ using a double-focusing mass spectrometer. *Journal of Physics B, 17*, L605 - L610.

Goldstein, E. (1898). Ueber eine noch nicht untersuchte strahlungsform an der cathode inducirter entladungen. *Annalen Der Physik Und Chemie, 64*, 38 - 48.

Grove, W. R. (1852). On the electro-chemical polarity of gases. *Philosophical Transactions Of The Royal Society Of London, 142*, 87 - 101.

Gschneidner Jr, K. A. (1964). Physical Properties and Interrelationships of Metallic and Semimetallic Elements. *Solid State Physics, 16*, 275 - 476.

Herzog, R. F. K., Viehböck, F. P. (1949). Ion source for mass spectrography. *Physical Review, 46*, 855 - 856.

Herzog, R. F. K., Poschenrieder, W. P., Satkiewicz, F. G. (1973). Observations of clusters in a sputtering ion source. *Radiation Effects, 18*, 199 - 205.

Honig, R. E. (1958). Sputtering of Surfaces by Positive Ion Beams of Low Energy. *Journal, 29*, 549 - 555.

Hues, S. M., Williams, P. (1986). Oxygen-induced segregation effects in sputter depth-profiling. *Nuclear Instruments and Methods in Physics Research B, 15,* 206 - 209.

Jonathon, P., Boyd, R. K., Brenton, A. G., Beynon, J. H. (1986). Diatomic dications containing one inert gas atom. *Chemical Physics, 110*, 239 - 246.

Johnson, R., Manfred, B. (1979). Thermal-energy charge transfer, fiuenching, and association reactions of doubly charged ions in the rare gases. *Physical Review A, 20*, 87 - 97.

Joyes , P. P. (1968). Èvaluation théorique de la pulvérization cathodique isotrope. *Journal de Physique, 29*, 774 - 790.

Joyes, P. P. (1969). Ètude théorique de l'émission ionique secondaire. *Journal de Physique, 30*, 365 - 376.

Kilner, J. A., Ilkov, L. (1984). Observations of electron stimulated desorption during SIMS profiling of insulators. *Vacuum, 34,* 139 - 143.

Kilner, J.A., McPhail, D.S., Littlewood, S.D. (1992). A quantitative study of copper segregation in silicon under oxygen ion beam bombardment using SIMS. *Nuclear Instruments and Methods in Physics Research B, 64,* 632 - 635.

Krohn Jr., V. E. (1962). Emission of negative ions from metal surfaces bombarded by positive cesium ions. *Journal of Applied Physics, 33*, 3523 - 3525.

Laegreid, N., Wehner, G. K. (1961). Sputtering Yields of Metals for Ar+ and Ne+ Ions with Energies from 50 to 600 ev. *Journal of Applied Physics, 32*, 365 – 369.

Lewis, R. K., Mirabito, J. M., Tsai, J. C. C. (1973). Primary oxygen ion implantation effects on depth profiles by secondary ion emission mass spectrometry. *Applied Physics letters, 23*, 260 - 262.

Li, X. -P., Ceperley, D. M., Martin, R. M. (1991). Cohesive energy of silicon by the Green's-function Monte Carlo method. *Journal, 44*, 10929 - 10932.

Menzel, N., Wittmaack, K. (1990). RBS study on bombardment-induced redistribution of copper impurities in silicon using neon, oxygen and nitrogen ion beams at different impact angles. *Nuclear Instruments and Methods in Physics Research B, 45,* 219 - 222.

Moens, M., Adams, F. C., Simons, D. S. (1987). Dependence of interface widths on ion-bombardment conditions in secondary ion mass-spectrometric analysis of a nickel chromium multilayer structure. *Analytical Chemistry, 59*, 1518 - 1529.

Nefedova, W., Boldyrev, A.I., Simons, J. (1995). Ab-initio energies and tunneling lifetimes of the doubly-charged AH(2+) (A=Mg-Ar). *International Journal of Quantum Chemistry, 55,* 441 - 457.

Pauling, L. (1933). The normal state of the helium molecule ions He_2^+ and He_2^{2+}. *Journal of Chemical Physics, 1*, 56 - 59.

Petravic, M., Svensson, B.G., Williams, J.S., Glasko, J.M. (1996). Segregation effects in SIMS profiling of impurities in silicon by low energy oxygen ions. *Nuclear Instruments and Methods in Physics Research B, 118,* 151 - 155.

Petravic, M. (1998). On the segregation of metals during low-energy oxygen bombardment of silicon. *Applied Surface Science, 135*, 200 - 204.

Plücker, J. (1858). Ueber die einwirkung des magneten auf die elektrischen entladungen in verdünnten gasen. *Annalen Der Physik Und Chemie, Vol*, 88 - 106.

Rosenberg, D., Wehner, G. K. (1962). Sputtering Yields for Low Energy He+, Kr+, and Xe+ Ion Bombardment. *Journal of Applied Physics, 33*, 1842 - 1845.

Schauer, S. N., Williams, P. (1990). Elimination of cluster interferences in secondary ion mass spectrometry using extreme energy filtering. *International Journal of Mass Spectrometry and Ion Processes, 103*, 21 – 29.

Schauer, S. N., Williams, P. (1992). Doubly charged ions of fourth-row elements. *Physical Review B, 46*, 15452 - 15464.

Seah, M. P. (1981). Pure element sputtering yields using 500-1000 eV argon ions. *Thin Solid Films, 81*, 279 - 287.

Sigmund, P. (1969). Theory of Sputtering. I.Sputtering Yield of Amorphous and Polycrystalline Targets*. *Journal, Physical Review*, *184*, 383 - 416.

Slodzian, G., Henequin, J. F. (1966). Sur l'emission ionique secondaire des metaux en presence d'oxygene. *Comptes rendus hebdomadaires des seances de l'Academie des sciences. Serie B, Sciences physiques, 263*, 1246 - 1249.

Slodzian, G. (1975). Some problems encountered in secondary ion emission applied to elementary analysis. *Surface Science, 48*, 161 - 186.

Sobers, R. C., Franzreb, K., Williams, P. (2004). Quantitative measurement of O/Si ratios in oxygen-sputtered silicon using 18O implant standards. *Applied Surface Science, 231-232*, 729 - 733.

Steinbrüchel, Ch. (1985). A Simple Formula for Low-Energy Sputtering Yields. *Applied Physics A, 36*, 37 - 42.

Thomson, J. J. (1910). Rays of positive electricity. *Philosophical Magazine, 20*, 752 - 767.

Thomson, J. J. (1913a). On the appearance of helium and neon in vacuum tubes. *Nature, 90*, 645 - 647.

Thomson, J. J. (1913b). On the appearance of helium and neon in vacuum tubes. *Science, 37*, 360 - 364.

Tosi, P., Correale, R., Wenyun, L., Stefano, F., Bassi, B. (1999). Production of the molecular di-cation ArN^{2+} in the Reaction Ar^{2+}+ N_2. *Physical Review Letters, 82*, 450 - 452.

Watson, H. E. (1914). Some experiments on the electrical discharge in helium and neon. *Proceedings of the Cambridge philosophical society. Mathematical and physical sciences, 17*, 90 - 107.

Weathers, D. L., McDaniel, F. D., Matteson, S., Duggan, J. L., Anthony, J. M., Douglas, M. A. (1991). Triply-ionized B_2 molecules from a tandem accelerator. *Nuclear Instruments and Methods in Physics Research B, 56/57*, 889 - 892.

Wien, W. (1898). Untersuchungen über die electrische entlandung in verdünnten gasen. *Annalen Der Physik Und Chemie, 65*, 440 - 452.

Williams, J.S., Short, K.T., Petravic, M., Svensson, B.G. (1997). Oxidation of silicon by low energy oxygen ions. *Nuclear Instruments and Methods in Physics Research B, 121,* 24 - 29.

Williams, P., Evans Jr., C. A. (1977). Depth profile detection limit of $3x10^{15}$ atom cm^{-3} for As in Si using Cs^{+} bombardment negative secondary ion mass spectrometry. *Applied Physics Letters, 30*, 559 - 561.

Williams, P., Evans Jr., C. A. (1978). Anomalous enhancement of negative sputtered ion emission by oxygen. *Surface Science, 78*, 324 - 338.

Williams, P., Baker, J. E. (1980). Quantitative analysis of interfacial impurities using secondary-ion mass spectrometry. *Applied Physics Letters, 36*, 842 - 845.

Williams, P., Katz, W., Evans Jr., C. A. (1980). Towards a universal model for sputtered ion emission. *Nuclear Instruments and Methods, 168*, 373 - 377.

Williams, P., Baker, J. E. (1981). Implantation and ion beam mixing in thin film analysis. *Nuclear Instruments and Methods, 182/183,* 15 - 24.

Wilson, W. D., Haggmark, L. G., Biersack, J. P. (1977). Calculations of nuclear stopping, ranges, and straggling in the low-energy region. *Physical Review B, 15*, 2458 - 2468.

Wittmaack, K. (1979). Ionization mechanism of H^{+} sputtered from hydrogenated silicon. *Physical Review Letters, 43*, 872 - 875.

Wittmaack, K. (1980). Comparison of ion-excited auger electron emission and secondary ion emission from silicon bombarded with noble gas ions. *Nuclear Instruments and Methods, 170*, 565 - 569.

Wittmaack, K. (1984). Beam-induced broadening effects in sputter depth profiling. *Vacuum, 34,* 119 - 137.

Wittmaack, K. (1986). Abrupt reduction of the partial sputtering yield of copper in silicone due to beam induced oxidation and segregation. *Applied Physics Letters, 48*, 1400 - 1402.

Wittmaack, K. (1987). Exceptionally pronounced redistribution of silver in oxygen bombarded silicon. *Applied Physics Letters, 50*, 815 - 817.

Wittmaack, K. (2000). Local SiO_2 formation in silicon bombarded with oxygen above the critical angle for beam-induced oxidation: new evidence from sputtering yield ratios and correlation with data obtained by other techniques. *Surface and Interface Analysis, 29,* 721 - 725.

Zalm, P. C. (1983). Energy dependence of the sputtering yield of silicon bombarded with neon, argon, krypton, and xenon ions. *Journal of Applied Physics, 54*, 2660 - 2666.

Zalm, P.C., Vriezema, C.J. (1992a). Oxygen bleed-in during SIMS depth profiling: curse or blessing? *Nuclear Instruments and Methods in Physics Research B, 64,* 626 - 631.

Zalm, P.C., Vriezema, C.J. (1992b). On some factors limiting depth resolution during SIMS profiling. *Nuclear Instruments and Methods in Physics Research B, 67,* 495 - 499.